Università degli Studi di Padova

Centro Ricerche Fusione (**CRF**)

Università degli studi di Napoli Federico II

Universidade de Lisboa

Instituto Superior Técnico (**IST**)

JOINT RESEARCH DOCTORATE IN FUSION SCIENCE AND ENGINEERING

Cycle XXX

DEVELOPMENT, OPTIMIZATION AND TESTING OF HIGH PERFORMANCE COOLING SYSTEMS FOR FUSION DEVICES

Coordinator: Prof. Paolo Bettini

Supervisors: Prof. Piergiorgio Sonato, Dr. Piero Agostinetti

Ph.D. student: Giulio Gambetta

Padova

UNIVERSITÀ
DEGLI STUDI
DI PADOVA

JOINT Doctorate and NETWORK in Fusion Science and Engineering

Network Partners:

- Instituto Superior Técnico (IST) Lisboa, Portugal
- Università degli studi di Padova, Italy
- Ludwig Maximilians University Munich, Germany

In collaboration with:

Consorzio RFX
IPP Garching, Germany

Abstract

One of the fundamental components for the full scientific exploitation of future fusion experiments is the Neutral Beam Injectors (NBI). Such devices shall operate in ITER and DEMO experiments at particle energy levels, heating power and steady state working conditions that have never been simultaneously reached before in other experimental facilities.

In addition to the challenging technological and manufacturing aspects, NBIs coupled with future fusion reactors should be characterized by much demanding efficiency, availability and reliability factors, composing and additional set of critical issues that claim for an accurate and robust design.

The research activity of this PhD thesis focuses on particular components of the negative ion beam source, the accelerating electrostatic grids, which are characterized by high heating power and highly focused power densities, and hence require a continuous active cooling in order guarantee proper heat removal and temperature control.

Present research aims to verify the present solution applied inside the NBI accelerator grids realized in PRIMA facility (i.e. MITICA experiment) and to perform further improvements in the heat transfer process with an acceptable pressure drop and reliable manufacturing process. The main advantages rely on the possibility to extend the fatigue life-cycle of different high thermal stress components and to investigate the possibility to employ alternative dielectric fluids instead of water. Such design solutions would in fact allow the exploitation of less performing fluids in terms of cooling capability. This is particularly relevant in view of DEMO and future power plants characterized by higher efficiency and reliability.

The research activity is not only limited to numerical analyses but includes the manufacturing of the prototypes of the accelerator grid cooling channels where the novel channel design solutions have been implemented.

In order to characterize the experimental thermo-fluid dynamic behaviour of the samples the hydraulic performances and the cooling efficiency in transient operations have been tested in a specific plant for thermo-hydraulic measurements, called Insulation and Cooling Experiment (ICE).

In order to support further optimization design activity and the implementation of the cooling solutions inside full-scale models of the electrostatic accelerating grid in future injector beam source the experimental results have been obtained and compared both with Computational Fluid-Dynamic models in order to validate the numerical realized predictions.

The thesis is organized in five chapters.

The first one is an introduction to nuclear fusion and magnetic confinement. The second chapter gives a description of the NBI devices, both from the conceptual point of view and technology of its components. The third chapter tackles the development of the novel cooling solution designs on a single channel and single beamlet group sub-modelling of the electrostatic grid system. The fourth chapter confronts the numerical obtained results to the experimental ones performed in the specific test-bed facility.

In the fifth chapter the different developed designs have been upgraded to the electrostatic grid full scale model and a general scheme for further design improvement is introduced. Final general conclusions are drawn in the last dedicated section of the work.

An outline of dealt topics is placed at the beginning of each of the different five chapters.

Sommario

Uno dei componenti fondamentali per la completa fruibilità scientifica dei futuri esperimenti sulla fusion nucleare è il sistema di iniezione dei neutri (NBI). Tali dispositivi dovranno operare negli esperimenti ITER e DEMO a livelli energetici delle particelle accelerate, carichi termici e condizioni di lavoro in regime stazionario che non sono mai state simultaneamente raggiunte in alcun impianto sperimentale.
In aggiunta ai severi aspetti tecnologici e dal punto di vista della realizzazione, i sistemi di iniezione dei neutri accoppiati a futuri reattori a fusion dovranno essere caratterizzati da fattori di efficienza, disponibilità e affidabilità molto severi, contribuendo a comporre un ulteriore insieme di aspetti critici richiedenti un accurate e robusto lavoro di progettazione.
L'attività di ricerca illustrata nella presente tesi di Dottorato si focalizza su particolari componenti della sorgente di fasci di ioni negative, le griglie di accelerazione, caratterizzate da elevate carichi termici e densità di potenze altamente localizzate, i quali richiedono un continuo ed attivo sistema di raffreddamento al fine di garantire un'appropriata rimozione del calore ed un adeguato controllo in temperatura.
Scopo del presente lavoro di ricerca è la verifica dell'attuale soluzione progettuale inserita nelle griglie di accelerazione del Sistema di iniezione dei neutri che verrà realizzato nel complesso sperimentale PRIMA (ovvero in MITICA) nonché la realizzazione di ulteriori migliorie nei meccanismi di scambio termico con cadute di pressione accettabili e processi di lavorazione affidabili. Il maggiore vantaggio associate a tali risultati risiede nella possibilità di estendere il ciclo di vita a fatica dei diversi component soggetti ad elevati sforzi di natura termomeccanica e nell' avvio di un'indagine volta alla possibilità di impiego di fluidi dielettrici alternativi all'acqua.

Tali soluzioni progettuali permetterebbero di fatto l'impiego di fluidi meno prestanti dal punto di vista delle proprietà termo-fluidodinamiche caratterizzanti i meccanismi di scambio termico. Tale considerazione risulta particolarmente rilevante in vista di DEMO e di futuri impianti per la produzione di energia caratterizzati da alte efficienze termodinamiche ed elevati fattori di affidabilità.
L'attività di ricerca non risulta limitata alle sole analisi numeriche ma include la realizzazione dei prototipi dei canali di raffreddamento delle griglie di accelerazione in cui sono state ricavate le innovative soluzioni progettuali.
Al fine di caratterizzare in ambito sperimentale il comportamento termo-fluidodinamico dei provini, le prestazioni idrauliche e l'efficienza di raffreddamento in regimi transitori sono state testate in un apposito impianto per l'esecuzione di prove termoidrauliche, denominato Insulating and Cooling Experiment (ICE).
Al fine di supportare ulteriori attività di ottimizzazione e l'implementazione delle soluzioni di raffreddamento in modelli in scala reale delle griglie di accelerazione elettrostatica in future sorgenti di iniezione di fasci, i risultati sperimentali così ottenuti sono stati confrontati con modelli fluido-dinamici al fine di validarne le previsioni realizzate numericamente.
La tesi è suddivisa in cinque capitoli.
Il primo capitolo effettua un'introduzione alla fusione nucleare ed al confinamento magnetico. Il secondo fornisce una descrizione dei dispositivi di iniezione dei neutri, sia da un punto di vista concettuale che tecnologico dei suoi componenti e sottosistemi.
Il terzo capitolo affronta lo sviluppo delle soluzioni innovative di raffreddamento su sotto modelli a singolo canale e singolo gruppo di aperture delle griglie elettrostatiche.
Il quarto capitolo confronta i risultati ottenuti numericamente con quelli sperimentali.
Nel quinto capitolo le diverse geometrie sviluppate sono state riscalate alle dimensioni reali della griglia , esso inoltre introduce uno schema generale per ulteriori migliorie nella progettazione dei canali di raffreddamento.
Le conclusioni sono tratte nell'ultima apposita sezione.
Un sommario con gli argomenti trattati è riportato all'inizio di ogni capitolo.

Resumo

Um dos componentes fundamentais para a completa exploração cientifica dos futuros experimentos de fusão nuclear é o sistema de injeção de partículas neutras (NBI). Tais dispositivos devem operar nos experimentos ITER e DEMO a nível energético de partículas, potência de aquecimento e condição de trabalho em regime estacionário nunca antes alcançados simultaneamente em outra instalação experimental.
Além dos desafios tecnológicos e de construção, os sistemas de injeção de partículas neutras acoplados aos futuros reatores de fusão nuclear devem ser caracterizados por fatores de eficiência, disponibilidade e confiabilidade, ajudando a compor um conjunto adicional de aspectos críticos que exigem um trabalho de design preciso e robusto.
A atividade cientifica desta tese de doutorado foca-se em componentes particulares das fontes de feixes de íons negativos, nas grelhas de aceleração eletrostáticas, caracterizadas por altas cargas térmicas e densidade de potência altamente localizada, que, portanto, requerem contínuo e ativo resfriamento para garantir uma apropriada remoção do calor e um adequado controle de temperatura.
O presente trabalho de pesquisa visa verificar soluções atuais aplicadas às grelhas de aceleração do sistema de injeção de partículas neutras que será realizado no complexo experimental PRIMA (isso é, no experimento MITICA) bem como a implementação de melhorias adicionais nos mecanismos de troca de calor com quedas de pressão aceitáveis e processos de usinagem confiáveis. A principal vantagem associada a estes resultados reside na possibilidade de prolongar o ciclo de vida de vários componentes sujeitos a tensões termomecânicas elevadas e de investigar a possibilidade de usar fluidos dielétricos alternativos à água. Tal consideração é particularmente relevante ao DEMO e às futuras plantas para a produção de energia caracterizada por alta eficiência termodinâmica e fatores de alta confiabilidade.
A atividade de pesquisa não se limita apenas à análise numérica, mas inclui a fabricação dos protótipos dos canais de resfriamento das grelhas de aceleração nas quais as soluções de design inovadoras foram implementadas.
Para caracterizar o comportamento dinâmico termo-fluido das amostras no campo experimental, os desempenhos hidráulicos e a eficiência de resfriamento em regimes transitórios foram testados em uma planta especial para a execução de testes termo-hidráulicos, denominada Insulating and Cooling Experiment (ICE).
A fim de suportar novas atividades de otimização e implementação de soluções de resfriamento em modelos em escala real das grelhas de aceleração eletrostática em futuras fontes de injeção de feixe, os resultados experimentais assim obtidos foram comparados com modelos fluido-dinâmicos para validar as previsões feitas numericamente.

A tese é dividida em cinco capítulos.
O primeiro capítulo faz uma introdução à fusão nuclear e ao confinamento magnético. O segundo fornece uma descrição dos dispositivos de injeção de neutros, tanto do ponto de vista conceitual como tecnológico de seus componentes e subsistemas. O terceiro capítulo aborda o desenvolvimento de soluções de resfriamento inovadoras em modelos de canal único e um único grupo de abertura das grelhas eletrostáticas. O quarto capítulo compara os resultados obtidos numericamente com os experimentais. No quinto capítulo, as diferentes geometrias desenvolvidas foram redimensionadas para as dimensões reais das grelhas e também introduz um esquema geral para novas melhorias na concepção dos canais de resfriamento.
As conclusões são apresentadas na última seção e um resumo com os tópicos abordados é mostrado no início de cada capítulo.

Index

	Abstract	*i*
	Sommario	*iii*
	Resumo	*v*
	Index	*vii*
1	*Fusion energy and plasma confinement*	*1*
1.1	*Fusion reaction process*	*2*
1.2	*Fusion plasma*	*3*
1.3	*Plasma magnetic confinement*	*4*
1.3.1	*Magnetic field related parameters*	*4*
1.4	*The Reversed Field Pinch (RFP)*	*5*
1.5	*The Stellarator*	*7*
1.6	*The Tokamak*	*8*
1.7	*ITER*	*10*
1.8	*PRIMA test facility*	*12*
1.9	*SPIDER*	*13*
1.10	*MITICA*	*15*
2	*Neutral beam injector system*	*17*
2.1	*The quest for additional heating systems*	*18*
2.2	*Additional power heating systems*	*20*
2.3	*Atomic processes during a ionization of a neutral particle and beam penetration distance*	*20*
2.4	*Positive and negative injected beams*	*23*
2.5	*Momentum transfer in ion and electron population*	*24*
2.6	*Additional effects produced on plasma through NBI*	*26*
2.7	*The D-beam design energy options*	*29*
2.8	*Pros and cons in adopting the NBI technology*	*30*
2.9	*NBI components*	*32*
2.9.1	*Ion sources and negative ion extraction*	*33*
2.9.2	*Accelerating stages*	*37*
2.9.3	*Negative ion neutralizer and electron dump (NED)*	*44*
2.9.4	*Residual ion dump*	*47*
2.9.5	*Beamline calorimeter*	*48*
2.9.6	*NB duct*	*49*
3	*Development of high performance cooling systems for fusion device*	*51*
3.1	*Active cooling of accelerating grids*	*52*
3.2	*Accelerating grids requirements*	*54*
3.3	*Identification of the objective*	*55*
3.4	*Present design solution*	*57*
3.5	*Single channel prototypes (SCPs)*	*59*
3.6	*Research methodology approach*	*60*
3.7	*Design constraints*	*60*
3.8	*Boundary conditions*	*61*
3.9	*Novel enhanced proposals*	*62*

3.10 SCP manufacturing 69

4 Testing of SCP performance 75
4.1 General description of ICE plant 76
4.2 Thermo-hydraulic test section 78
4.3 Sensors for plant control and experimental tests 81
4.4 ICE plant tests and commissioning 82
4.5 Thermo-hydraulic tests on the SCPs 86
4.6 Experimental plan 86
4.7 Pressure and leak tests 87
4.8 SCPs pressure drop characterization 89
4.9 SCPs cooling efficiency test 95
4.9.1 Equivalent electrical circuit 97
4.10 Modelling and validation 105

5 Full scale application and optimization of the novel cooling solutions 111
5.1 Segment models 112
5.2 SCP design implementation 113
5.3 Cooling and mechanical performance assessment 114
5.4 Optimization process 119

Conclusions and perspectives 127
Bibliography 131

1

1. Fusion energy and plasma confinement

The improvement of the standard of living of a growing world population implies a significant increase in the energy consumption. This is one of the most difficult challenges that the international community has faced starting from the beginning of XX century since on, one hand, energy services are fundamental to guarantee economic and social stability, but on the other, a large extent of the energy sources and related technology jeopardize environmental and geopolitical stability. In order to overcome the intrinsic limitations that each of them presents (reserves, toxic emissions, availability, CO_2 production and the climate change it implies) and dependence from foreign and unstable regions, the solution is represented by the combined use of different energy sources.

Nuclear fusion energy will play an important role in the forthcoming energetic scenario as possible base load power generation, given its potentially unlimited fuel reserves, being free from greenhouse gases emission, intrinsically safe and without waste burden for future generations. Far from being commercially available, the international community is focused on the research.

This chapter deals with the nuclear fusion and the methods used to produce and confine fusion plasma. In the first part of the chapter nuclear fusion reactions are discussed In order to achieve nuclear fusion ignition matter has to be in plasma state which has to be properly confined notably gravitationally, magnetically or inertially. The three main configurations for the magnetic confinement of fusion plasma, namely the RFP, the Stellarator and the Tokamak will be then discussed. The chapter closes with the descriptions of the main international experiment (ITER) presently under construction and the Padua Neutral Beam Test Facility with SPIDER and MITICA devices.

1.1 Fusion Reaction Process

Nuclear fusion is the reaction between two light nuclei that fuse into a heavier one, releasing energetic reaction products. Such fusion reactions are the same known to provide the huge energy production in stars.
Given a positive gain in terms of products binding energy, the main need for fusion to occur is the overcoming of the coulombic barrier existing between charged particles: the higher is the electric charge the higher is the related coulombic barrier (which scales as the squared effective nuclear charge, Z^2). As a matter of fact the heavier are the reactant nuclei the more prohibitive is to achieve fusion reactions conditions.
The controlled reaction that uses the particles' thermal energy to overcome the coulombic barrier is called controlled thermonuclear fusion.
Studies about the nuclear properties of light nuclei show that, despite the large variety of fusion reactions occurring in the universe, just three of them are exploitable on Earth's laboratory to produce energy. As a matter of fact these reactions are equals to those active in the sun, though with different chain reaction, and involve deuterium (D), tritium (T) and helium-3.
The main reactions are:

$$\begin{aligned} D + D &\rightarrow T\ (1.0\ MeV) + p\ (3.0\ MeV) \\ D + D &\rightarrow He^3 (0.8\ MeV) + n\ (2.5\ MeV) \\ D + T &\rightarrow He^4 (3.5\ MeV) + n\ (14.1\ MeV) \\ D + He^3 &\rightarrow He^4 (3.5\ MeV) + p\ (14.7\ MeV) \end{aligned} \tag{1.1}$$

Each of the four fusion processes is characterized by its proper reaction cross section. Figure 1.1 depicts such "reaction probability" (1 barn = 10^{-28} m^2) with respect to the reactant kinetic energy.

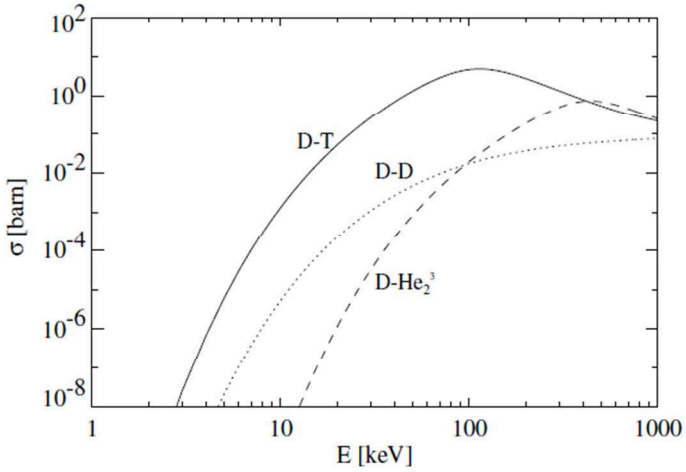

Figure 1.1– Cross section of the typical fusion reactions: (D-T), (D-D) and (D-He^3) with respect to the Deuteron energy.

It can be easily evinced that the most promising fusion reaction is the D-T one due to the fact that its cross section is considerably higher compared to the other reactions

(except at impractically high energy), reaching its maximum at a temperature of ~15 keV.
As long as tritium is a radioactive gas (β^- emitter), with half-life on Earth's condition of 12 year, it does not exist in nature and it has to be produced starting from an alternative source. Lithium is the appropriate candidate by means of two possible reactions which exploit the resulting neutrons from the D-T fusion process:

$$\begin{aligned} Li^6 + n &\rightarrow He + T + 4.8\ MeV \\ Li^7 + n &\rightarrow He + T - 2.5\ MeV \end{aligned} \tag{1.2}$$

The natural abundance of Lithium is thus distributed: 7.4 % Li^6 and 92.6 % Li^7. The real source needed to realize energy from fusion technology is therefore Lithium as its resources are much lower than Deuterium ones (which can be relatively easily extracted from seawater), although relatively abundant over Earth's upper crust.
However the technological and scientific problem connected with the exploitation of such reactions lies in the achievement and maintenance of the temperature and density conditions necessary to lead to a sufficient number of thermonuclear fusion reactions. This is what is addressed by plasma confinement.

1.2 Fusion plasmas

Plasma is a quasi-neutral ionized gas characterized by a high electrical conductivity and whose behaviour is dominated by collective effects. Two criterions must be satisfied for an ionized gas to be considered as plasma.
The first criterion involves the role of the high electrical conductivity, which results in the ability to shield electrical fields. Thus it is shown that the maximum spatial dimension over which charge inhomogeneity can appear is given by the Debye length, defined as:

$$\lambda_D = \sqrt{\frac{\varepsilon_0\, T_e}{n_e\, e^2}} \tag{1.3}$$

where T_e and n_e are the electron temperature and density [1].
Plasma behaviour requires $\lambda_D \ll L$, where L represents the typical macroscopic length of the plasma. Charge inhomogeneities are shielded in a time scale given by the plasma frequency:

$$\omega_p = \sqrt{\frac{n_e\, e^2}{m_e\, \varepsilon_0}} \tag{1.4}$$

The second criterion defines the role of collective effects. Collective effects dominate the number of particles that are present in a sphere whose radius is equal to λ_D if the quantity denoted as Λ_D is much greater than one. Low collisionality (that means low

level of local coulombic interaction and long range collective effects dominating) implies:

$$\Lambda_D = \frac{4\,\pi\,\varepsilon_0^{3/2}\;T_e^{3/2}}{3\,e^3\,n_e^{1/2}} \gg 1 \tag{1.5}$$

1.3 Plasma magnetic confinement

Plasma can be confined gravitationally, magnetically or inertially.
Stars confine the plasma by means of the only action of gravitational interaction. The thermonuclear reactions provide the energy that prevents the stars from collapsing under the action of their own gravitational attraction. Since these conditions are impractical on Earth, fusion research is focusing the attention on the remaining two branches.
Inertial confinement fusion relies on the heating and compression of a target of deuterium and tritium using laser light. For more information the reader is referred to [2].
The magnetic confinement concept is based on the behaviour of a charged particle in an electromagnetic field. The Lorentz force on a charged particle is given by:

$$\vec{F} = q(\vec{v} \times \vec{B} + \vec{E}) \tag{1.6}$$

Under the action of this force a particle gyrates around the magnetic field lines with a radius and a frequency called *Larmor radius* and *cyclotron frequency*, defined as:

$$r_L = \frac{m\,|v_\perp|}{q|B|} \qquad\qquad \omega_c = \frac{q|B|}{m} \tag{1.7}$$

where $|v_\perp|$ is the module of the component of the velocity perpendicular to the $\vec{B}$ vector. Exploiting these phenomena plasma can be confined by magnetic fields. The best topological configuration to avoid particle losses minimizing one's system boundaries is the toroidal one. In particular magnetic field lines need to be twisted to avoid the drift motions, like the outward $\vec{E} \times \vec{B}$ *drift* [1], that would cause large particle losses in a purely toroidal magnetic field. Three main configurations for twisting the magnetic field lines have been designed in the 50's: the Reversed-Field Pinch (RFP), the stellarator and the tokamak.

1.3.1 Magnetic field-related parameters

Before starting the description of the different fusion reactor concepts it is worth defining a list of three important parameters related to the magnetic field and to the energy confinement.

The magnetic field lines' twist is a fundamental quantity to deal with the problem of the stability of the plasma column. Such topology characteristic is quantified by the safety factor q, which describes the number of toroidal turns that a magnetic field line performs while making one poloidal turn around a magnetic axis. In cylindrical approximation the safety factor q is defined as follows:

$$q(r) = \frac{r\, B_\phi}{R_0\, B_\theta} \tag{1.8}$$

where R_0 represents the major radius of the cylindrical approximation, while B_ϕ and B_θ represent the toroidal and poloidal magnetic field components, while r is the radial coordinate.
The quantity β is a measure of how effectively the applied magnetic fields confine plasma pressure. It can be defined as the ratio between the average kinetic pressure (1.9) and the magnetic one acting on the minor radius of the fusion device (1.10).

$$\langle p \rangle = \langle n k_b T \rangle \tag{1.9}$$

$$p_{mag}(a) = B(a)^2 / 2\mu_0 \tag{1.10}$$

Expressing the magnetic field through the dual contribution of the toroidal and poloidal one, the β factor can be expressed as:

$$\beta = \frac{2\mu_0 \langle p \rangle}{B_{\phi a}^2 + B_{\theta a}^2} \tag{1.11}$$

Ideally, a magnetic confinement reactor device would want to have as high beta as possible, as this would imply the minimum amount of magnetic force needed for confinement. Usually the normalized beta (or Troyon factor) β_N is used as an operational parameter to indicate how close the system is to be strongly destabilized by plasma conditions. Its definition is:

$$\beta_N = \beta \frac{a\, B_0}{I_p} \tag{1.12}$$

with B_0 representing the on-axis magnetic field, a the minor radius of the device and I_p the plasma currant. Typically the maximum reached β_N values are around 4.

1.4 The Reversed-Field Pinch (RFP)

The Reversed-Field Pinch (RFP) is a toroidal pinch configuration (nominally axisymmetric) for the magnetic confinement of fusion plasmas [3], whose main feature is that the toroidal component of the field has the same order of magnitude as the poloidal one. This can be quantified by the Θ pinch parameter, defined as:

$$\Theta = \frac{B_\theta(a)}{\langle B_\phi \rangle} = \frac{\mu_0 a I_p}{2\Phi} \tag{1.13}$$

which is instead employed to discriminate the component of the magnetic field produced by the plasma itself (poloidal) and the one produced by the external coils (toroidal).
Such parameter is proportional to the ratio between plasma current I_p, the minor radius of the torus a, the vacuum magnetic permeability and the toroidal flux Φ. The symbolism ⟨•⟩ represents the average over a fixed poloidal section.
The RFP is similar to the tokamak as both the configurations exploit the pinch effect, i.e. the self-confinement effect obtained driving and electrical current on a plasma embedded in a given magnetic field.
A picture of the mean axis symmetric field is given in Figure 1.2.
A second feature is the reversal of the toroidal component of the magnetic field next to the plasma edge. The small edge value of the toroidal component indicates that the external coils produce a little part of the magnetic field only: this is the signature that magnetic fields in the RFP configuration are produced by the plasma current itself through a process of self-organization.

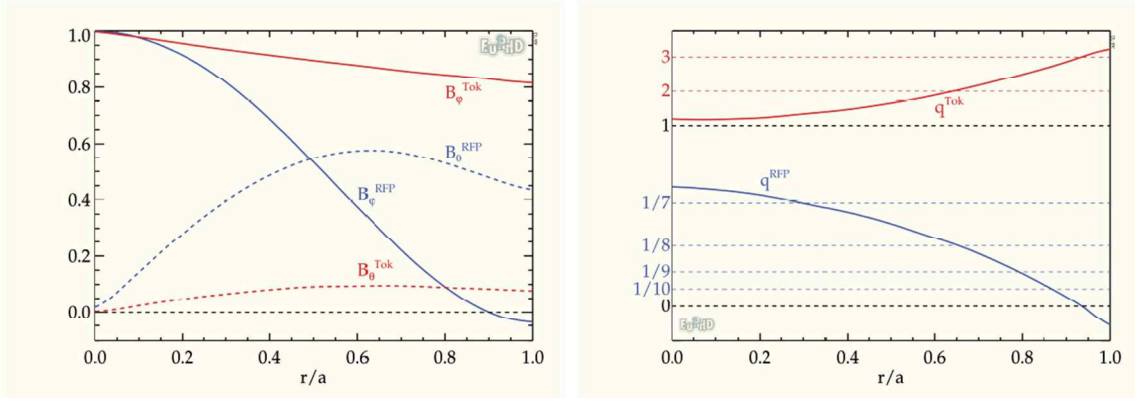

(a) (b)

Figure 1.2 - a) Radial profiles of the toroidal and poloidal magnetic field for a RFP configuration. b) Radial profile of the safety factor.

A parameter, called *reversal parameter*, describes the depth of the reversal of the field at the edge:

$$F = \frac{B_\varphi(a)}{\langle B_\varphi \rangle} \tag{1.14}$$

Such configuration as a self-organized state based on the saturation of a single resistive-kink tearing mode is supported by theoretical, numerical and experimental evidences and eventually leads to a regime of reduced chaotic transport [4]. This paradigm outdates a previous picture of the RFP as a device prone to a heavy turbulent magneto-hydrodynamics (MHD) activity due to the relatively higher current driven in this configuration.
Depending on the ability to further reduce transport, the configuration would have several positive features. For example, with the same on-axis toroidal field the configuration has a much higher value of plasma current, which results in the possibility of heating the plasma through ohmic dissipation without employing additional heating systems.

Furthermore the weaker edge toroidal field implies that a less expensive technology is required to build the reactor's magnets. From the theoretical point of view [5], the favorable MHD stability properties for pressure driven modes leads to the possibility of operating the configuration at a β value higher than the one found in tokamaks.

1.5 The Stellarator

The stellarator configuration was proposed in 1951 in Princeton plasma physics laboratory by Spitzer [6]. The main feature of this configuration is that the field lines' twist is created solely by the action of an external coil system.
This condition, which cannot be satisfied by axisymmetric device, makes the stellarator intrinsically 3D and represents a source of complexity both from the physical and the technological point of view.
The first advantage of the stellarator is that its operations are not limited by the magnetic induction effect of the central solenoid, like in tokamaks and RFPs. A second advantage is represented by the low plasma current (a pressure driven current component, due to toroidal effects, is present despite the original stellarator concept is free from plasma current) that avoids the *disruption* process: a disruption is a sudden loss of thermal energy followed by a fast termination of the discharge.

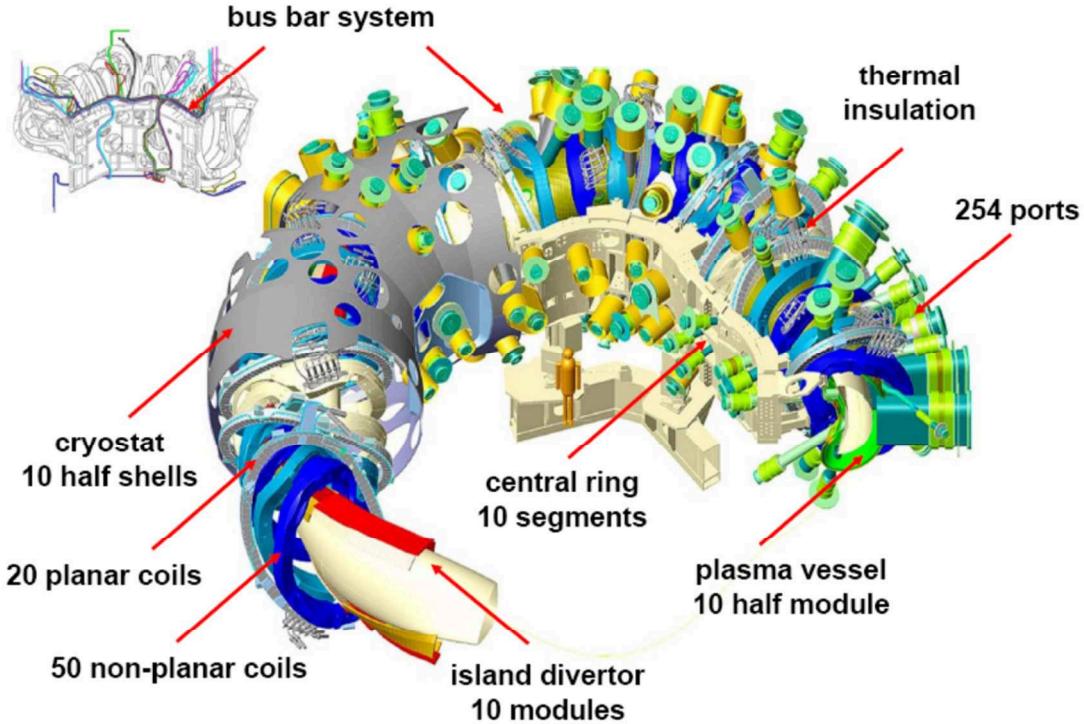

Figure 1.3 - A picture of Weldestein 7-X experiment that has been realized in Greifswald. The main characteristic of the device are: overall diameter 16m, major radius 5m, minor plasma radius 0.53m magnetic field 3T, total weight 725 tons, discharge time 30 mins.

This can cause strong thermal and mechanical stresses on the machine's components, being one of the major causes of concern for the next generation of tokamaks experiments.

The main physical problems of this configuration are the high level of neoclassical transport: this requires an elaborate optimization to achieve the necessary confinement. This optimization process has to deal with a large set of issues: it has to sufficiently confine thermal plasma and fast ions, to allow reliable operations at high plasma densities and pressure and to take into account the role of wall materials and the effect of impurities.
This process has been performed, in particular for the construction of the W7-X (see Figure 1.3) stellarator in Germany [7]: this device should allow operations and MHD stability up to $\beta \approx 5\%$ and a small level of neoclassical transport.

1.6 The Tokamak

The tokamak (being a Russian acronym meaning "toroidal chamber with magnetic coils") configuration was invented in 1952 and in the present days represents the most promising toroidal axisymmetric configuration for fusion plasmas confinement. The plasma is created by the action of a central solenoid that produces a time varying poloidal magnetic flux which induces a toroidal loop voltage. Together with the low but finite plasma resistivity this creates a toroidal current [8].
The toroidal magnetic field is provided by magnets. The poloidal component of the magnetic field, typically a factor of ten weaker, is generated by the plasma current itself, providing the fundamental ingredient for the field lines' twist. In a tokamak Θ is lower than 1, meaning that the magnetic field produced by the plasma itself is much weaker than the one produced by the external coils.

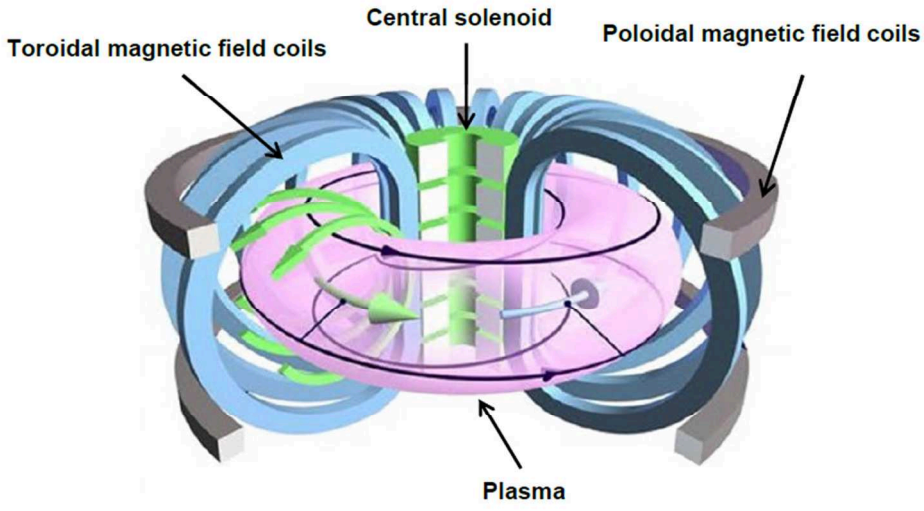

Figure 1.4- 3-D schematization of a Tokamak device.

Plasma pressure and the expansion force of a closed current loop would tend to create a force directed outward that is balanced by a set of so called vertical field coils, mainly employed for the plasma shaping and stability.

The performance of tokamak fusion experiments, measured by the fusion triple product $nT\tau_E$ [1], has grown exponentially in the last decades, representing one of the main successes of this configuration. In the formula n represents plasma density, T the plasma temperature and τ_E the energy confinement time (that measures the scale on which thermal energy from the plasma can be confined).
Plasma ignition, defined as the condition wherein the heating of the plasma given by the fusion reactions is sufficient to replace the energy losses without using external heating, is obtained if the triple product respects the Lawson criterion:

$$n\tau_E T_E \geq 3 \cdot 10^{21} [m^{-3}\ keV\ s] \tag{1.15}$$

The values in time of these important parameters are shown in Figure 1.5.

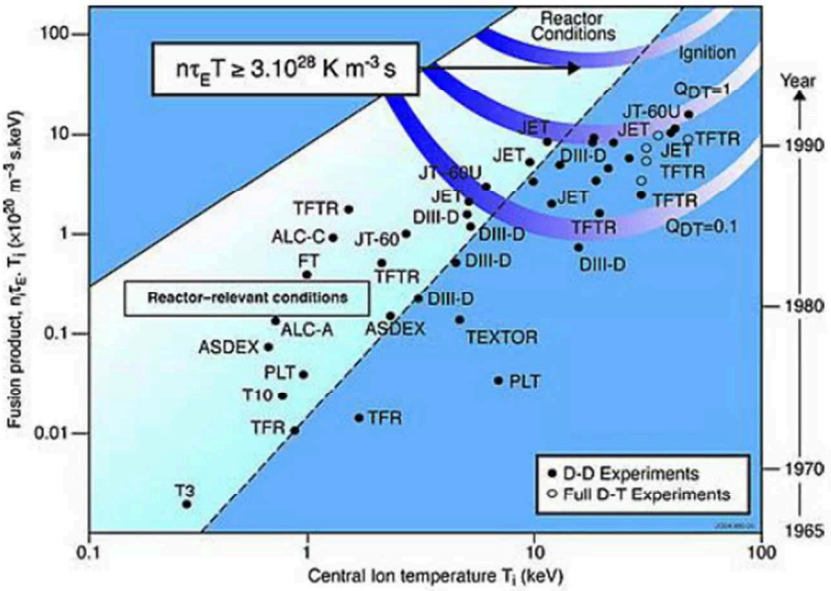

Figure 1.5 – Behavior of the fusion triple product $nT\tau E$ as a function of core temperature (x-axis) and time (right-axis) for different Tokamak experiment D-D or D-T discharge.

The empirical scaling law for the energy confinement time τ_E is shown in Figure 1.6. One important information is the linear increase of τ_E with the plasma current I_p, as described by the quantity labelled on the x-axis and equal to $HI_p^{0.93}P_{heat}^{-0.63}B_\Phi^{0.15}$, with H measuring the quality of the confinement relatively to the scaling law.

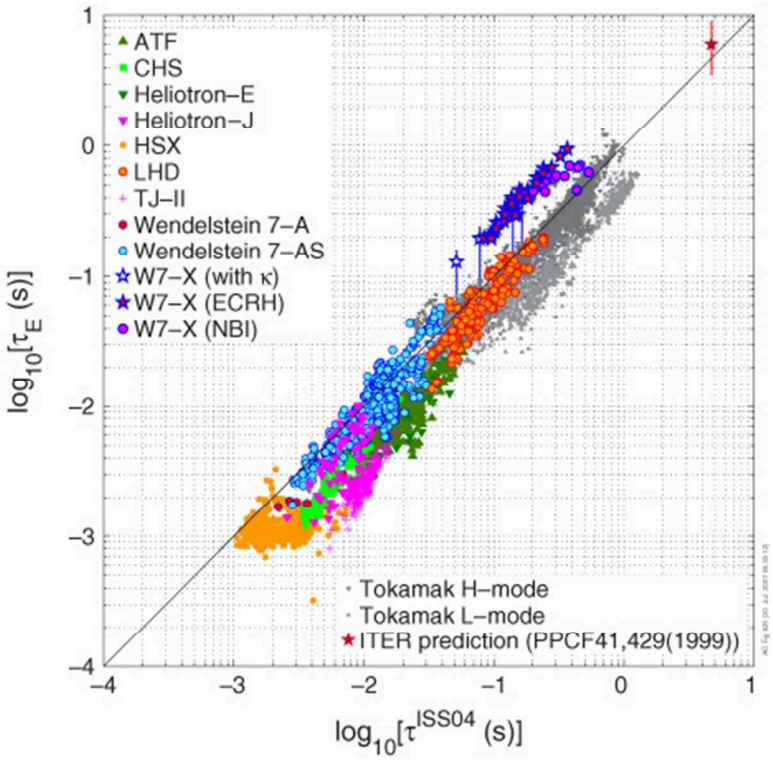

Figure 1.6 - Empirical energy confinement time scalings for the biggest Stellarator (color) and Tokamak (grey scale) experiments in the world.

1.7 ITER

The attention of the international scientific community involved in nuclear fusion research is focused on ITER (International thermonuclear Experimental Reactor) which is the main tokamak under construction in Cadarache (France), where 35 nations are collaborating to build the world's largest device, designed to prove the feasibility of producing net energy and maintain fusion for long periods of time [9].

With ten times the plasma volume of the largest machine operating today, ITER is expected to offer the possibility of studying new physical regimes and technological issues allowing to make a straightforward step towards the demonstration of the technological and economic feasibility of a nuclear fusion power plant (as thought to be addressed by next research step with DEMO experiment).

ITER has been designed to produce 500 MW of thermal fusion power from 50 MW of input power with an amplification factor Q (the ratio between the power produced by the fusion with respect to the external power supplying the reactor) of 10.

Another mission of the device is to prove the feasibility of producing tritium within a reactor environment directly testing mockup in-vessel tritium breeding blankets.

A cutaway of ITER is shown in Figure 1.7 with the indication of the main components. Starting from the outside the stainless steel cryostat (about 29 m x 29 m) ensures a vacuum and cold environment, and surrounds the vacuum vessel and the superconducting magnets. It is used also to protect the reactor from external damages.

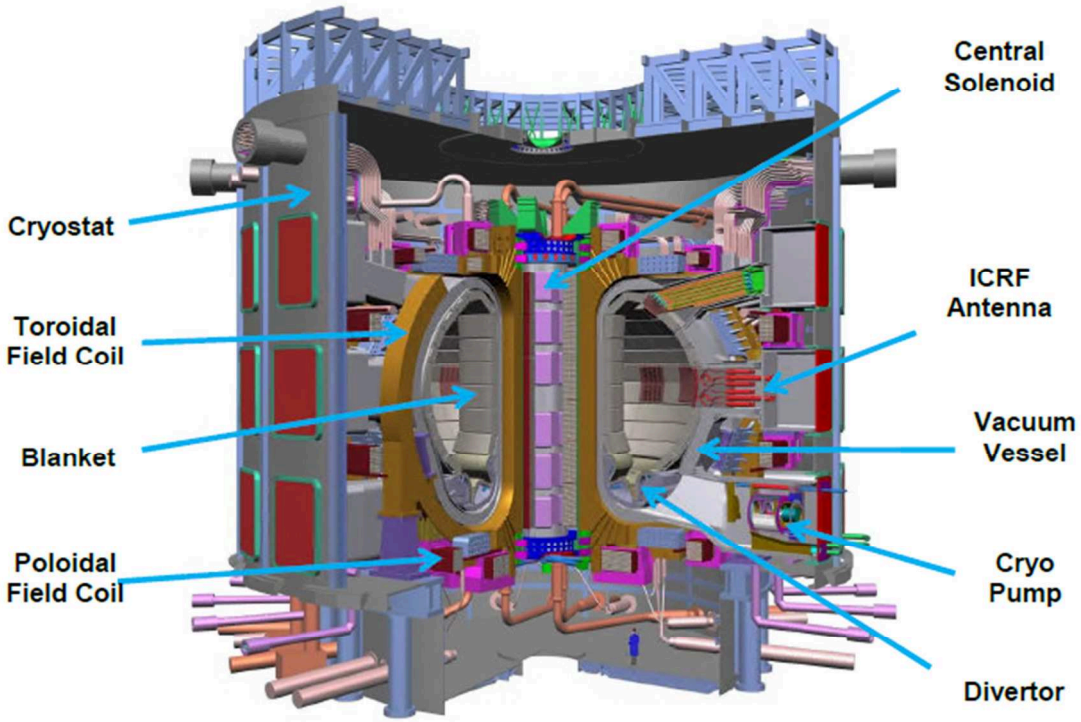

Figure 1.7 - 3D cutaway model of ITER.

Ten thousand tons of superconducting magnets will produce the magnetic fields to initiate, confine, shape and control the plasma. The stainless steel vacuum vessel allows the vacuum environment and acts as a first safety containment barrier. The blanket shields the interior part of the steel vacuum vessel and the external components from the heat load and high-energy neutron fluxes produced during the fusion reactions. On the bottom side of the vacuum vessel the divertor has the main functions of withstand the highest heat flux of the machine and control the exhaust of waste gas and impurities from the reactor.

Three kind of auxiliary heating system are foreseen: neutral beam injectors, ion cyclotron antenna and electron cyclotron antenna. The maximum total power that these systems will supply is 73 MW: 33 MW from the neutral beam injectors (two NBIs - each one delivering a deuterium beam of 16.5 MW with particle energies of 1 MeV - are currently foreseen for ITER), 20 MW from the ion cyclotron antenna and 20 MW from the electron cyclotron antenna.

The main technical data and parameters of the ITER experiment are listed in Table 1.1.

Table 1.1 - Main ITER parameters.

Total fusion power	500 MW	Electron density (n_e)	10^{20} m^{-3}
Amplification factor Q	~10	Average ion temperature $<T_i>$	8.0 keV
Plasma inductive burn time	≥400 s	Average electron temperature $<T_e>$	8.8 keV
Plasma major radius (R_0)	6.2 m	Plasma total external heating	~50 MW
Plasma minor radius (r)	2.0 m	Neutral beam injector	33 MW
Plasma current (Ip)	15 MA	Electron cyclotron antenna (170 GHz)	20 MW
Safety factor (q)	3	Ion cyclotron antenna (50 MHz)	20 MW
Toroidal magnetic field	5.3 T	D-T Plasma volume	840 m^3

1.8 PRIMA Test Facility

Since the required technology for the ITER NBIs is well beyond to the present performance for similar systems, it has been decided to realize a new test facility to solve the scientific gap.
This ITER Neutral Beam Test Facility, named PRIMA (Padova Research on ITER Megavolt Accelerator), is presently under construction in the site of the National Research council (C.N.R.) of Padova (Italy) and will host two experimental devices: SPIDER and MITICA with their relative operation and control dedicated auxiliary systems [10].
The buildings will be built on a surface of approximately 17500 m^2, whereas the area covered by test facility is of approximately 7000 m^2.
Figure 1.8 shows a cutaway of the main building with the disposition of the two experiments while Figure **1.9** shows the plant layout.
The main building is subdivided in two bodies having different height, but the same length of 110 m. The mechanical apparatus of the two devices will be hosted in the main single-span building (1) which covers a surface of 3000 m^2 with a height of 26 m.

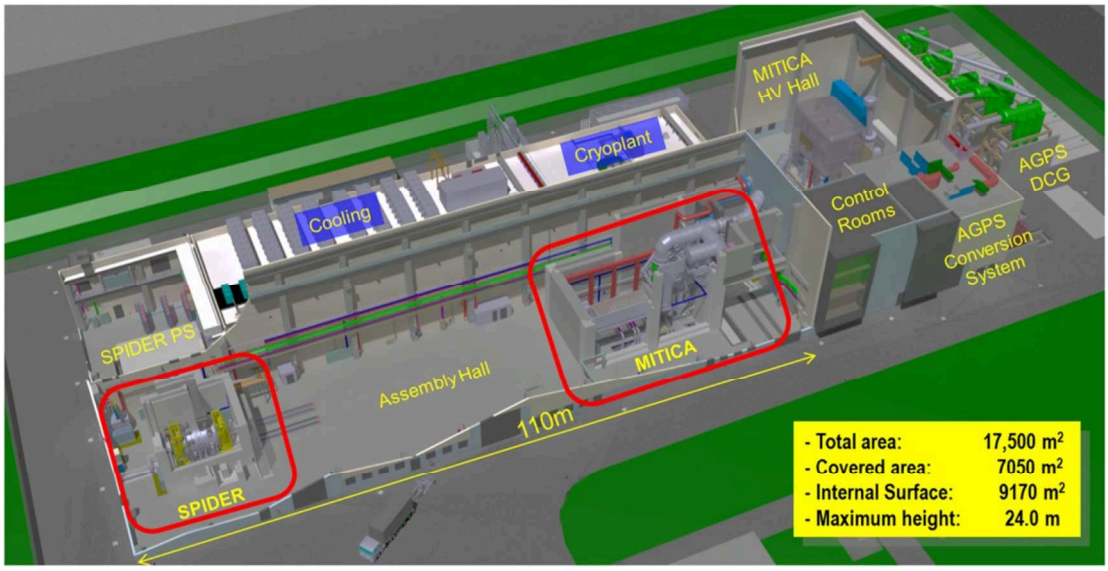

Figure 1.8 - Cutaway of the PRIMA buildings with a view of the two experiments.

A single crane having a total capacity of 50 tons and covering the whole building area will allow the maneuverings and placing of all components to be installed in the experimental devices.
The second body (2), as depicted in Figure 1.9, is adjacent to the first one and has a surface of 2100 m^2; it is partially divided into rooms that are disposed along in two floors. The whole height of the building is 18 m. In order to host on the roof some of the experimental apparatuses the body is divided in two spans to host. In particular some components of the cooling and of the cryogenic plants will be housed here. In order to move the components inside the buildings, two cranes (10 tons maximum weight to be moved) have been foreseen for each span in the single floor rooms.

A second body of buildings is composed of two rooms; the first one (3), see Figure 1.9, with a surface of about 800 m² and a height of 26 m will host a -1 MV shielded deck, containing power supply systems and other devices set at -1 MV voltage with respect to ground potential. The second room (4), see Figure 1.9, having a surface of 400 m² and 17 m height has two floors and hosts other power supply systems and utility devices.
A final building (5), see Figure 1.9, connecting the previous ones, will host two experiment control rooms; computers, network devices and data storage systems.
In the external area, other systems and components necessary for the experimental plant operation are located: the MITICA acceleration grid power supply, hosting five secondary 200 kV transformers series-connected in order to reach the voltage value of -1 MV (6), the underground -1MV transmission line (7) and two underground water basins which serve as cooling system heat sink (8).

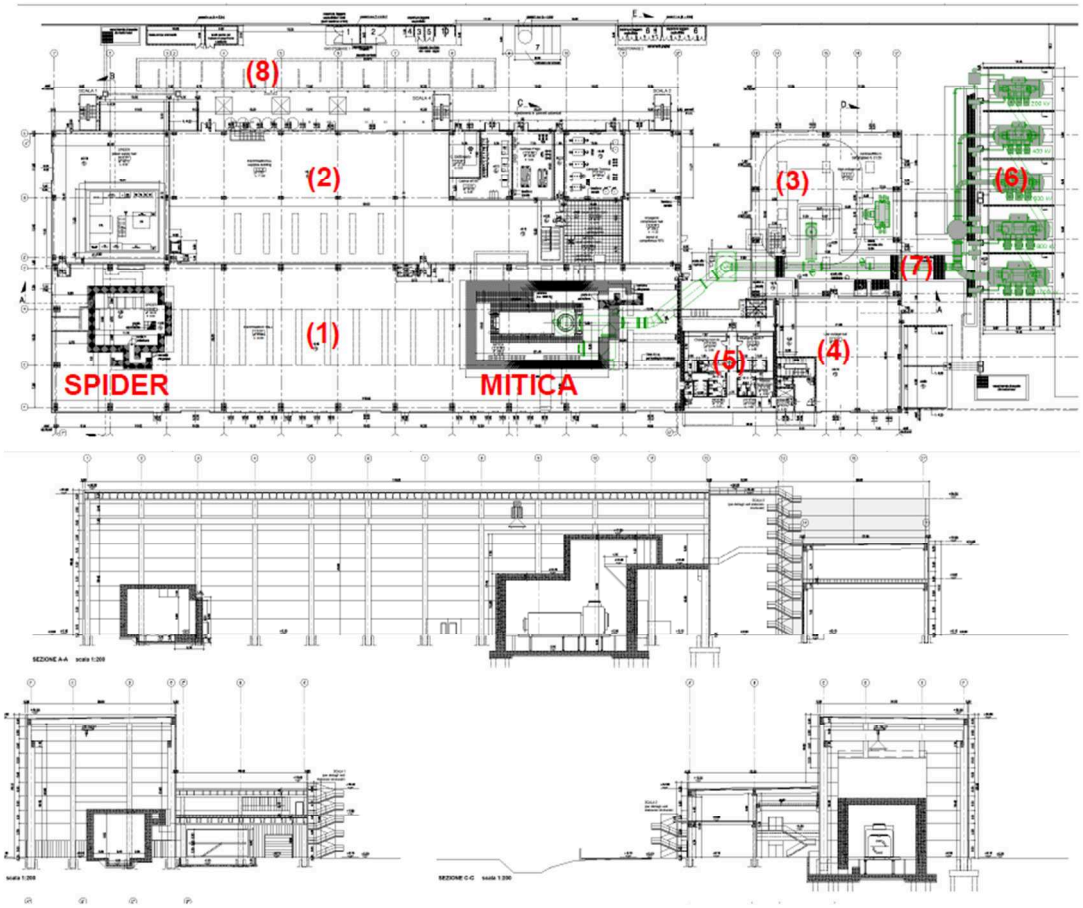

Figure 1.9 - PRIMA buildings, layout and side views.

1.9 SPIDER

SPIDER (Source for Production of Ion of Deuterium Extracted from Radio-frequency plasma) is the former experiment to go under operations (final delivery has been in October 2017, conditioning is expected to conclude in March 2018) and has the target to test, develop and optimize one of the most critical and complex components for future

injectors negative ion source. Such device is therefore not a full-scale version of the neutral beam device, since it is mainly focused on the first steps of the process for the realization of a neutral beam. The process for the production of deuterium neutral particles originates from deuterium (D) plasma produced by means of 8 inductive radiofrequency generators (operating at 1 MHz) in a chamber 1.8 m high, 0.6 m wide and 0.2 m deep (Plasma Source). Such volume faces a surface (Plasma Grid) previously covered with a caesium layer, whose interaction with Deuterium can generate a deuterium ion having one additional electron (D^-). The D^- is created either by reactions within the plasma or by volume surface reactions.
The potential close to the Plasma Grid is controlled by the Bias Plate. Downstream to the Plasma Grid (PG) two others grids are designed respectively for negative ion extraction (Extraction Grid – EG) and acceleration (Grounded Grid – GG).
The mission of SPIDER is to guarantee on a large extraction surface (1.52 m x0.56 m) the following ITER parameters for Hydrogen and Deuterium operations:

Table 1.2 – SPIDER nominal parameters

SPIDER	Unit	H	D
Beam Energy	[keV]	100	100
Maximum Beam Source Pressure	[Pa]	<0.3	<0.3
Uniformity	[%]	10	10
Extracted Current Density	[A/m^2]	>350	>290
Beam pulse duration	[s]	3600	3600
Co-extracted electron fraction	[e^-/H^-] [e^-/D^-]	<0.5	<1

The electrostatic accelerator located inside such experiment will therefore operate with reduced electric potential (100 kV) with respect to the ITER designed one (1 MV) and no neutralization of the beam will be performed.

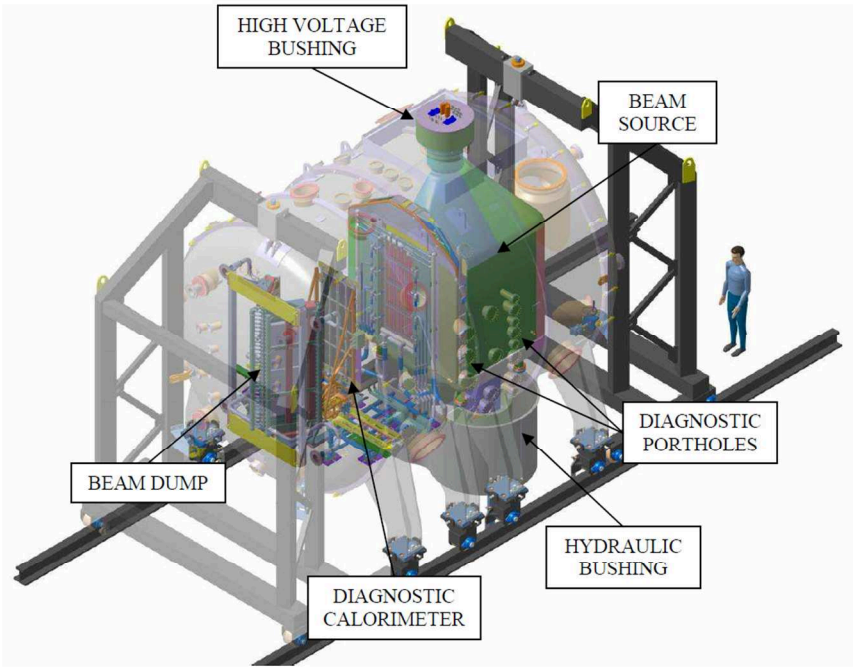

Figure 1.10 - SPIDER experiment with transparent vessel.

A tailored diagnostic system will provide the possibility of measuring parameters related both with the generated beam and with the study of source operational modes with the aim of realizing further developments to the system.
An overall picture of the whole device can be seen in Figure 1.10.

1.10 MITICA

The MITICA (Megavolt ITER Injector & Concept Advancement) experiment constitutes the full-scale prototype of ITER NBI. Its final objective is the optimization of the performance of the injector in all the possible operating working scenarios till reaching the goal of providing a wide through reliable system to be coupled with the fusion reactor in Cadarache.
MITICA and SPIDER share the same design of the Plasma Source, the Bias Plate, the Plasma Grid (PG) and the Extraction Grid (EG). What differs among the two sources is essentially the presence of hydraulic connections of "flanged type" in SPIDER rather than "welded type" as designed for MITICA.
The ion source is held at −1 MV and the D^- ions are accelerated up to ground potential by a system of 5 grids set at different growing potentials, by steps of 200 kV.
The composition of the ion source and the accelerator stage is called Beam Source. Once the acceleration stage is performed, the beam will then pass through the Neutralizer where a cloud of deuterium gas neutralized the ion beam through a charge exchange process.
At the exit of the neutralization process, the beam will pass through an electrostatic field (Residual Ion Dump, RID). The electric field deflects the charged particles of the beam onto a set of plates, leaving the neutral beam to impinge onto the calorimeter located just downstream of the residual ion dump.
In this configuration the injector can be commissioned and the neutral power dumped onto the calorimeter can be measured. For a detailed description of the neutral beam injector system the reader can refer to paragraph 2.9 in Chapter 2.
In the ITER NBI, the calorimeter will be opened and the neutralized deuterium beam of 16.5 MW power will flow along the duct until the ITER plasma is reached.
What characterized MITICA from the foreseen NBI designed for ITER is the insertion of several diagnostic systems able to provide the measurement of a variety of generated beam parameters, in all the different phases, and validate the accuracy of injector design development. The nominal parameters of the MITICA injector are reported in Table 1.3.

Table 1.3 – MITICA nominal parameters.

MITICA	Unit	H	D
Neutral beam power	[MW]	16.5	16.5
Beam Energy	[keV]	870	1000
Acceleration current	[A]	49	40
Maximum beam source pressure	[Pa]	<0.3	<0.3
Beamlet divergence	mrad	≤7	≤7
Beam pulse duration	[s]	3600	3600
Co-extracted electron fraction	$[e^-/H^-]$ $[e^-/D^-]$	<0.5	<1

2

2. Neutral beam injector systems

Neutral Beam Injector (NBI) systems are used to launch uncharged high-energy particles into the plasma where, by means of collisions, they transfer their energy to the plasma ion and electron population [11]. One of the main advantages of injecting energetic neutrals particles lies in the fact that these particles can travel unaffected through the magnetic fields present inside the reactor chamber and eventually transfer the energy to the plasma through successive collisions.
Before injection, deuterium atoms need to be accelerated outside of the Tokamak to a high kinetic energy, namely comprised in the range of 100 keV and 1 MeV.
In order to perform the accelerating stage to the desired energy through electrostatic phenomena the initial deuterium gas has to be ionized either positively or negatively.
Since the electrically-charged ions would be deflected by the magnetic field surrounding acting into the toroidal reactor chamber, the beam has to be neutralized again before the final injection into the fusion plasma.
The large plasma volume of ITER will impose new requirements on this proven method of injection: the particles has to be characterized by an energy which has to be the double of the most energetic NBI presently operating (500 keV in JT 60-U experiment) in order to penetrate far enough into the plasma.
Present chapter covers the main physical and technological aspects of neutral beam injector related to the present and future NBI machines. Particular attention will be given to the components characterizing such devices.

2.1 The quest for additional heating systems

The power balance of a fusion reactor is given by the relation expressed in Equation 2.1:

$$\frac{\partial W}{\partial t} = P_R + P_H - P_L \tag{2.1}$$

where W is the plasma energy density, P_R is the power per unit volume produced by the fusion reactions, P_H the auxiliary heating per unit volume and P_L the power loss per unit volume. In neutral plasma, where the ion and the electron population density (n) have both fully thermalized at the same temperature T, the energy density can be approximated to $3nT$.
In first approximation the particles can be considered equally divided between Tritium and Deuterium species.

$$n_e \sim n_i = n_D + n_T \tag{2.2}$$

In a stationary regime during a plasma discharge, the energy losses have to be compensated by the power released by the alpha particles during their thermalization subsequent to the fusion process. In case the balance between these two quantities is not reached, the reaction inside the reactor cannot be sustained and additional heating systems are required.

$$P_{Heating} + P_\alpha = P_{losses} \tag{2.3}$$

Such additional heating power can be therefore described as the difference between the power density losses (seen as the thermal energy divided by the energy confinement time τ_E) and the power of the alpha particles (expressed in terms of the reactants cross section).

$$\begin{aligned} P_{Heating} &= (p_{losses} - p_\alpha) Vol \\ &= \left(\frac{3nT}{\tau_E} - \frac{1}{4} n^2 < \sigma v > E_\alpha\right) Vol \end{aligned} \tag{2.4}$$

$$\tau_E \propto 1/T \tag{2.5}$$

In Equation 2.3 n represents the ion density.
For fusion reactions τ_E is a known parameters and experimental results can readily show its dependency on temperature and on the fuel mix that is employed in the discharge.
The contribution related with the power losses can be described in the simplest way with a parabolic behaviour over temperature, whereas the alpha particle heating can be described taking into account the cross section distribution in the energy spectrum.
The self-sustained fusion reaction process is therefore realized at the intersection of the two characteristics. Such intersection is obtained in two different points. The former, at the lower temperature, is associated to an unstable equilibrium, while the latter to a

stable one. For D-T plasma operation the unstable equilibrium ignition is realized at 13 keV, whereas the stable conditions are reached at a temperature of about 16 keV as illustrate in Figure 2.1 and Figure 2.2.

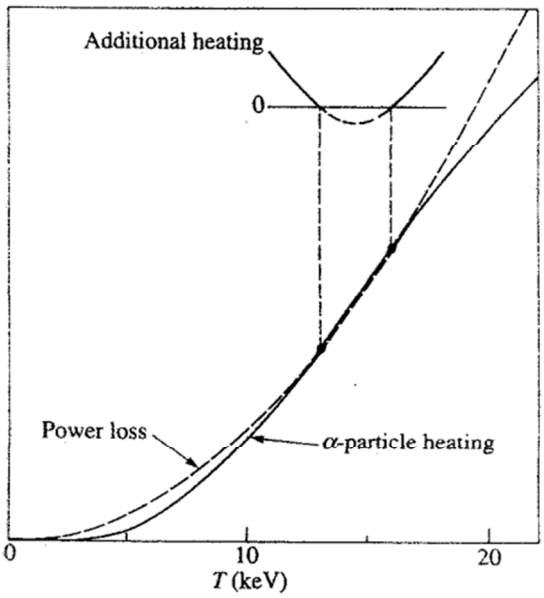

Figure 2.1 – Power loss and α particle heating contributions in the temperature spectrum.

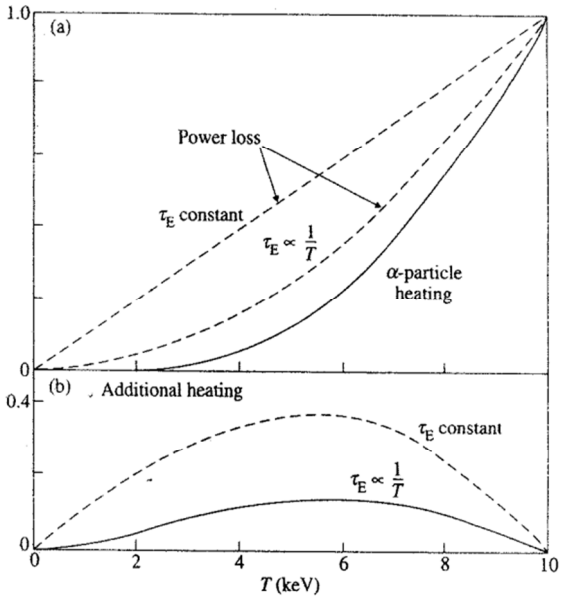

Figure 2.2 – Zoom of the intersection region between power loss contribution and α particle heating (a) and resulting quest of additional heating as a percentage of P_α (b).

The restricted temperature interval 0-10 keV, depicted in Figure 2.2, highlights the amount of additional heating that is needed to cover the gap between the alpha power and the losses.

For plasma at a temperature of 6 keV the additional heating contribution reaches its maximum whether the energy confinement time is described as a constant or with temperature dependence behaviour.

$$15\%\ \text{of}\ P_\alpha \qquad \tau_E \propto 1/T \tag{2.6}$$

$$40\%\ \text{of}\ P_\alpha \qquad \tau_E \sim \text{constant} \tag{2.7}$$

Taking into consideration a thermal power from fusion reaction processes of 1 GW, due to momentum conservation, the P_α recovered from the full thermalization of alpha particles can be estimated in the order of 200 MW (1/5 of the global power). The global amount of the needed additional power is then:

a) 30 MW (3% of the overall power) considering an energy confinement time that evolves with temperature;
b) 80 MW (8% of the overall power) assuming a constant behaviour of the energy confinement time with temperature.

2.2 Additional power heating systems

In fusion experiments such additional power heating contribution can be supplied exploiting three different principles: ohmic power, radiofrequency and neutral beam particle injection.

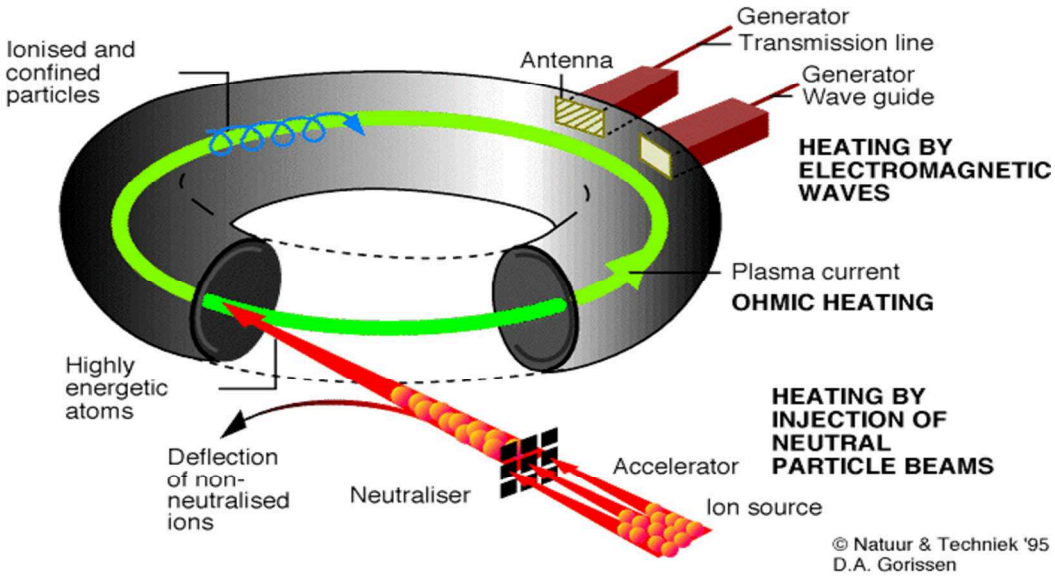

Figure 2.3 – Additional heating power systems in a fusion reactor.

The ohmic power has dependence with $T^{-3/2}$ leading this additional heating method to be ineffective at high temperature. In a reactor comparable with a DEMO (Z_{eff}=1.5, V=2000m^3, T=10keV) it would be possible to supply a contribution of just 6 MW with this external heating method.

In order to cover the additional heating power contribution required by a future commercial fusion reactor (in the order of 80 MW), two different concepts have been developed.

The former involves electromagnetic waves which directly heat the ionized particles in the plasma by means of Ion or Electron Cyclotron (IC/EC) device, the latter is instead realized through the neutral beam injector concept which realizes a momentum transfer to ions and electrons contained inside the plasma exploiting the injection of high energetic neutral particles.

2.3 Atomic processes during a ionization of a neutral particles and beam penetration distance

The five main atomic processes that lead to the absorption of a deuterium beam inside plasma can be summarized in the Table 2.1:

Table 2.1 - Basic atomic processes during ionization of a neutral beam in high temperature plasma (the subscript b stands for beam, whereas D and A stand respectively for Deuterium and Impurities).

Charge exchange	$D_b^0(1s) + D^+ \rightarrow D_b^+ + D^0$
Ionization by ions	$D_b^0(1s) + D^+ \rightarrow D_b^+ + D^+ + e$
Ionization by impurities	$D_b^0(1s) + A^{z+} \rightarrow D_b^+ + A^{z+} + e$
Impurity CX	$D_b^0(1s) + A^{z+} \rightarrow D_b^+ + A^{(z-1)+}$
Ionization by electrons	$D_b^0(1s) + e \rightarrow D_b^+ + 2e$

All these processes are associated to specific cross sections depending on the energy of the deuterium beam.

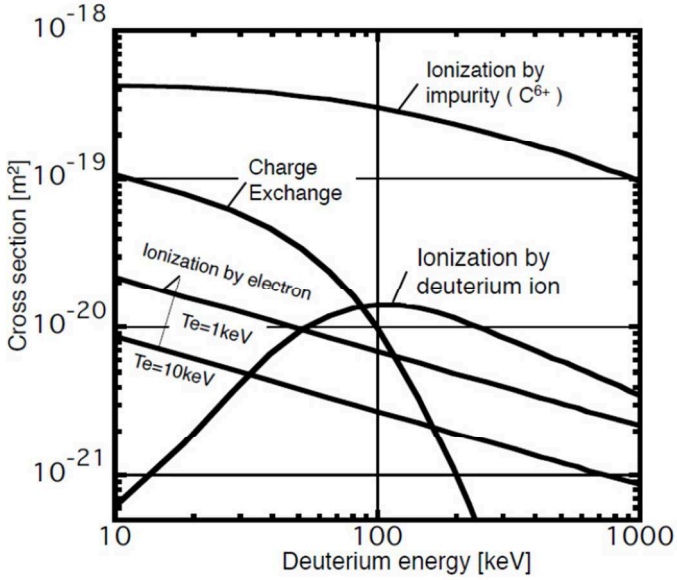

Figure 2.4 – Atomic ionization process cross sections.

In a logarithmic scale the ionization by electrons is more or less described by a straight line, whose interception with the y-axis is correlated to the temperature of the electrons population. The cross sections related with charge exchange and ionization by impurity show a monotonically decrease with the energy of deuterium beam while the ionization by deuterium ion is instead characterized by a maximum at 100 keV and then decreases to one half of this maximum value at 1 MeV.

It can be noticed that around 90 keV the ionization by Deuterium atom and the charge exchange curves intercept. As a consequence at lower energy the leading ionization process between Deuterium atoms is the Charge Exchange while at higher energy the dominant absorption phenomenon inside the plasma is the ionization one.

The cross section related with the ionization by impurity depends as a matter of fact both on the type of impurity contained in the plasma and on its ionization level. Typically the charts report C or W impurity ionization cross section depending on the case the considered machines are carbon or tungsten ones.

The absorption of the beam along its trajectory can be expressed in terms of its flux intensity *I(x)*.

$$dI(x) = -\Sigma \cdot I(x) dx \qquad \text{where } \Sigma = n \cdot \sigma \qquad (2.8)$$

This variation of the beam intensity depends on the overall cross section (σ) of the phenomena introduced so far. Multiplying the cross section of the different absorption contribution by the density of beam (n) it is possible to define the macroscopic cross section (Σ).
The differential law of absorption can be then globally defined as:

$$\frac{d}{dx} I_{beam}(x) = -\left(\frac{n_i(x)}{n_{el}(x)} \sigma_{ChEx} + \frac{n_i(x)}{n_{el}(x)} \sigma_{ion} + \frac{n_z(x)}{n_{el}(x)} \sigma_z + \frac{\langle \sigma_{el} v_{el} \rangle}{v_{beam}} \right) n_{el}(x) \cdot I_{beam}(x) \qquad (2.9)$$

In this expression the different population densities that are involved in the absorption process are all normalized on electron density $n_{el}(x)$.
With a plasma density in the order of 10^{20} particles/m^3 and with an energy of the beam of approximately 100 keV, the sum of the different cross section for the various absorption processes is in the order of $3 \cdot 10^{-20}$ m^2. The associate macroscopic section is therefore given by the product:

$$\Sigma = n \cdot \sigma_{tot} \sim 3 \text{ m}^{-} \qquad (2.10)$$

It is possible to obtain the characteristic decay length from the inverse of the macroscopic cross section (33 cm). Such length individuates the distance over which the 63% of the beam is absorbed.
In a JET-like reactor [http://www.ccfe.ac.uk/JET.aspx] where the plasma minor radius in the order of 1m it is then possible to perform the 63% of energy absorption of a perpendicularly injected beam in 1/3 of the radial dimension of the machine.
Since the absorption of the power carried by the particles has to be realized in the plasma core region (and not at the edge where losses would be relevant) the energy of the beam should be correlated with the characteristics of the fusion reactor.
If the beam energy is too low with respect to the appropriate one the absorption would be localized just at the plasma edge. A practical example of having a beam with a too low energy is given by what is presently occurring in JET machine during high performance discharge. The energy of the beam is in fact limited to 120 keV, and this is not sufficient for particles to transfer their energy up to the center of the plasma, leading the energy to be deposited mostly at the edge of the JET plasma.
On the contrary if the beam energy is too high the absorption inside the plasma would result incomplete leading part of the neutral particles to cross completely the reactor chamber and eventually depositing their residual energy on the first wall surfaces opposite to the injector.
This phenomenon is called Shinethrough and is a very risky condition for the operation of the NBI since it could eventually lead to destroy part of the first wall.
As a matter of fact the level of energy associated to the injected particles should be a tradeoff between the two values associated with the absorption at the plasma edge and the shinethrough threshold.
As a matter of fact in a reactor where the minor radius is much bigger than the one in JET (2-3 m instead of 1m) the deposit of the energy in the center of the plasma can be

then realized on condition that the beam is supplied with an energy much higher than 100 keV.

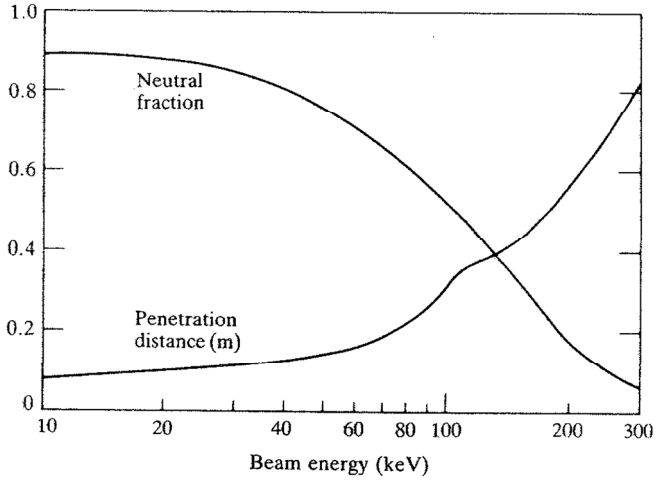

Figure 2.5 – Deuterium beam penetration distance and neutral fraction efficiency with a plasma and beam density of 10^{20} m^{-3}.

Being the beam accelerated by means of successive electrostatic grids during the acceleration step, the generated particles should be initially characterized by a net charge in order to interact with the generated electric fields of the grids. Notwithstanding the accelerated beam has to be introduced in the plasma chamber as neutral. It is therefore necessary to implement between the acceleration step and the beam introduction into the torus a neutralization step. Figure 2.5 depicts the efficiency of such neutralization process and the realized penetration distance inside the plasma for positive beams in the range 10-300 keV. At 300 keV, it is possible to notice that the associated characteristic length for the deposition of the 63% of beam energy is 0.8 m. However beyond this energy level the efficiency per unit length of the neutralization process of the positive ions is dumped to very low values.
In JET during the operation with hydrogen ions the neutralization efficiency at 100 keV is less than 30% (H beam neutralization is worse than D ones). As a matter of fact the 70% of the injected particles remains ionized and cannot be introduced into the plasma. In case these ionized particles reached the volume where high magnetic field are present, this high energetic population would be deviated and dumped on some components of the machine, with the consequent risk of destroying the vacuum vessel or the duct necessary for the connection of the beam to the plasma itself.

2.4 Positive and negative injected beams

In fusion experiments two different kinds of ion beams have been developed. The former type is the one derived from the acceleration of positive ions while the latter takes advantage from the acceleration of negative ones. The reason on the basis of developing these two different concepts of ion beam lies in the neutralization performance at difference energy level.

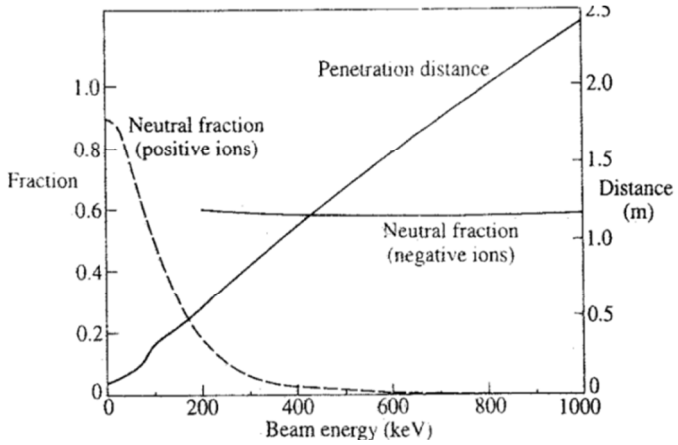

Figure 2.6 – Neutralization efficiency for positive and negative ions accelerated beam.

At very low energy (up to 50 keV) the fraction of neutralized positive ions per unit of length along the neutralizer is between 80-90%.
Increasing the energy above 100 keV the neutralization efficiency is reduced to 40%, at 200 keV to 20%, while at 400 keV almost any particle experiences neutralization process since at these energies there is no sufficient time for the interaction between the ion and the gas to attach the electron to the former.
At high energy positive ions have therefore such small cross section with neutral particles (or impurities) that is impossible to neutralize the associated beam up to a reasonable fraction.
This is the reason why if the penetration distance required into the plasma is in the order of 1-2 m, like for ITER and DEMO experimental reactors, the only possibility to achieve such performance is to rely on accelerated negative ions, whose neutralization efficiency for a plasma density of $n=10^{20}$ m^{-3} is in the order of 55%.
The drawback to pay in order to achieve this higher neutralization efficiency is the higher complexity in the production of negative ions. If on one hand the creation of positive ions is quite easy to be performed by stripping process of the single electron in H or D atoms, on the other the attachment of the second electron is rather more difficult, with the created negative ion specie furthermore characterized by with very short lifetime and mean free path.

2.5 Momentum transfer in ion and electron populations

Due to the different cross section between electrons and ions contained into the plasma, the transfer of momentum from the energetic neutral particles to these species is governed by different relations.

$$P_{Heating} = P_{Heating-elct} + P_{Heating-ion} \tag{2.11}$$

$$P_{Heating} = A_{Beam}\left(B_{el}\frac{E_{Beam}}{T_e^{\frac{3}{2}}} + C_{ion}\frac{1}{E_{Beam}^{\frac{1}{2}}} \right) \tag{2.12}$$

Where:

$$A_{Beam} = m_{Beam}A_D = m_{Beam}\frac{ne^4 \ln\Lambda}{2\pi\varepsilon_0^{\,2} m_{Beam}^{\,2}} \qquad B_{elct} = \frac{2m_e^{\frac{1}{2}}}{3(2\pi)^{\frac{1}{2}}}$$

$$C_{ion} = \frac{m_{Beam}^{\frac{3}{2}}}{2^{\frac{3}{2}} m_{ion}^{\frac{1}{2}}} \qquad E_{Beam} = \frac{1}{2}m_{Beam}v_{Beam}^{\,2} \tag{2.13-2.16}$$

As expressed from Equation 2.12 the plasma heating addressed by electrons is proportional (through some coefficients) to the energy of the beam divided by $T_{el}^{3/2}$, while the contribution given by the ion heating is proportional to the inverse square root of the beam energy.

As a consequence the contribution to electrons heating, which is mainly realized through the slowing of beam particles rather than scattering, increases with the increase of the energy of the beam. The ion heating, which is instead realized through scattering and loss of parallel energy, is characterized by the opposite behavior and its contribution is higher the lower is the energy of the beam. The coefficients A,B and C are expressed through the Equation 2.13-2.16.

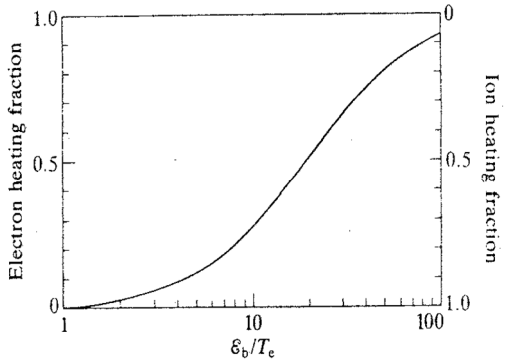

Figure 2.7 –Electron and Ion heating fraction distribution with respect to the ratio of beam energy over electron temperature.

The relative weight for ion and electron heating is summarized in Figure 2.7 having in the abscissa the ratio between the beam energy and the electron temperature.

The resulting curve discriminates on the left side the electron heating fraction and on the right side the ion heating one. For high energetic beam (with respect to electron temperature) the heating is then essentially transferred to the electron population and not the ions one.

In order to increase the penetration (and energy deposition) distance associated to the beam it is mandatory to increase the energy of beam, thus exploiting the acceleration of negative ions (as positive ions would result impossible to neutralize). However for high penetrating beam, the transfer of momentum is mostly concentrated to electrons (and very little to ions) and therefore in order to reach a uniform temperature of the

plasma it is either necessary to wait for the thermalization of the two species or realize specific additional heating system tailored for the ion population (e.g. Ion cyclotron design for ITER).
In the case of ITER, with T_e around 10-20 keV and an associated beam prescribed with an energy in the order 1 MeV, it results that the 10% of the beam heats the ions while the remaining and 90% deposit momentum to electrons.
In JET where the ratio between E_b/T_e is much smaller due to the lower energy of the beam (E_b =100 keV, T_e =10 keV) the contribution to electron heating reaches 35% (and 65% of ions).
As far as the plasma heating performances from NBI are concerned, the record for ion heating at low energy (hence with positive beam injectors) was reached in 1996 in JT-60. During a pulse in H-mode configuration the ions have been heated up to 45 keV, while electrons were delivered with around 10 keV (4 time less).

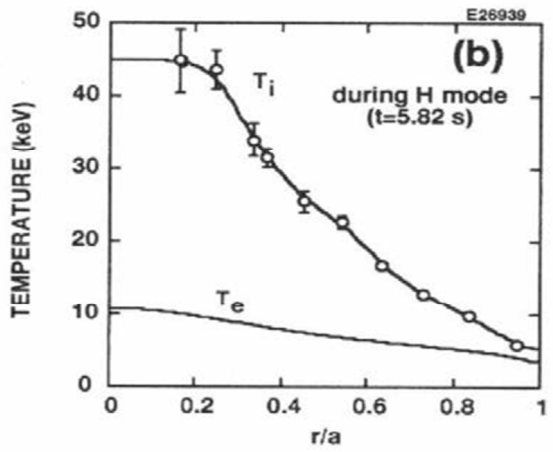

Figure 2.8 – Electron and ion temperature profile during an H-mode impulse in JT-60 in 1996.

2.6 Additional effects produced on plasma through NBI

During the stationary operation of a fusion reactor the contribution given by the additional heating is, in principle, not needed due to the excess of power released by alpha particles. In reality the additional heating system could not be turn completely down due to the request for plasma fueling, plasma rotation and current drive (addressed by the physical injection of Deuterium atoms or momentum transfer performed by the NBI) or impurity control (addressed by Electron and Ion Cyclotron).
In addition it is important to remember that the need of additional heating in a fusion reactor is even associated to perform the transition from L to H mode during the transient phase in the start-up of the plasma.
As far as the plasma fueling is concerned the particle flux intensity associated to the neutral beam is the most important characteristic as it directly affects the feeding of one of the reactants (D).

In JET, whose NBI operates at 100 keV, the plasma fueling is therefore dominated by the particle injected by the neutral beam (67% of the fueling). Considering the fact that the power associated to an injector is determined by the product beam energy times beam particle, it is straight forward to note that in ITER, where the NBI operates at 1MV, in order to inject into the plasma the same power as JET, the fraction of injected particles shall be ten times lower. As a matter of fact even the fraction of fueling is essentially ten times lower (in the order of 6-7%).

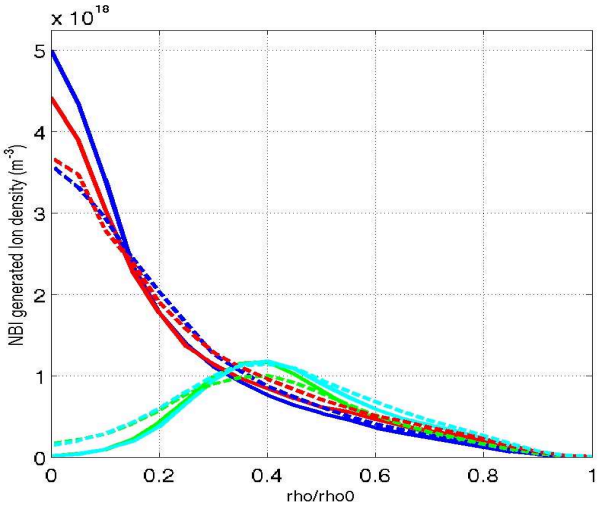

Figure 2.9 – NBI plasma density contributions in on and off axis injection tests. Blue and red profiles refer to the density profile in FAST reactor, the dashed ones depict the initial distribution (beam off), while solid one the distribution obtained during NBI operations. Green and light blue curves illustrate instead the ion density contribution proper of the NBI.

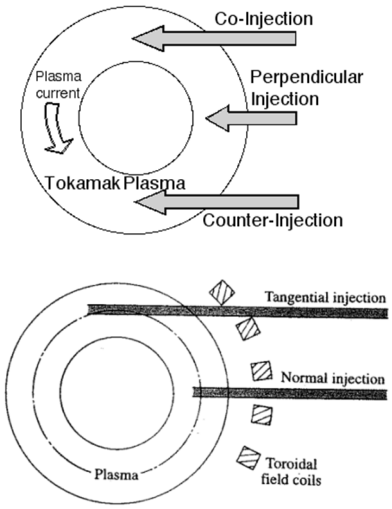

Figure 2.10 – Possible NBI injection configurations (a) and spatial constraints imposed by the presence of the toroidal field coil system.

Figure 2.9 depicts some analyses that have been carried out for FAST [http://www.fusione.enea.it/PROJECTS/FAST/index.html.en]. The objective of such activity was to study the effect in terms of plasma density resulting from on and off axis injections. Regardless to the characteristics of the injection, the contributions in density are in the order of $4\text{-}5 \cdot 10^{18}$ m^{-3}, a few percent of the plasma density foreseen inside the reactor (10^{20} m^{-3}). Even in this case the density contribution realized by the NBI is small and in the same term of ITER.

The induced plasma torque consists in the mutual toroidal rotation of both ion and electron species, thus not generating a net current. This effect is sought in order to move instabilities along the toroidal direction leading them to be dumped before they could propagate to the first wall.

The neutral beam can be inserted into the plasma with perpendicular, co- or counter-injection configurations. In order to prevent the shinethrough, and therefore realize a more uniform absorption inside the plasma with an increase of absorption length and current drive efficiency, it is suggested to inject the neutral particles in a tangential mode (and in particular in a co-injection configuration). However with such kind of configuration the toroidal field coils impose some constraints in the choice of the

injection angle and further pumping requirements are hence needed for the longer drift ducts of the NBI. As a result the selection of the injection angle in such configuration has necessarily to be a trade-off between these constrains.
On the other hand with a co-injection configuration it is however possible to induce an additional rotation to the plasma in the order of 30-40 krad/s (cf. ITER with 2-3 NBIs). This contribution is not so relevant with respect to the neutral rotation frequency of the plasma but however it helps for the control of instabilities.
In some experiments, like D-IIID or ASDEX, there are two injectors, each of them introducing particles either in co or counter directions in order to make experiments on the effects of introducing different additional momentum with respect to the plasma reference rotation.
Among the additional effects produced on plasma reactors through NBI, the current drive is the most important feature. The Tokamak concept as the basis for a steady-state, electricity producing power plant cannot indeed be achieved without a source of high-power current drive to sustain the plasma for long periods of time.

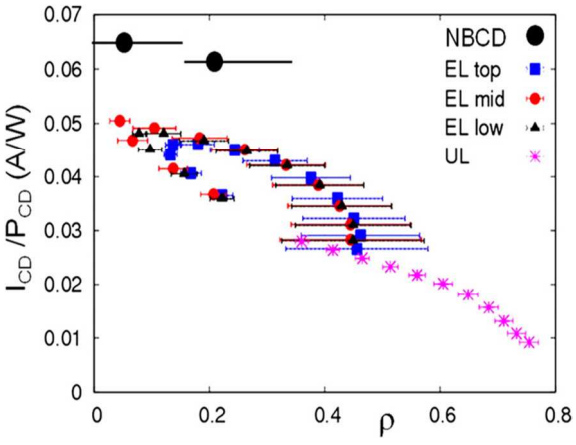

Figure 2.11 –Current drive contribution with respect to the total power introduced by additional heating systems along the radial direction of a reactor.

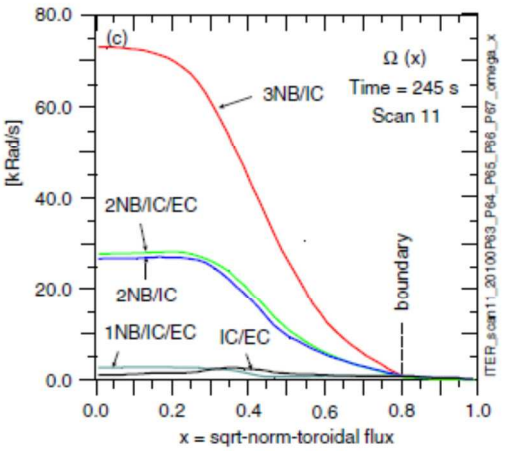

Figure 2.12 – Evaluation of current drive contributions for different configuration of additional heating operating systems along the radial direct5ion of the reactor.

Figures 2.12 and 2.13 depict the induced current drive with respect to the injected power for different configurations of heating systems: electron/ions cyclotron (IC/EC) and neutral beam (NBI). As far as current drive is concerned the neutral beam heating system option reveals to be much more effective than the other ones.
The evaluation of the beam driven current to be realized in future experiment has been performed starting from experimental results on which coherent numerical models have been built. Equations (2.17) and (2.18) are the ones taken as a reference in order to evaluate the driven current drive efficiency.

$$\eta_{CD} = 0{,}2 \cdot 10^{17} \cdot \sqrt{E} \cdot T_e^{\frac{3}{2}} \qquad (2.17)$$

$$I_{CD} = \frac{\eta_{CD} P_{NBI}}{n_e R_0} \qquad (2.18)$$

Where E refers to the neutral beam energy, T_e is the electron temperature. In order to match the NBI performances required in the three additional parameters are requested: P_{NBI} which characterizes the power associated to the injected beam, n_e the electron density and R_0 the major radius of the machine.
For a plasma temperature of 10-20 keV, like in ITER, it is foreseen a driven current efficiency of 3-4·10^{19} A/m² per injected Watt. Considering the sum of the two NBI power (i.e. 32 MW), the major radius of the machine (6.2 m) and the electron density (1020 m^{-3}) proper of ITER reactor it is possible to obtain overall an additional current drive realized in that machine in the order of 1.5-2 MA.

2.7 The D-beam energy design options

In order to assess the possible D-beam design options it is at first necessary to evaluate the dependence of the current drive from the energy of the beam. Such characteristic is shown in the Fig. 2.13 and parameterized for different value of plasma temperature.

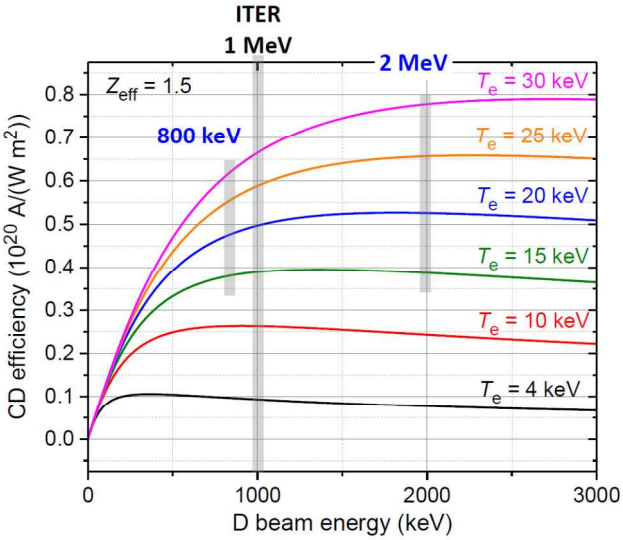

Figure 2.13 – Current drive efficiency performed for different plasma temperature and neutral beam energy.

If plasma operations were carried at a temperature of 25 keV, the gain obtained in terms of current drive efficiency in increasing the beam energy from 1 to 2 MeV, would be even lower (5%). On the contrary a 20% cut in the beam energy (800 keV) would produce a loss in term of current drive efficiency limited only to 7% passing from 5.9 to 5.5 A/Wm². Passing from 1 MeV to 800 keV design the losses associated to 20 keV operations would be even more contained (in the order of 3-4%).
Nowadays in the fusion community there is an open discussion if increase the energy of the ion beam from 1 to 2 MeV could be a reasonable option. Since the realization of 1 MeV energy neutral beam injector is presently a technological challenge, going up to a 2 MeV beam could involve a harsh complication of the project which would not be balance by an adequate gain in terms of current drive efficiency (cf. Figure 2.13)

Besides, as far as shinethrough is concerned, the proposal of having a 2 MeV injector is even more critical. Increasing the beam energy the penetration distance inside plasma would reach such a high value that the neutral beam injector could run only within a small operational window (i.e. at very high density). If the density is below such prescribed interval the fraction of shinethrough would be too high with the consequent risk of seriously compromising or destroying the first wall.
As already mentioned the NBI provides the transition from L to H mode during the transient phase in the start-up of the plasma. During this operation the plasma density is not the nominal one associated to stationary conditions, but lower. As a consequence higher risk of shinethrough is associated in case of high energetic beams. Therefore if the NBI device has to be sufficiently efficient for both the transition from L to H mode during the startup and to provide a sufficient current drive during the flat-top phase the 2 MV beam option could reveal several drawbacks.
On the contrary a less energetic injector (e.g. 800 keV) could operate in a wider spectrum (being more addressable with lower energy), with an associated loss in terms of current drive efficiency that is not so relevant. Due to the decreased risk associated with shinethrough, even in case of some accidental scenario during the H-mode phases the energy would sufficiently low to be absorbed inside the plasma.

2.8 Pros and Cons in adopting the NBI technology

Around 2009 a number of analyses have been performed with the aim of individuating the best configuration for ITER heating systems. In the publication the comparison between the use of NB, EC or IC or a given mixture of the three was shown. All the results of the simulations demonstrated that the neutral beam injector reveals to be more efficient for all the features that an additional heating is required to provide (i.e. current drive, plasma torque injection, fueling). In the specific it can be noted that for ITER the more NBIs were designed in the heating system mix the higher efficiency, with respect to these three features, was realized.

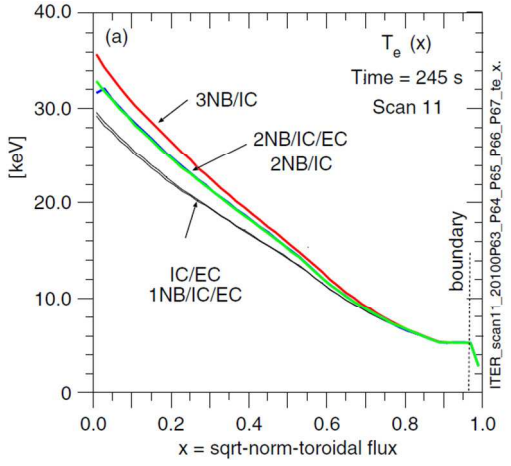

Figure 2.14 - Electron temperature distributions .along the radial direction for different heating system mix.

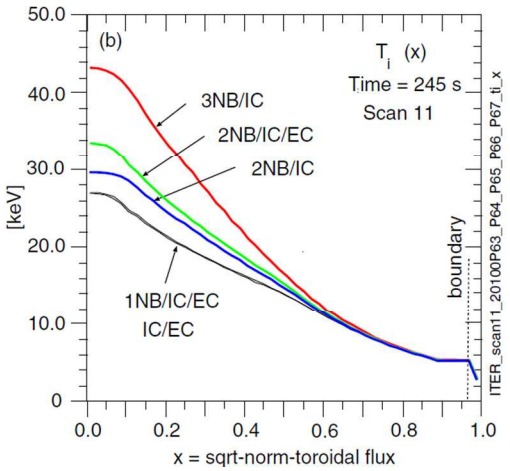

Figure 2.15 - Ion temperature distributions along the radial direction for different heating system mix.

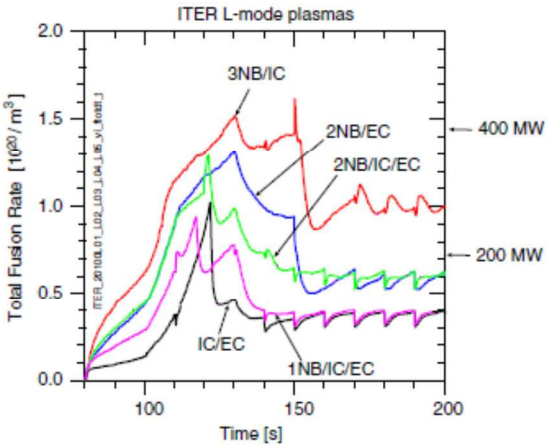

Figure 2.16 - Total fusion reaction rate in L-mode for different heating system mix.

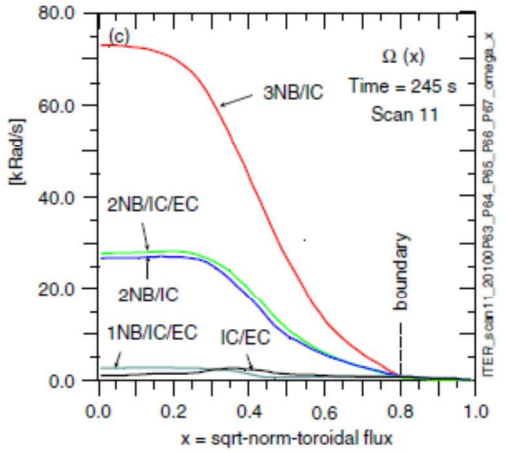

Figure 2.17 - Plasma Rotation distributions along the radial direction for different heating system mix.

The adoption of the neutral beam technology presents however a list of disadvantage:

c) The NBI requires a large scale of equipment and auxiliary plants (c.f. ITER);
d) The high voltage technology reliability in reactor relevant conditions is not fully demonstrated;
e) The negative ion current production efficiency is still not matching the injection requirements;
f) In the present system designed for ITER the overall NBI efficiency (calculated as power injected into the plasma with respect to the overall power given to the system) is very low and close to 25%, and having such inefficient sub-system is not acceptable for a future commercial reactor.

There are of course even advantages which make the adoption of NB indispensable:

g) It is possible to develop a system completely independent from the Tokamak itself (to be realized in a different facility);
h) The heating profile can be predicted independently from the magnetic configuration and this is an advantage with respect to the radiofrequency heating whose operating frequency must consider the magnetic field inside the machine in order to match the ion and electron cyclotron frequency;
i) There are no coupling issues, as for ion cyclotron where it is required to match the travelling wave between the antenna and the plasma through the injection of some gas;
j) Absence or limited reflection of power leading to a sufficient absorption;
k) High current drive efficiency in NB.

2.9 NBI components

The NBI devices are constituted by different sub-systems located serially one after the other which can be studied from the point of view of the related components. Starting from the generation of particles the final injection into the plasma the following systems can be identified:

a) the ion source, where H^- or D^- ions are produced through arc of RF drivers acceleration stages by means of electrostatic grids;
b) the extractor, where the ions in the plasma are extracted by means of an electric potential, forming an ion beam;
c) the accelerator, where the ion beam is accelerated to the designed potential;
d) the neutralizer, that transform the ion beam into a fast neutral one;
e) the deflection system removing from the beam the particles that have not been neutralized in the previous section leading them to be absorbed on the residual ion dump;
f) a calorimeter, used to measure the power of the beam together with its spatial distribution in order to test the efficiency of the NB before injecting it into the plasma;
g) a connection duct with the Tokamak for the final injection of the neutral particles inside the plasma.

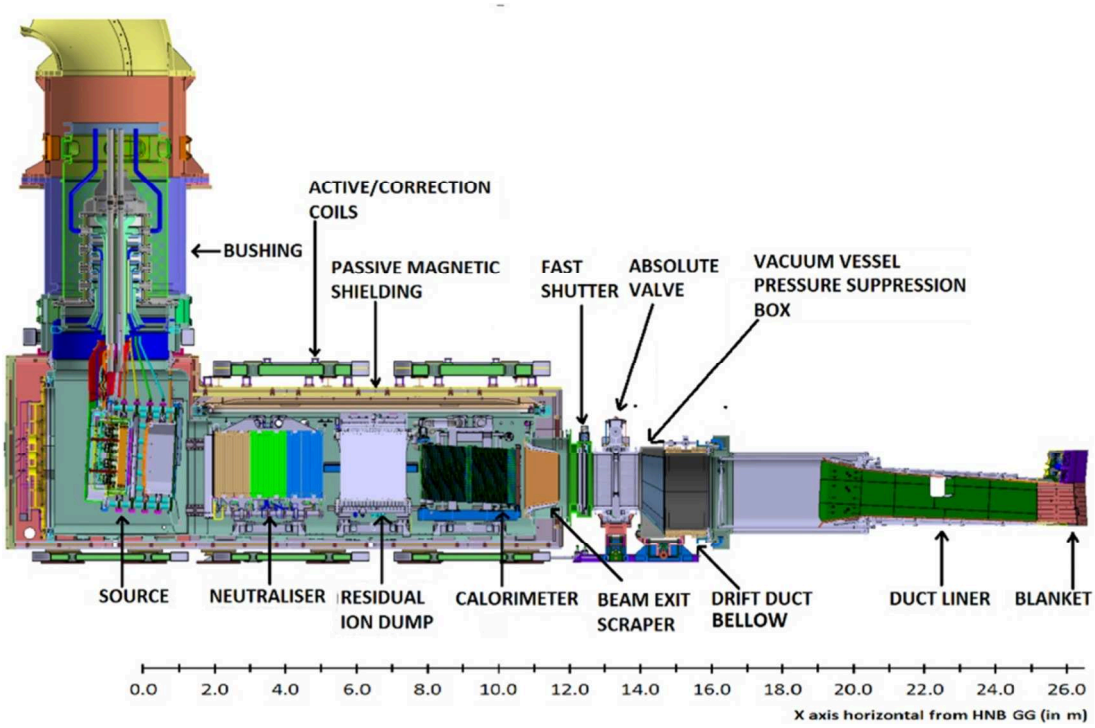

Figure 2.18 - Rendering representation of ITER beam-line injector.

During the past years, the basic concept of the beam system has been further refined and developed, and assessment of suitable fabrication techniques has begun [12].

2.9.1 Ion Source and Negative Ion Extraction

The production of a neutral beam is performed starting from the generation of energetic ions in a source facing an expansion region where the hot plasma is confined. Basing on the concept employed in order to produce the electrons, forerunner of the plasma, the generation system can be classified in two different categories:

- *Arc Sources*

  In an arc source electrons are emitted from a hot cathode and accelerated by a DC voltage of typically 100 V into the source. The subsequent ionization of the gas molecules leads to the desired plasma. Numerous configurations, differing in the way of optimizing the ionization efficiency of the fast electrons (for example by utilizing magnetic fields, biasing the source walls etc.) have evolved over the last 25 years. The development of these sources is based mostly on empirical methods, while theoretical work is exploited in order to address singular topics like ionization efficiency and composition of atomic and molecular species.

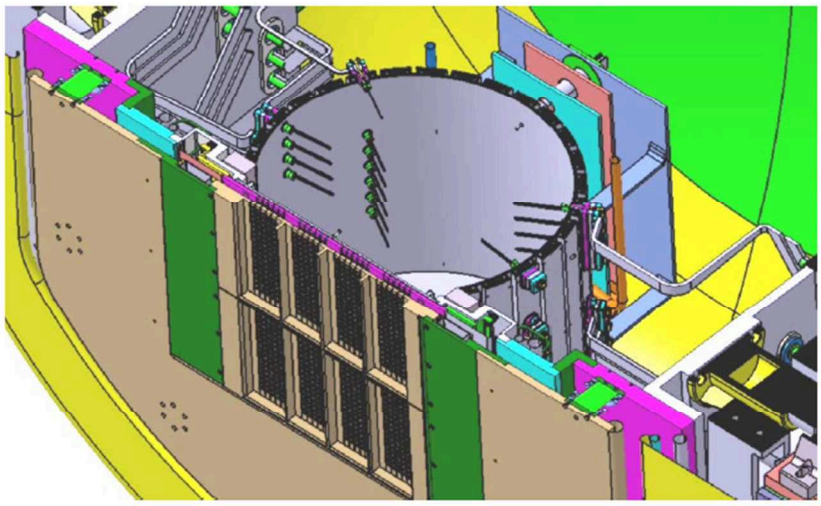

Figure 2.19 - Arc driven source overview.

- *Radio Frequency Sources*

  In order to accelerate electrons which eventually produce the desired plasma the radio frequency source exploits an oscillating electric field, generally induced by a radio frequency coil. A typical frequency for RF sources is 1 MHz, while requiring a power supply in the order of 100 kW.
  Radio Frequency sources have a number of advantages with respect to the arc sources: a longer lifetime due to the absence of filaments having a limited thermal cycle time, a better control of the extracted current due to the direct response of the ion density in the source to changes of the RF input power, the

simplicity of the source (less electrical connections compared to arc source), making remote handling easier.

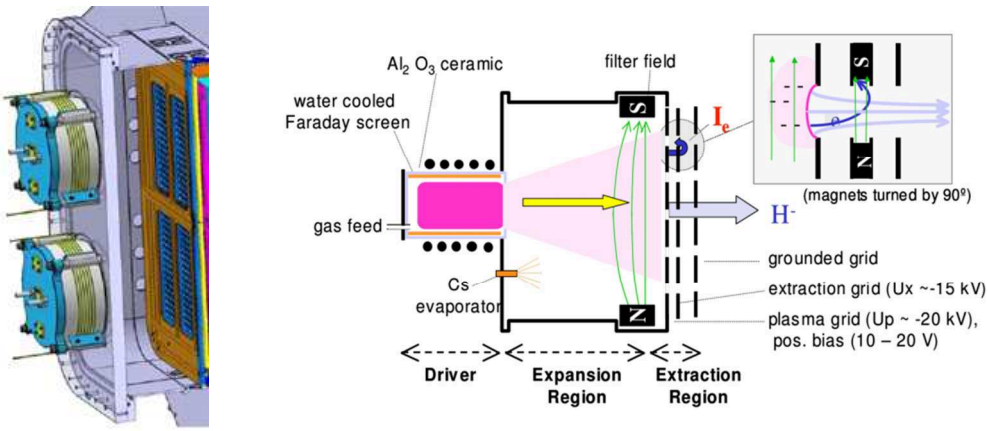

Figure 2.20 - Radio Frequency ion source overview (left) and schematic representation of the overall system (right).

Once the plasma is created the particles have to experience physical phenomena which eventually lead to the production of negative ions to further accelerate into the injector. There are essentially three different mechanisms able to generate the required negative ion population:

a) Double charge exchange:

The double charge exchange mechanism requires a cell in which is present an alkali metal vapor in which in case of injection of a positive ion it is possible to extract a negative one due to low work function of alkali metals. This mechanism however is not the one exploited in the present sources.

b) Volume Production:

This ions production process occurs in the volume of the source through roto-vibrational mechanisms which involve a neutral molecule of hydrogen (or deuterium) and a low energy electron. The subsequent interaction can produce a dissociative attachment leading to the creation of one negative ion and one neutral atom of the reactant specie.

$$H_2 + e(\leq 1eV) \rightarrow H^- + H \tag{2.19}$$

c) Surface Production :

The main mechanism employed in the sources is the surface production. In this process the radicals of Hydrogen or Deuterium interact with the surface of the source which has been previously coated with cesium (Cs). Due to the alkali electronic configuration Cs has one of the lowest work function for electron retention. Such characteristic increases the probability that sputtered particles could escape in the form of negative ions having captured one e^- during the interaction with the Cs-coated wall. The adoption of Cs leads to a 3÷5 factor

increase of the negative ion yield production, a decreasing operating pressure, a drop down of stray electron current ratio and linear dependent production of negative ions in Cs seeded ion sources with increasing arc or RF power, with no yet revealed saturation phenomena

$$H_x^+ + e_{surface} \rightarrow H^- \tag{2.20}$$

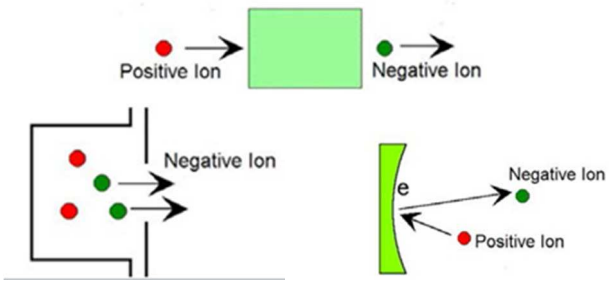

Figure 2.21 - Schematic representation of the three different mechanisms governing the ion production phenomena.

Once the negative ion is produced there are however three volume destruction processes:

1. Mutual neutralization process:

This is the most important destruction process where collisions between a positive ion and the opposite negative one may lead to the removal of the excess of electrons from the negative ion population.

$$H^- + H^+(H_2^+, H_3^+) \rightarrow H + e + \ldots \tag{2.21}$$

2. Associative detachment process:

Such process consists in the collision between the negative ion and neutral atom of the specie which eventually produce a neutral molecule and a free electron. This reaction is however is less effective than the previous ones.

$$H^- + H \rightarrow H_2 + e \tag{2.22}$$

3. Electron detachment process:

In such process the collisions with high energy electrons produce the electron detachment of the negative ion. This counter-acting detachment process rate can be limited through the introduction of a transverse magnetic field in the region immediately close to the plasma grid. Such field produces a physical separation between the hot plasma production region (characterized by electrons with an energy of tens of eV) from the negative ion production one (pre-sheath and sheath region).

In such way positive and negative ions and cold electrons (with an energy lower than 1eV) can penetrate this region, while those with higher energy are confined through the magnetic field and hence prevented from the region in which negative ions are extracted. The ion source so created is denoted as tandem or magnetically filtered ion source.

Due to these ion destruction processes the related life time of the produced particles is very short it is necessary to remove the negative ions as close as possible to the site where they are generated.
Such issue is solved placing immediately after the plasma grid (PG) confining the pre-sheath and sheath region, the extraction grid (EG). The applied voltage difference between these grids is able to create an electrostatic field producing an electrostatic lens in correspondence of the openings in the PG. The particle is then attracted and converging in the direction paved by the lens. The further differential voltages between EG and the other accelerating grids (AGs) perform the acceleration of the beam to the final designed energy.
An additional issue which need to be addressed during the extraction stage is given by the fact that the negative charged current extracted from the source might be composed by both electrons and negative ions. The power supply cannot indeed distinguish between these two populations characterized by the same electrical charge.
Since the overall charge that can be collected a fix parameter, the more electrons are extracted the fewer ions can be collected leading the amount of negative ions accelerated to decreases together with the power that is eventually injected into the plasma.
The electrons that are however collected and extracted from the source need to be managed and to a large extent removed during their acceleration with negative ions. If this is not the case at the end of the acceleration stage the beamlet designed for the additional heating of plasma would turn into an electron beam system.
At that energy a similar device would not transfer any momentum but would just cut or weld any material that lies on the trajectory of the electrons whose paths in addition cannot be properly controlled but are disseminated all around the system.
This is the reason why NBI device are characterized by precise limitation on the amount of co-extracted electrons (in ITER the ratio e^-/H^- should be lower than 1).
The removal of such electronic population is realized through the introduction of a further magnetic field by means of permanent magnet installed in the extraction grid.
Such magnetic field interacts by means of Lorentz's law with the extracted particles producing a deflection, which in case of the electrons leads to their disposal on the Extraction Grid.

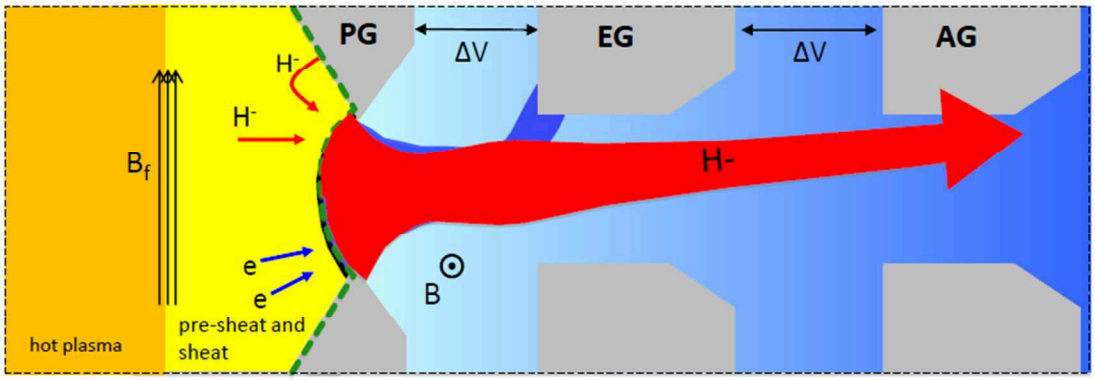

Figure 2.22 - Representation of the extraction mechanism of ions and electrong in the beam source.

2.9.2 Acceleration stages

During the acceleration stage the negative ion beam produced in the source has to be accelerated to the nominal energy of the injector limiting to the maximum extent the losses resulting from unavoidable parasitic processes which mostly involve the destruction of the negative ions. The main phenomena which are responsible for the losses in the accelerating region are:

- Stripping losses;
- Secondary electron produced, disposed and transmitted;
- Back-streaming of positive ion accelerated toward the plasma source;
- Halo fraction.

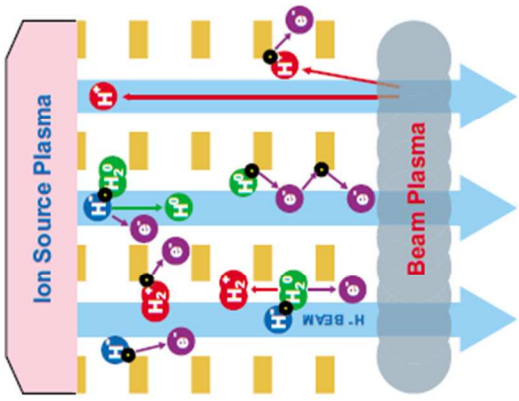

Figure 2.23 - Schematic representation of parasitic losses along the acceleration stage.

The stripping reactions involve the loss of the additional electron in negative deuterium atoms on background gas resulting in the stripped electron and an unconfined neutral deuterium atom. This neutral population will travel without suffering any accelerating drift and will not eventually contribute to the heating of the plasma.

Electrons can be additionally created through ionization of background gas by deuterium atoms and by interactions of stray ions, neutrals and electrons with surfaces in the accelerator. Such secondary electron population is to a large extent eventually deposited on the electrostatic grids through the presence of tailored magnetic fields. In such a way the electron power at the exit of the accelerator is strongly decreased.

The third process is referring to those collisions leading to the production of positive ions which due to their opposite charge are back accelerated towards the plasma source. This flux of positive ions that are back accelerated needs of course to be taken into account in the design of the device.
The halo fraction of negative ions is a portion of negative particles that are extracted from the source but are not properly optically confined inside the main beamlets. The name halo derives from the fact that it is still not very well exactly understood where these particles are originated. Such contribution mainly results from experimental activities and it is not very easy to reproduce with the codes starting from particles that are extracted directly from the plasma. Being its evaluation very difficult, a percentage of current due to these negative ions is usually superimposed to those numerically evaluated.
As a matter of fact parasitic processes can also involve the successive generation of particles coming out from one of the four losses mechanisms. The neutral particles (H_2 or D_2) generated by the stripping processes could indeed be involved in collisional events with other negative ions which eventually give origin to the presence of an additional neutral hydrogen plus one electron stripped by the ion through the associative detachment process.
In addition to the losses addressed by the previous processes it is essential to take into account the contribution derived electrostatic issues and affecting the optics [13]. The charges that are accelerated are subjected in fact to the phenomena of space charge repulsion, resulting from the fact that the population of particles is all characterized by the same charged and only the central beamlet can indeed overcome such issue due to the symmetric electrostatic conditions.
As a matter of fact the beamlets start to diverge from the nominal cylindrical shape inside the grid openings along the beam line direction. Superimposed to this effect is acting the halo contribution of additional negative ions which are not very well either confined or described into the main beamlet. The primary Gaussian distribution around the axis is then accompanied by a second broader one which carries around the 10-15% of the amount of the primary Gaussian current but with a larger dispersion which describes the halo fraction contribution.
The beamlet trajectory and shape can be therefore described by a theoretical beam axis and a deflection angle with respect to the nominal mechanical one which takes into account magnetic and electrostatic aspects. The direct consequence of this phenomenon is that the different beamlets can eventually have direct intersection with the wall of the grids or other boundary.

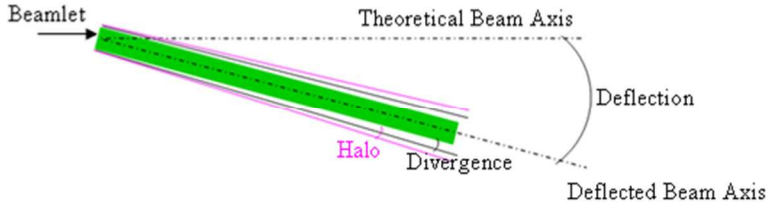

Figure 2.24 – Representation of the deflection produced by magnetic fields, divergence and optical mechanism involving a ion beamlets.

One of the possibilities to recover this misalignment of the beamlets is to introduce some different additional electrostatic conditions which could eventually readjust the space charge effect in multi beamlet system. The solution is given by placing copper plates, called kerbs, with a defined thickness and position with respect to the original deflecting angle.

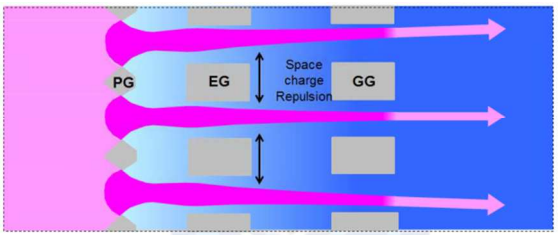

Figure 2.25 - Representation of the space charge repulsion effect.

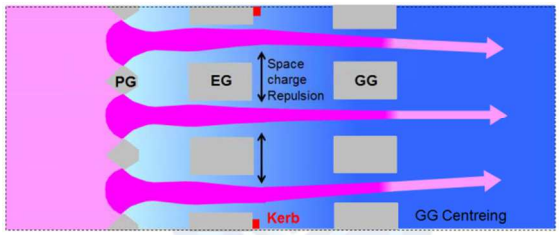

Figure 2.26 - Representation of the resulting effect after the introduction of kerbs.

The boundary conditions for the definition of all the phenomena that occur in the acceleration stage are mainly given by the limit of the system due to the following aspects:

a) the presence of neutral particles;
b) the voltage holding;
c) the electrostatic local deflection;
d) the magneto-static local or global deflection.

As already mentioned in the description of the volume process ion production, when the negative ions are extracted from the plasma grid the electrostatic lens given by the topology of the electric field, called meniscus, cannot distinguish the ion from the electron population and collects the both of them. It is hence necessary to add a magnetic field, through permanent magnet inserted in the extraction grid, which could deflect the electrons population (whose Larmour radius is smaller) with a large angle. However a small deflection is even associated to the main negative ion beamlet and it is therefore necessary to correct such deflection, or in case of a multiple stage acceleration the fraction of particles that intercept the physical wall would reach unbearable values.

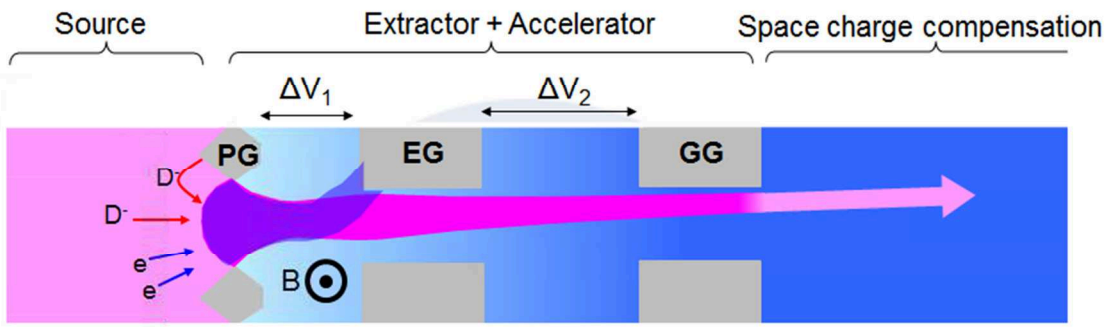

Figure 2.27 - Negative ion residual deflection due to the presence of the magnetic field producing the removal of co-extracted electron population.

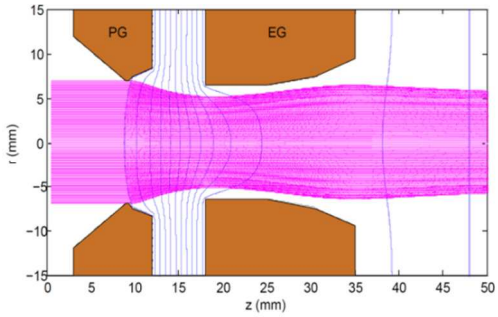

Figure 2.28 - Effect of the electrostatic lenses resulting from the electric filed comprised between two successive grids.

At a given perveance of the system given by the expression (2.23) with S expressing the aspect ratio parameter given by the ratio between the radius of the grid holes at the plasma grid and distance between the plasma grid and the extraction one, it is possible to regulate the voltage difference between the plasma and extraction grids obtaining different configuration of beamlet divergence.

$$P = \frac{4}{9}\pi\varepsilon_0\sqrt{\frac{2eZ_{ion}}{m_{ion}}}S^2 \qquad (2..23)$$

In case of a too low voltage difference between the plasma and the extraction grid the beamlet is not very well confined and will be characterized by high divergence (with the trajectory of the particles looks like the one described in Figure 2.28-a). On the other hand if the extraction imposed by the voltage difference is too high the beamlet is characterized by a too high degree of convergence, and therefore after the interception of the external boundaries of the extracted particles the beamlet starts to diverge again (cf. Figure 2.28-c).
Between these due opposite configuration there is a condition of minimum of divergence for which the extract ions composing the beamlet are characterized by the best optical configuration (cf. Figure 2.28-b). As a matter of fact, the injector has to operate close to these conditions.

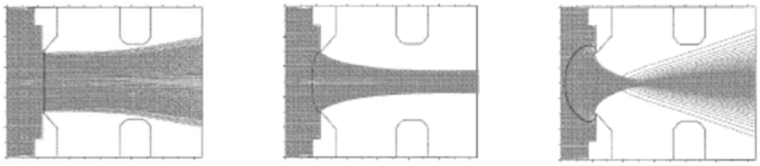

Figure 2.29 – Beamlet divergence resulting from a too low (left), a proper (center) and a too high voltage difference applied between extraction and plasma grid.

Although such consideration is valid for the extraction stage, the control of the divergence has to be performed in all the different acceleration stages, since every successive grid is characterized by two electrostatic lenses, one at the entrance producing a divergence of the beam and one at the exit with an opposite curvature which allows for the re-concentration of the beam. The voltage and the position of the different accelerating grids should therefore be optimized in order to have a minimum divergence at the exit of the acceleration stage (i.e. downstream the grounded grid).

Taking into account all these contributions a detailed set of beam optics and physics analyses have been carried out with the geometry and magnetic field configuration design for MITICA. The simulation has been carried out with a purposed code (EAMCC) and considering a much large number of particles, in order to provide a quite affordable estimation of the power density deposited on the grids and the one transmitted downstream the acceleration step [14].

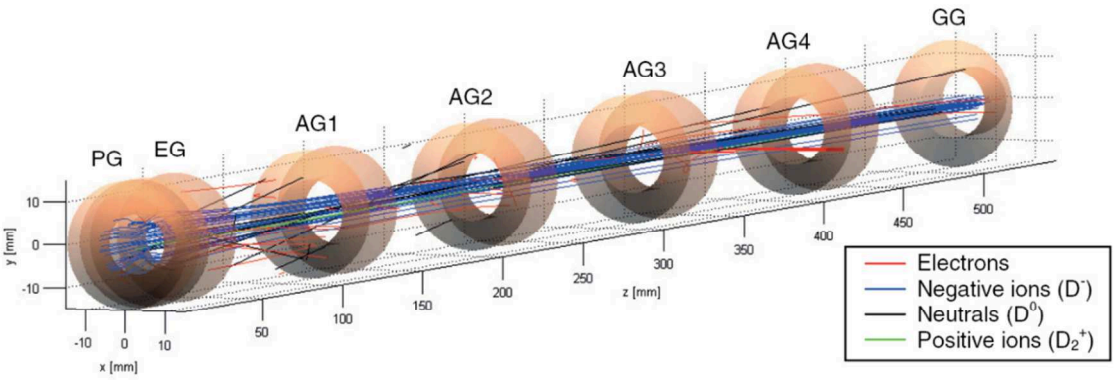

Figure 2.30 - EAMCC simulated co-extracted electrons, negative and positive ions and neutrals trajectories along the different accelerating grids.

The results obtained from EAMCC code have been successively employed in order to evaluate the overall heat loads and the spatial distribution of the specific heat fluxes insisting over the various up-streaming plates of the different electrostatic grids. The spatial distribution of heat loads insisting on the cylindrical surfaces of the beamlet openings and on the back-plate surface s of the different electrostatic grids can be instead neglected and considered uniform.

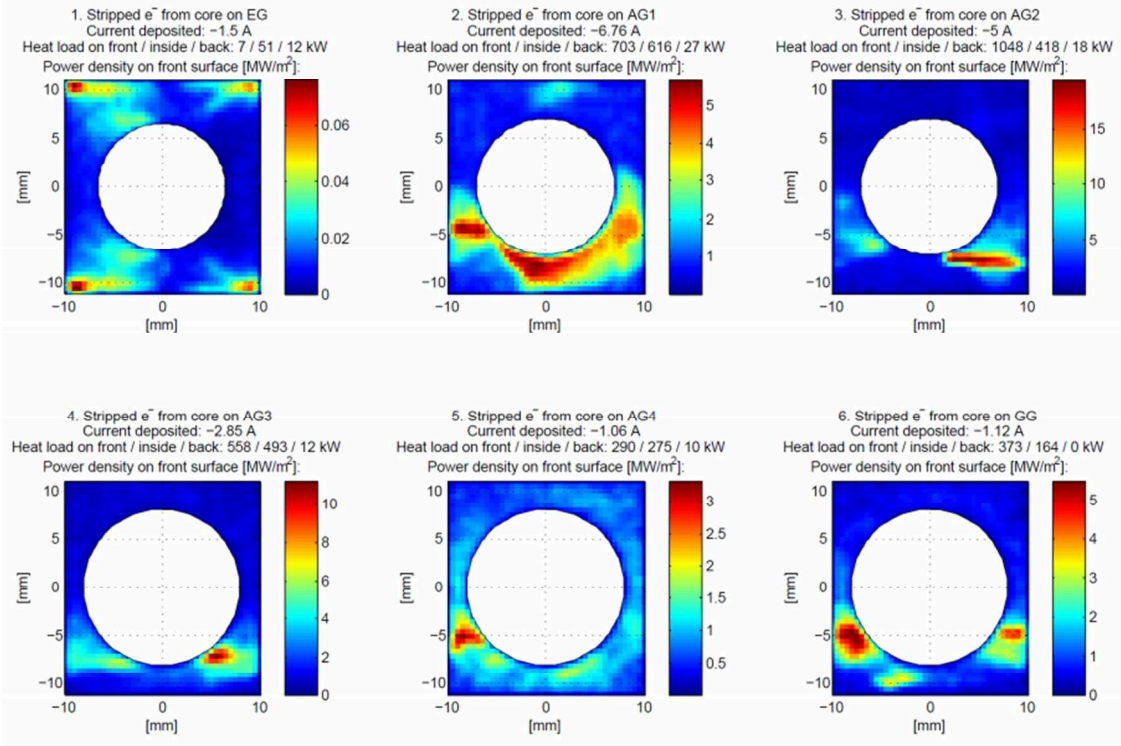

Figure 2.31 - Stripped electrons heat loads distribution on the different electrostatic grids of MITICA calculated with EAMCC according designed geometry and magnetic configuration.

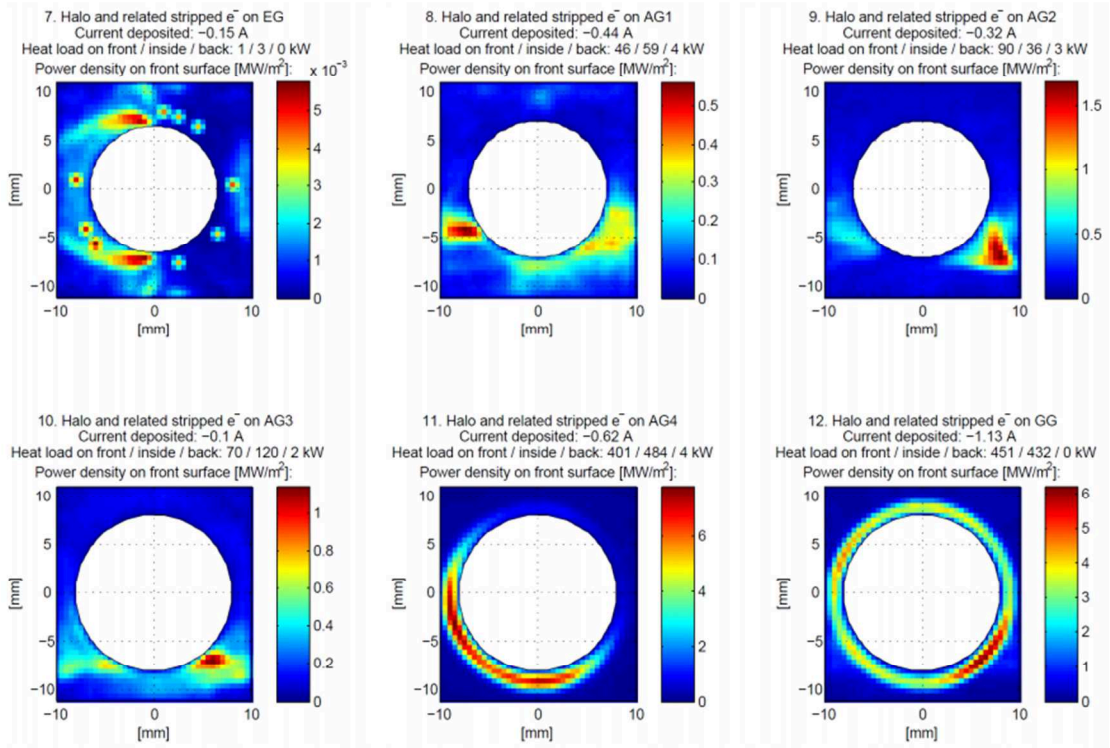

Figure 2.32 – Halo fraction and related stripped electrons heat loads distribution on the different electrostatic grids of MITICA calculated with EAMCC according designed geometry and magnetic configuration.

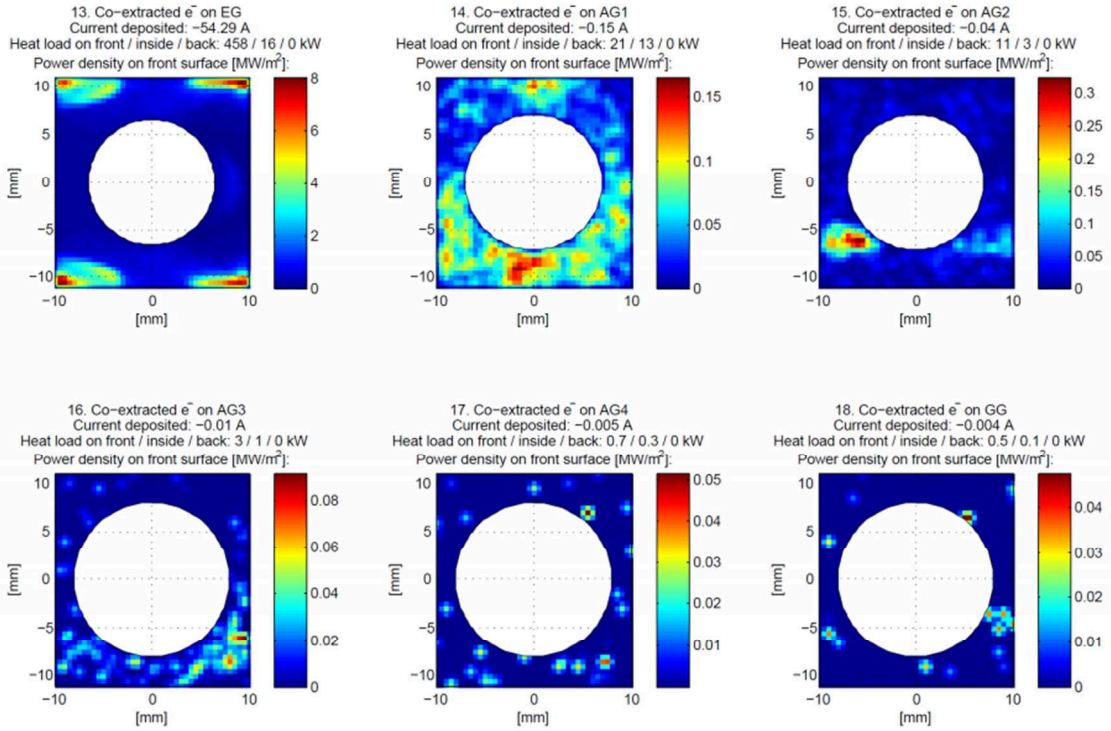

Figure 2.33 – Co-extracted electrons heat loads distribution on the different electrostatic grids of MITICA calculated with EAMCC according designed geometry and magnetic configuration.

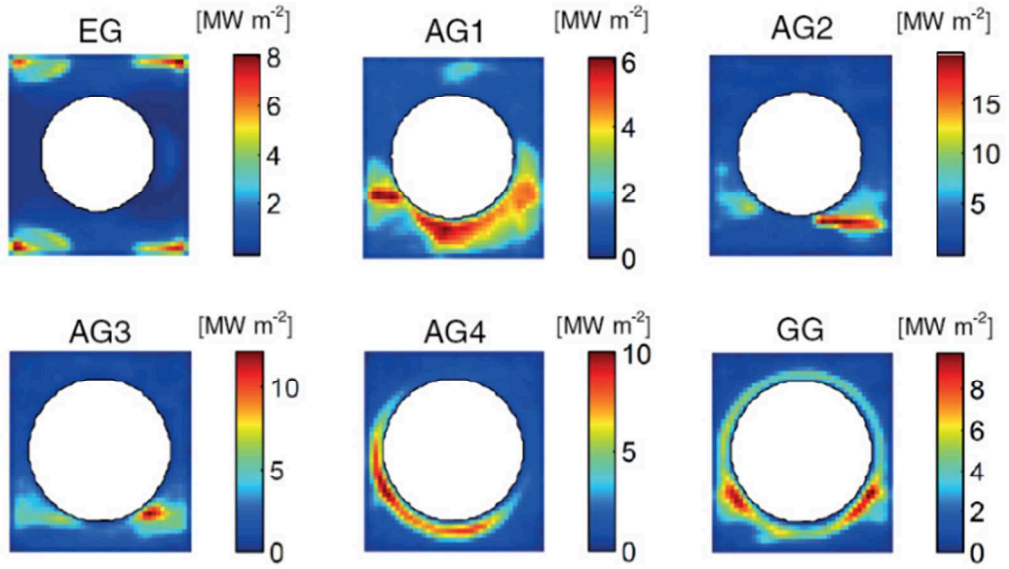

Figure 2.34 - Overall heat loads spatial distribution on the different electrostatic grids of MITICA calculated with EAMCC according designed geometry and magnetic configuration.

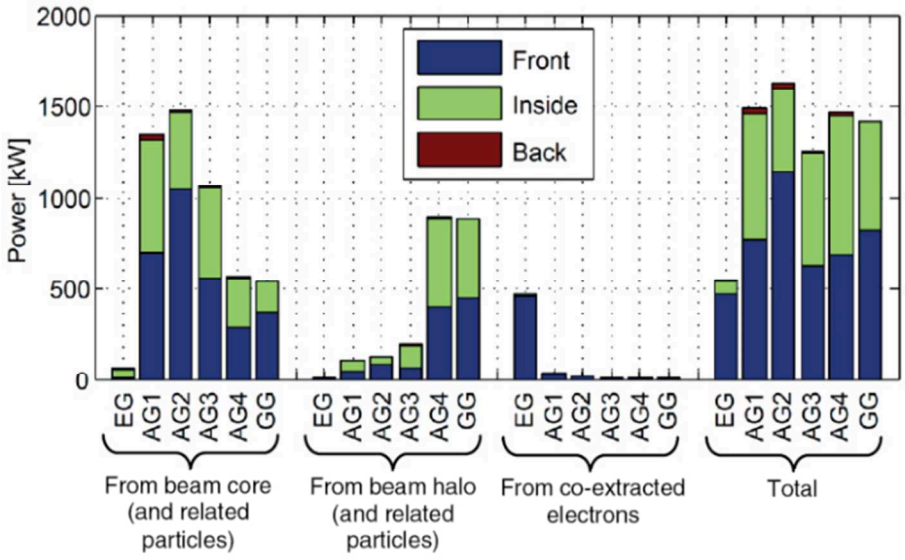

Figure 2.35 - Overall heat loads on electrostatic grids discriminated in terms of the depositing surfaces.

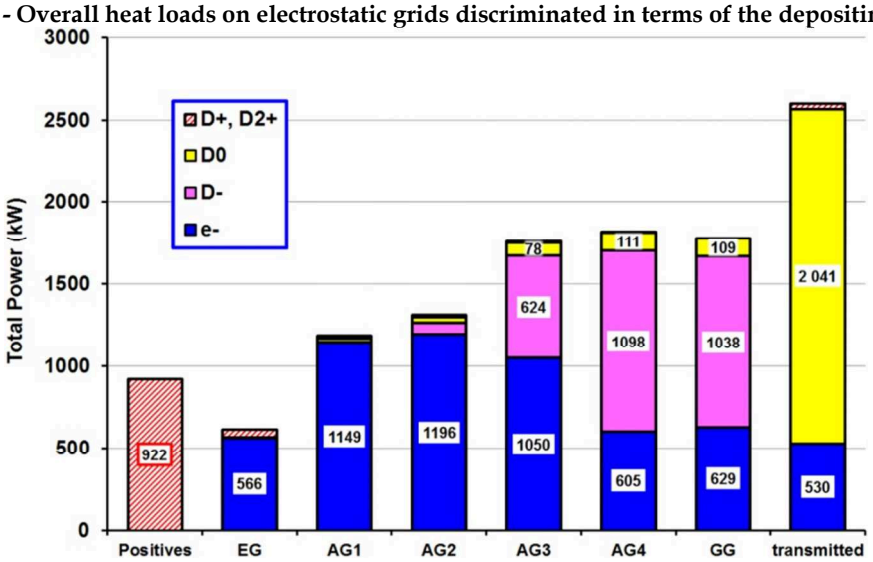

Figure 2.36 – Power loads on the EG, the accelerator grids, power from back-streaming positive ions and the power exiting from the accelerating stage (except D^-) as calculated by EAMCC under less conservative conditions.

2.9.3 Negative Ion Neutralizer and Electron Dump (NED)

Moving outside the accelerator stage, the neutral beam injector hosts the so called beam line components. Figure 2.35 depicts the footprint of one of the 1280 beamlet coming out from the beam source with a specific power of 2000 MW/m^2. Each beamlet is not exclusively composed by negative ions but a fraction of electrons and an even smaller extent of positive ions are present.

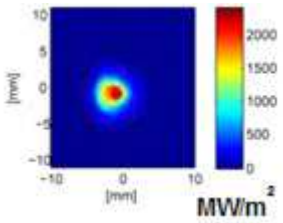

Figure 2.37 - Transmitted negative ion footprint coming out from grounded grid openings.

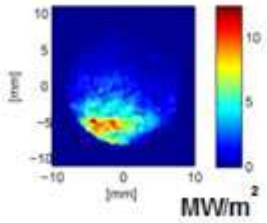

Figure 2.38 - Transmitted electron footprint coming out from grounded grid openings.

It can be noted that the uniform magnetic field deflects the load (mainly constituted by negative particles, electrons and ions) towards the lower part of the openings. This is the filter magnetic field used in the source to deflect the high energetic electrons.
Those electrons are able to exit from the accelerating stage unless properly managed they eventually go to impinging on the cryopump, leading to increase the requirements for the cooling of these devices in order to avoid loss of performance of the cryopump system. In order to avoid the cryoplant to be designed both for the heat radiation in vacuum and to withstand the additional heat loads related to the unconfined electrons, two louvre-like copper (Cu) panels are placed on each side of the neutralizer entrance and another electron dump panel is located below the neutralizer entrance.

.

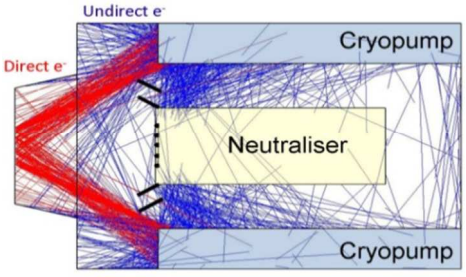

Figure 2.39 - Direct and indirect electron trajectories along the neutralizing stage (horizontal cut).

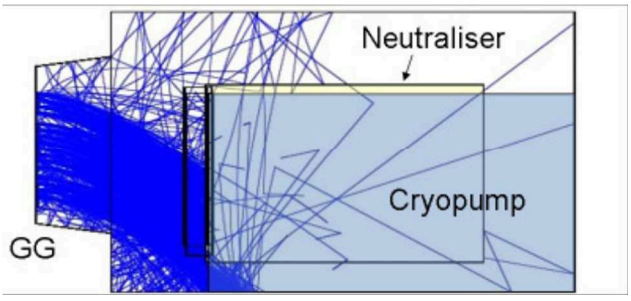

Figure 2.40 - Indirect electron trajectories along the neutralizing stage (lateral cut).

The beam line components consist of the neutralizer, the residual ion dump and the calorimeter. The cryopump are instead surrounding the overall neutral beam injector.
The neutralization process is done in a 10^{20} particle per cubic meter gas through the electron loss or electron capture mechanism respectively for negative and positive ions.

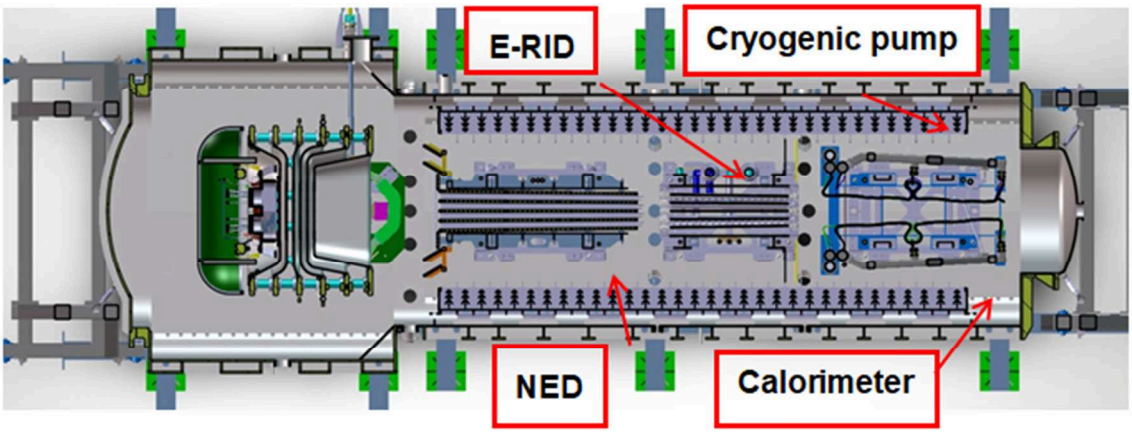

Figure 2.41 - Beamline components disposition along the neutral beam injector device. Downstream the neutralizer electron dump (NED), the Residual Ion Dump (E-RID) is located immediately followed by the calorimeter device. All the different components are surrounded by two sets of cryogenic pump batteries.

The almost constant neutralization efficiency in negative ion beam injector (cf. Figure 2.6) comes from two competing processes. In the neutralizer the incoming deuterium negative ions that interact with neutral gas generate a stripped electron, obtaining therefore one neutral deuterium atom and the stripped electron at the final acceleration energy, plus the neutral gas molecule remaining at room temperature.

The energetic D_0 can however further interact with another D_2 generating a positive ions at 1MeV. Due this process the creation of positive ions increases linearly with the increase of the target thickness of the neutralizer gas (given by the product of the length of the neutralizer times the density). It is worth noting that the same product between neutralizing stage length and gas density produce the same results in terms of production of positive ions and neutralization of negative ones.

$$D^- + D_2 \Rightarrow D^0 + D_2 + e \qquad D^0 + D_2 \Rightarrow D^+ + D_2 + e \tag{2.24}$$

Figure 2.43 depicts for a given gas target thickness crossing estimated production of positive ions and the portion of neutralized negative one. The two trends have monotonic behavior, increasing for positive ion production and decreasing for negative ion neutralization. As a matter of fact the composition of the two contributions produces the estimation of the overall neutralized particles coming out from this stage, which reaches a maximum.

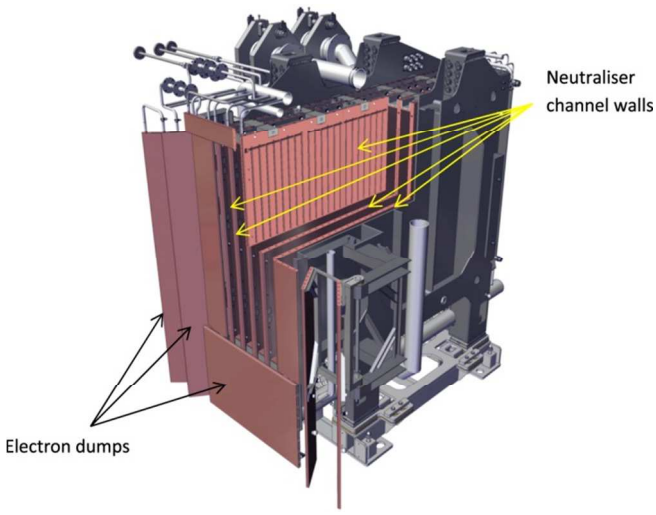

Figure 2.42 - 3-D rendering of the neutralizer and Electron Dump device.

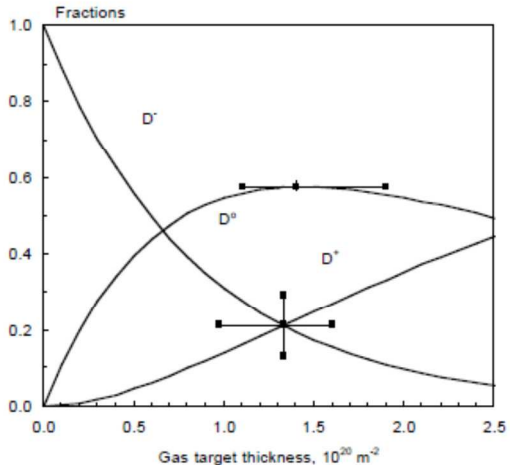

Figure 2.43 - Negative and positive ion fraction distribution over neutralizer gas target thickness.

At smaller gas target thickness it is not possible to neutralize a sufficient number of particles despite a low positive ions production, on the contrary with too high gas target thickness there is an excessive production of positive ions accompanied with a marginal small neutralization of negative ions.

The maximum neutralization efficiency is close to 60% regardless the incoming energy of the incoming ions. At the gas target thickness value associated to the maximum neutralization efficiency the incoming negative ions which have not experienced neutralization are around the 20%, another 20% have been converted into positive ones while the remaining 60% have turned into neutrals.

For Deuterium operation at 1 MeV, the gas target thickness associated to the maximum neutralization efficiency is in the order of $1.4\ 10^{10}\ m^{-2}$ while for H operation at 100 keV and 800 keV the maximum is respectively located at $0.4\ 10^{10}\ m^{-2}$ and $2.1\ 10^{10}\ m^{-2}$.

Around those values the composition of the particle population exiting from the neutralizer is the same (20% of both positive and negative ions, 60% of neutrals) regardless to the chosen combination of gas density and neutralizer length.

As far as the vacuum conductance is concerned it is worth noting that in the neutralizer the profile of the gas is not flat. It is indeed worth noting that the pressure outside the neutralizer should reach through a set of cryogenic pumps very low values (around 0.02 Pa) in order to limit the stripping phenomena outside the neutralizer itself.

Considering this component as a prism with a rectangular base and a length of approximatively 3 m, it is possible to evaluate that the nominal density (close to $1.0\ 10^{20}\ m^{-3}$) is performed only in about 1 m. In order to guarantee the expected value of density along the central section, the throughput of gas from the overall 20 injection holes shall reach values in the order of 43 Pa m^3s^{-1} for Hydrogen operation at 616 Pa and 19 Pa m^3s^{-1} for Deuterium operation at 272 Pa. Such levels of throughputs are much high and comparable to the one associated to a radiating configuration of the divertor.

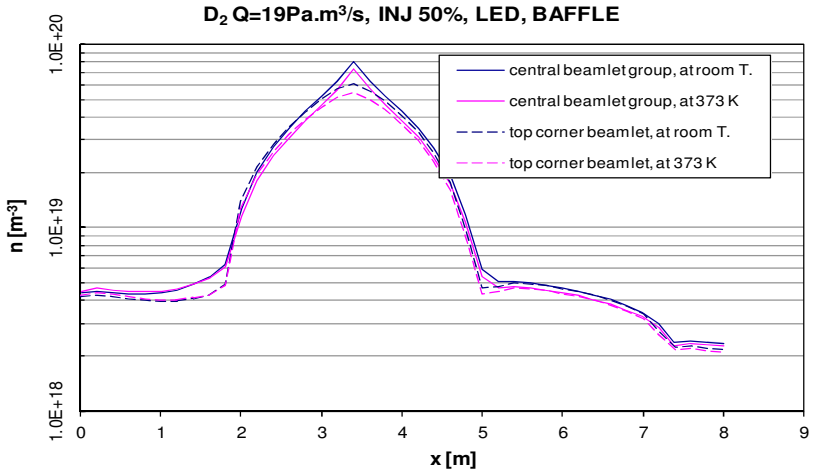

Figure 2.44 – Gas density distribution along beam line components axis encountered by central and top corner beamlet group (neutralizer device is comprised between 2 and 5 m).

2.9.4 Residual Ion Dump

As mentioned in section the previous paragraph, the beam emerging from the neutralizer will consist of about 60% D^0 and 20% each of D^- and D^+ (the residual ions). The residual ions, must be removed from the beam in a controlled way inside the injector to avoid their deflection into the walls of the duct between the injector and the reactor chamber by the stray magnetic field, as that would lead to an unacceptable power load to the walls of the duct and an unacceptable level of reionization of the NB.
The residual ion dump can be classified in two different categories: electrostatic and magnetic ones. The magnetic RID are more robust in reason of the longer operation experience, but they are accompanied by dimensional problems. The dimension of the magnetic core that is necessary to create a magnetic field able to deflect the positive and negative ions and the resulting electrons is quite demanding in term of volume. As a matter of fact due to the operational condition foreseen in ITER it has been decided to develop an electrostatic residual ion dump.
The RID consists of 5 panels forming 4 vertical channels in line with the walls of the neutralizer channels. A potential difference is applied to the 2nd and 4th panels in order to deflect the ions entering the channels to the left or to the right depending on their charge.
Each RID panel is made of 18 CuCrZr elements, with 4 cooling channels inside each element. Twisted tapes (70 mm twist pitch) inside the cooling channels act as a turbulence promoter and subcooled nucleate boiling can occur. The flow rate division amongst the elements of the panels is to be realized by varying the thicknesses of the twisted tapes in the cooling channels, with larger flow rates through the more heated elements.

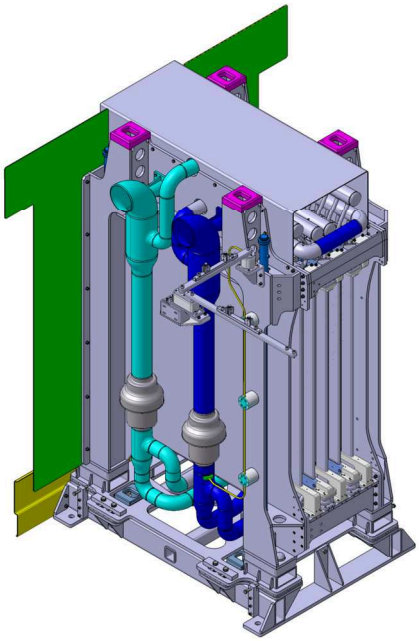

Figure 2.45 - Electrostatic residual ion dump rendering.

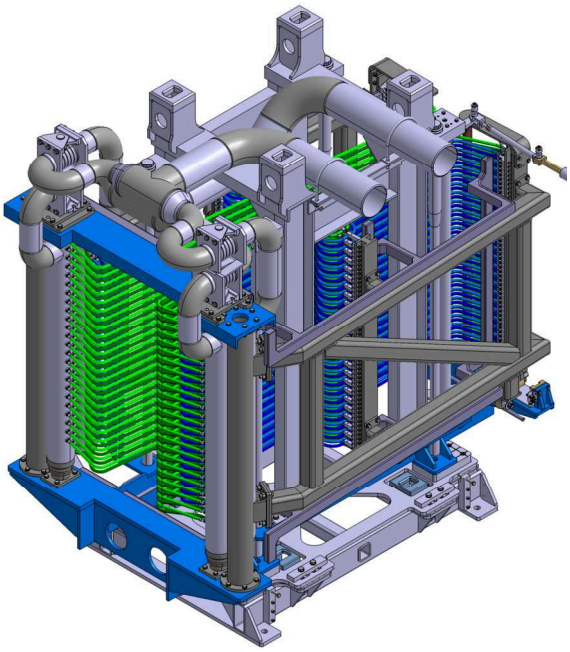

Figure 2.46 - Calorimeter assembly rendering.

2.9.5 Beamline Calorimeter

The beamline calorimeter is located downstream of the RID. It consists of 2 panels arranged either in a V shape, such that the panels intercept the beam, or the panels can be rotated so that they sit either side of the beam, leaving a clear passage for the beam to continue towards the vacuum vessel.

When the calorimeter intercepts the beam, the HNB can be operated independently of the operation of the main machine, which allows the commissioning, or re-commissioning, of the HNB.

Each calorimeter panel is made up of a double array of CuCrZr swirl tubes placed one behind the other; the rear array covers the gaps between the STs of the front array. The swirl tubes intercept the beam at an angle (of about 6°) with respect to the beam axis. At the location of the calorimeter, the peak heat flux in the beam is 130 MW m^{-2}, with a beamlet divergence of 3 mrad, no halo, but with the beam power reduced so that only 16.5 MW is eventually injected into the reactor chamber.

The inclination of the panels with respect to the beam axis reduces the heat flux on the tubes to a peak of ≈13 MW m^{-2}.

The 2 panels are each made from 96 tubes, 20 mm in diameter, arranged parallel to the beam in 2 arrays so as to overlap vertically by 4 mm, thus effectively forming a panel that is opaque to the beam particles.

Notwithstanding some beam particles can be scattered from the tubes and pass through the gaps between them, hence thin sheet steel panels are mounted behind the tubes to intercept these.

2.9.6 NB Duct

Following the particle trajectory at the exit of the beam line components, the last stage to be performed is the injection into the plasma. The particles enter in a duct, a rectangular or circular tube which is not pumped at the walls. As a matter of fact the duct can be pumped only from the injector or from the Tokamak.
Depending on the operation of the neutral particles inside the Tokamak (e.g. Argon injection to cool down the edge of the plasma) the final pressure in the plasma and inside the duct can raise of one order of magnitude with respect to the pressure that realized into the vacuum region of the injector.
The length of the duct is about 15 m, a relevant fraction of the all NBI system length (20-25 meters, duct included). Along such distance the beam is interacting with neutral gas leading therefore to additional reactions of stripping and re-ionization of the beam, with consequent heat loads on duct wall.

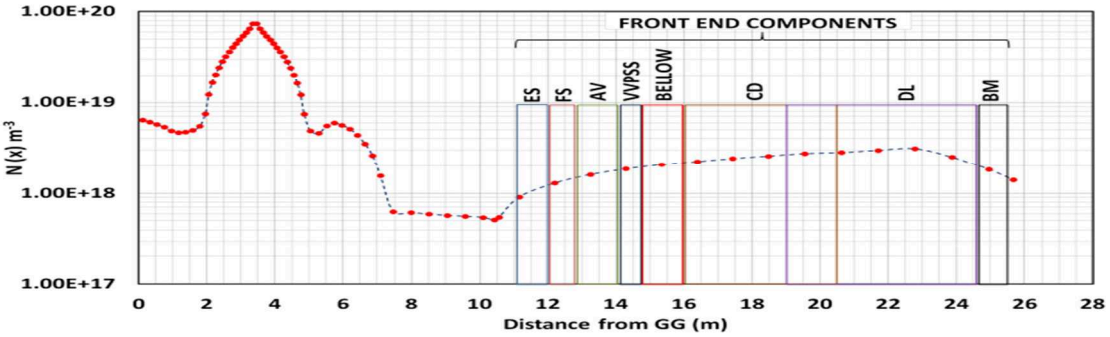

Figure 2.47 - Estimated neutral particles density along the beam line components and the final injection duct.

3

3. Development of high performance cooling systems for fusion device

Current Neutral Beam Injectors (NBIs) are designed to accelerate deuterium negative ions with energy up to 1 MeV and current up to 40A. The NBI Beam Source represents one of the most critical parts of the Neutral Beam Injectors since its performance largely influence the efficiency of the whole injector.
Crucial components inside the injector Beam Source are the accelerating grids which have to be designed to operate at high voltages and to withstand high power density loads. In addition they are required to guarantee an optimal performance in terms of optics in all the foreseen operating scenarios maintaining at very low values the unavoidable thermo-mechanical deformations and hence the maximum surface temperature in copper.
With these requirements, the cooling of the grids represents a significantly critical aspect of the NBI design. On one hand the coolant properties have to satisfy high resistivity requirements and to be appropriate for the removal of the impinging heat loads, on the other the cooing circuits have to match with the beam optics geometry and the space constraints which severely affect the coolant distribution.
Present chapter reports the R&D activity on the numerical thermo-hydraulic analyses performed on specific sub-models of the accelerator grids, called Single Channel Prototypes (SCPs) together with the complete manufacturing process of leading to the construction and realization of the samples.

3.1 Active cooling of accelerating grids

The accelerating grids, as designed inside MITICA experiment, are approximately 1600 mm high, 840 mm wide (divided into four segments of 400 mm×840 mm for alignment and manufacturing reasons) and 17 mm thick.
Each grid features 1280 apertures (320 per segment), grouped in four beamlet groups with 16×5 apertures.
Due to the very high heat load deposited on the electrostatic grids such devices has to be designed with a proper active cooling system realized through embedded channels lying beneath the upstream surface of each segment.
These channels shall couple the optical design of the grids and shall therefore be located in between the various openings.
In addition to the cooling channels the grids contain embedded permanent magnets below the downstream surface used to deflect the co-extracted and stripped electrons preventing them to be accelerated together with the negative ions in the accelerator [13].

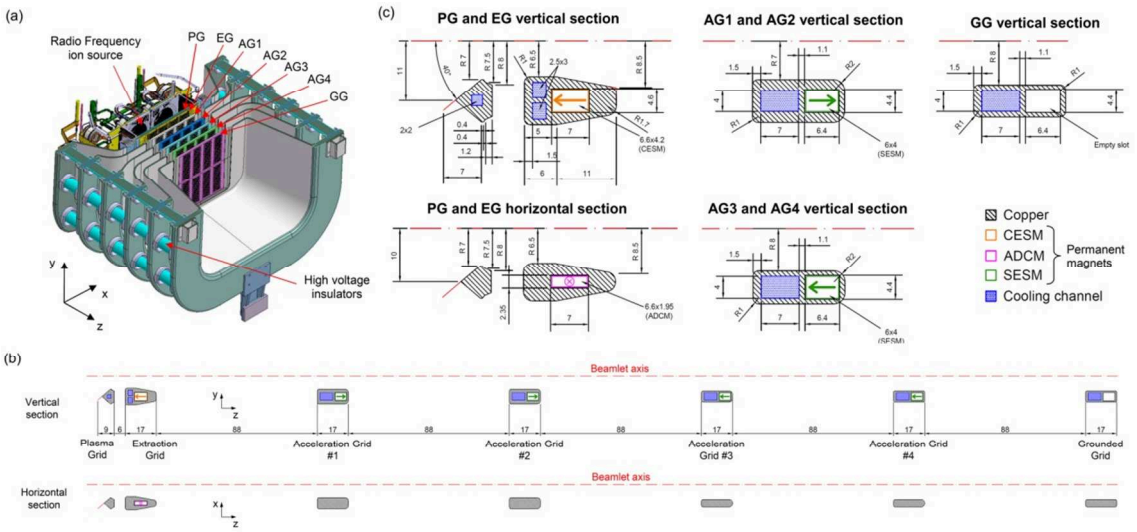

Figure 3.1 - Design of the MITICA extractor/accelerator system. (a) isometric view of an horizontal section of the whole beam source; (b) vertical and horizontal sections in the aperture area; (c) detail view of the most relevant sections.

In order to provide the most uniform heat sink along the different electrostatic grid, it has been necessary to locate the different horizontal channels in parallel connection along copper structure. The fact that the 4 segment are vertically piled imposes the channels to be obtained along the longitudinal direction of each segment in order to guarantee the possibility of a feasible supply and draining of the coolant fluid.
With the aim of guarantying the most uniform distribution of the cooling fluid inside the different channels two side common vertical manifold have been integrated into the design just before different fluid inlet and outlet cavities.

Aside these cavities two external stainless steel manifolds are foreseen in order to collect and convey the coolant fluid from or to a single feeding or draining duct per each segment.

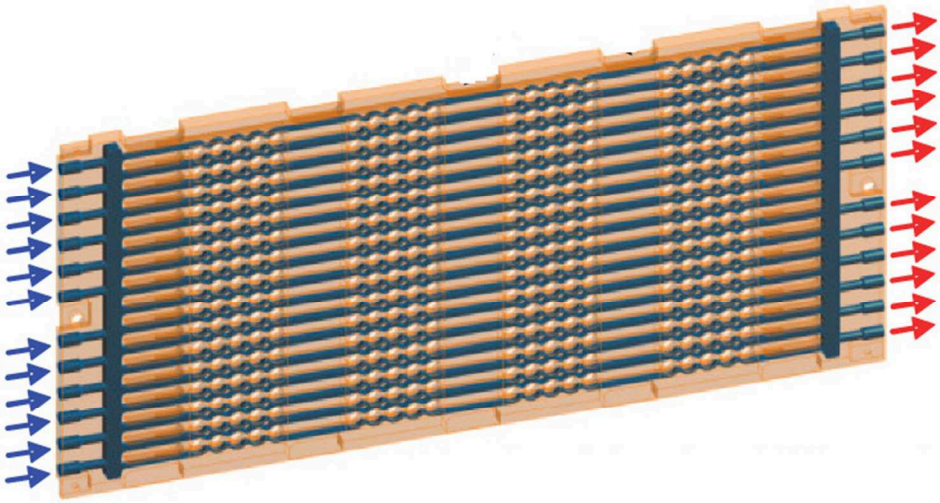

Figure 3.2 - Schematic representation of the accelerating grid heat exchanger in transverse configuration.

Due to the limited space available for the external manifold and feeding and draining pipes it is preferable to develop the heat exchanger design with transverse cooling channels. Notwithstanding the thermodinamycal drawbacks of this solution such design would limit the external manifold and feeding and draining pipes to a single one per each side of the various segment.

The heat load profile is a fundamental input parameter for the identification of the appropriate cooling system capable to remove in the most effective way the deposited power. With the aim of developing the highest performing set of cooling channel designs to be embedded in the electrostatic grids the power load which has been applied on the four different beamlets groups shall be necessarily the most demanding one among all the different estimations obtained from EAMCC code.

Despite the fact that the highest predicted value in terms of impinging heat flux has been determined to be reached on AG2, it has been decided to adopt the one acting on AG4. Though the peak associated to the heat load applied to AG4 is just the half of the one acting on AG2, the spatial distribution is highly biased along the annulus of the beamlet opening leading the exhausting operation much more difficult without requiring high performing design. A heat load of 10 MW/m^2 has to be indeed cooled very close to the deposition of power leading the requirements for the cooling system to become very stringent.

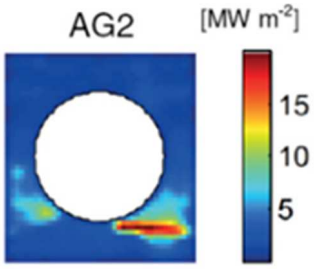

Figure 3.3 - Spatial heat load distribution over AG2.

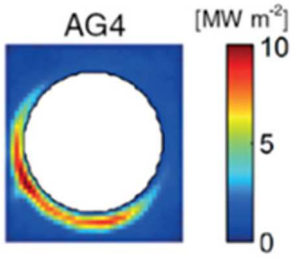

Figure 3.4 - Spatial heat load distribution over AG4.

Since the uncertainties which still affect the power loads estimation are still considerable an additional prescription is to develop a single phase flow heat exchanger which could guarantee a sufficient safety margin from reaching critical heat flux conditions though sacrificing a better heat exchange mechanism.
The peculiarity that the grids are set to an elevated voltage difference with respect to ground potential imposes a last requirement in term of choice of the cooling fluid. The deigned coolant should indeed guarantee the capability to maintain the electrical insulation between the different electrostatic components at ground potential and the highest potential design in the injector.
In order to accomplish this requirement it has been decided to consider ultrapure water as default option for the cooling of the grids. Such choice would be able to guarantee good cooling capabilities, proper electrical insulation and good compatibility with nuclear environment although requiring costly purification system and further investigation of its electrochemical behaviour (i.e. corrosion mechanism)

3.2 Accelerating grid requirements

The operation of the NBI will be carried out in pulsed state (cf. Table 1.3). In order to guarantee a sufficient life-time associated to the cycling application of thermal mechanical loads the mechanical design of the accelerating grids has to fulfil different requirements both from the thermal and structural point of view [15]. In particular they should be characterized by

- A peak temperature on the grids as low as possible, and in any case lower than 300°C (beyond this temperature the copper thermo mechanical properties sensibly worsen);
- Stress peaks as low as possible, and in any case satisfying the appropriate Structural Design Criteria for In-Vessel Components;
- Fatigue life as long as possible, and in any case satisfying the Structural Design Criteria for In-Vessel Components (50000 beam on/off cycles).
- Acceptable alignment among all the grids in a suitable range of operating scenarios and always lower than 0.2 mm.

Among the different requirements, the one regarding the fatigue life have resulted as the most critical to accomplish, while all the others were found to be accomplished in a much straightforward way. The fatigue characteristics of electrodeposited copper were similarly measured during a dedicated experimental campaign.
With the purpose of taking into account an appropriate safety margin, as stated in the SDC-IC criteria, the strain-cycle curves considered in the assessment of grids fatigue life resulted to be significantly much conservative than those derived from laboratory tests [16].
As easily noticeable in Figure 3.5, it can be noted that in order to perform a fatigue life larger than the prescribed 50000 beam on/off cycles, it is necessary to obtain values of equivalent Von Mises total strain range lower than 0.169% over the all domain of each accelerating grid.

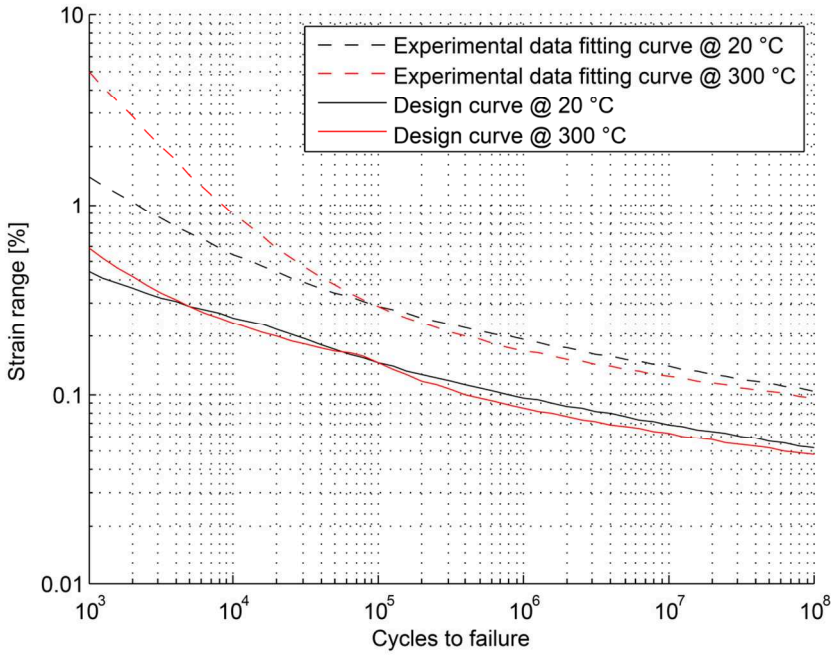

Figure 3.5 - Experimental and design fatigue curves.

3.3 Identification of the Objective

In order to best convey the efforts, it has been chosen at first to study in deep the given literature on thermal fatigue for metallic materials.
Thermal fatigue is defined as the progressive damage and eventual final rupture of a material due to cyclic stresses caused by alternate heating and cooling stages in which thermal expansions are partially or completely prevented.
Up to now thermal fatigue testing has not reached a standardization level equal to that of the experiments conducted in the field of mechanical fatigue. As a matter of fact it is

then not so easy to compare the different results achieved through the different experiences.
The difficulties arise from the fact that the same thermal cycle may cause different stress states depending on the geometry of the specimen, on the applied mechanical constraints, on the solution used to supply and exhaust the heat during the test.
A general theory for the prediction of component fatigue life has been developed and involves different yield criterions. Among these it is worth noticing the approach proposed by Von Mises.
Such criterion states that the yield strength of the material is reached when the strain distorting energy reaches a limit value. Such distortional deformation energy has to be meant as the fraction of the elastic deformation energy linked to variation in shape and not in terms of volume of the body.
As a matter of fact the duplex objective is to minimize thermal gradients and temperature field of the accelerating grids, which are the effective drivers for the distortion of original shape of the structure.
From the thermo-dynamical point of view this is equivalent to identify cooling design solution which could perform the heat transfer process from the accelerating grid to the coolant fluid with higher efficiency.
Such efficiency concept is translated through the second principle of the thermodynamics in minimizing the entropy generation reducing to the maximum extent the thermal gap between the copper and the ultrapure water.
In addition to the temperature control approach there are a number of methods and devices able to improve the fatigue strength of a mechanical component in order to further improve the fatigue strength of a mechanical component. Such methods can be grouped in four categories:

1) Drawing devices:

   Design expedients are all those changes made without changing the functional aspects of the shaped body in order to avoid or limit the concentration of stress in the most solicited areas. A typical feature adopted is the filleting of sharp edges. Another possibility is constituted by shadow effect: this is creating appropriate additional slots inside the structure in order to divert the flows of stress thus decreasing the concentration in the most stressed points. Particular attention must be finally placed for welding since they generally record a lower fatigue limit. An effective remedy to limit such reduction involves milling welding cord.

2) Residual surface stresses:

   This method is based on the principle that a component under a cyclic stress has a longer life if the maximum stress level is reduced. To perform such condition it is possible to create a state of compressive preload nearby the

critical point region. When such compressive preloads are algebraically added to those stresses derived from the applied boundary conditions, such preset stress profile provides an effective decrease of maximum stress. The methods exploited to generate residual stresses are various (e.g. rolling) and all are based on the concept of plastically deforming the surface of the component in order to induce, just below the outer layer, a negative elastic deformation which persists in time in reason of the above plastically deformed material layers.

3) Thermal treatments:

   The thermal treatments constitutes a particular device able to create high surface compressive residual stresses that in some cases can even double the fatigue strength. These methods consist of treatments called surface hardening as nitrurization, cementification and surface hardening. It should by the way pay attention to the fact that the surfaces residual stresses are very high, and it could occur that at a certain depth, tensile stresses arise leading to rather limited fatigue life cycle expectancy.

4) Choice of material:

   The choice of the material is not exactly a method to improve the fatigue resistance because it is an essential design step. In the particular case of thermal fatigue preferable materials are those characterized by high thermal conductivity in order to reduce temperature gradients with equal heat flow. Additional advisable positive features regard a low value both of the thermal expansion coefficient and Young's modulus.

In such studies particular attention has been paid on the first category of advised methods introducing to the design of the electrostatic grids a number of Stress Relieving Slits (SRS). These would allow the grids to have a better deformation, with lower peaks of stresses and strains. In particular such slits are limited to a fraction of the thickness of the grid, leaving a copper layer on the front side in order to prevent from bad optics particles or undesired electrons to be further accelerated and eventually imping on downstream components of the injector at higher energy contributing to an additional and undesired thermal power load.

3.4. Present Design Solution

The NICE (Nozzle Island Cooling Enhancement) acted as the starting point for the development and optimization of further high performance cooling designs options. This solution is able to provide good cooling performance by means of two parallel design guidelines: approaching the channel walls to the heat load footprint (thus

reducing thermal conducting resistance) and increasing the laminar heat transfer coefficient with the introduction of turbulence due to streamline curvature in the most thermal loaded areas. Furthermore the reconnection of the two 7 mm x 2 mm channels is another crucial aspect able to increase the average hydraulic diameter thus limiting pressure losses.

An additional characteristic of this concept is a cooling channel design featuring a larger cross section (7 mm x6 mm) in the non-heated parts (i.e. where an intensive cooling is not desired because it would increase the temperature difference with respect to the heated parts).

A set of 15.5 mm thick stress relieving slits have been inserted in the frame regions of the electrostatic grid in order to further decrease the associated equivalent strain.

Due to the fully accomplishment of the different thermal and structural requirements imposed on the electrostatic grids such cooling channel concept was integrated in the final design of MITICA beam source [17][18].

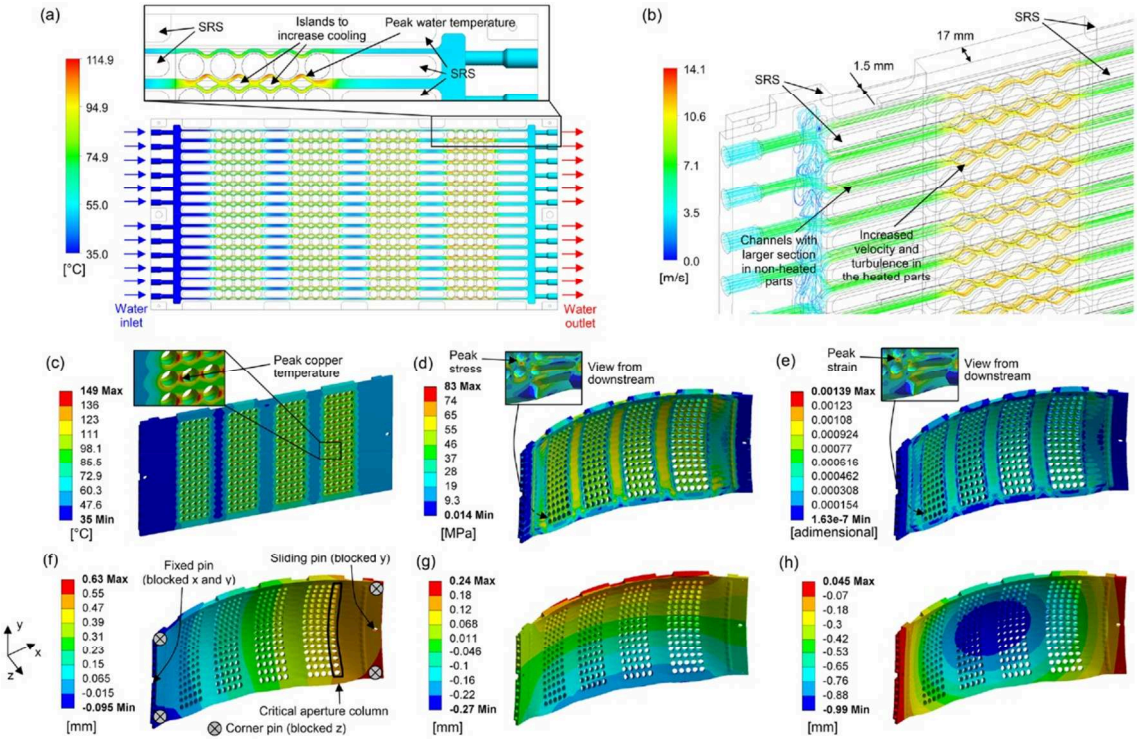

Figure 3.6 - Main results of the thermo-structural analysis for AG4 with the NICE and SRS enhancement, as calculated with the fully self-consistent fluid-thermal-structural segment model: (a) water temperature at the channel wall; (b) effect of NICE concept on water turbulence; (c) copper temperature; (d) equivalent (Von Mises) stress; (e) equivalent (Von Mises) total strain; (f) deformation along X-direction; (g) deformation along Y-direction; (h) deformation along Z-direction.

The novel design proposals were conceived by further extending these guidelines, considering that, in the heated region, an almost uniform cross section and additional turbulence injection are both wanted.

3.5. Single channel Prototypes (SCPs)

As mentioned in the previous paragraphs the present and novel cooling channels designs of the grids have to match the geometrical constraints coming from beam optics optimizations, and face the space constraints that severely affect the coolant distribution. Since the cooling channels have rectangular shape and hydraulic diameters in the order of few millimeters (3÷6.5 mm), the numerical and experimental evaluation of the thermo fluid-dynamical performance could be complex.

The need to perform reliable measurements of the thermo-hydraulic performances of present and novel cooling channels design, in order to support the design hypotheses and assumption, and the need to demonstrate the feasibility and reliability of the manufacturing process needed to be adopted during the construction activity led to the decision develop the novel design proposal on an appropriate subdomain of the whole accelerating grid in order to be manufactured and successively tested in a dedicated test facility.

The subdomain that has been chosen is a single group of opening to be modeled in a 230 mm x 22 mm x 17 mm prototype as depicted in Figure 3.7.

The experimental results shall be compared with the results coming from Computational Fluid-Dynamics (CFD) models of the Single Channel Prototypes (SCPs), so that appropriate modelling parameters can be identified. The result of such experimental benchmarking could lead to the possibility to perform CFD models of full scale components capable of providing reliable results.

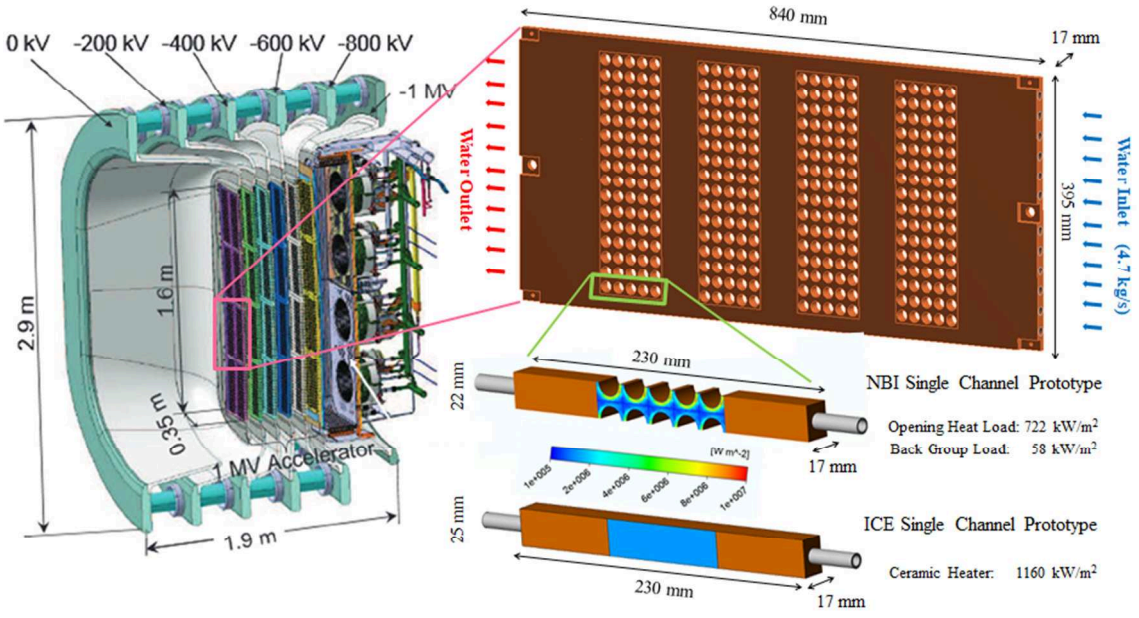

Figure 3.7 - Graphical representation of the sub-modeling process leading to the definition of the single channel prototypes.

3.6. Research Methodology Approach

Due to the impossibility of reproducing the experimental conditions foreseen in the neutral beam injector, the research activity has been subdivided in four different and consequential steps:

a) Numerical simulations considering the operating scenarios foreseen during the ITER NBI operations;
b) Prototype Manufacturing;

c) Numerical simulations considering the operating scenarios foreseen in the ICE facility. This is a facility of Consorzio RFX used to simulate the operating conditions of the cooling systems for high heat flux components;

d) Experimental tests in the ICE facility;

The first step provided a numerical test bed for the validity of the new design proposals under the application of the reference thermal loads. The geometries defined in this step provide the manufacturing design inputs. The third step is instead aimed to benchmark the different fluid-dynamics models in CFX and FLUENT solvers determining how closely the models can predict the numerical results with those derived from the experimental campaign in the ICE facility, the final step. Due to the objective difficulties in reproducing the reference thermal load given by the NBI beamlet optic, in this facility the applied heat flux is the one given by the exploitation of ceramic heaters. As a result the spatial distribution of the thermal load is no more annular but uniform along the whole heated surface.

3.7. Design Constraints

Besides the thermo mechanical requirements a further set of design constraints has to be taken into consideration in developing the new set of high performance cooling systems.

- Pressure Drop

  It is mandatory to provide solutions for different grid geometries, able to lower the temperature gradients to the maximum reasonable extent without determining an excessive amount of pressure drop along the cooling circuit. In particular it has been set as maximum hydraulic loss the one admitted along one segment in MITICA experiment (6 bar).

- Structural requirements

In order to guarantee robustness to the design the walls composing the limit of the cooling channels should guarantee a minimum gap of 1.5 mm from the heated upstream surface and 1 mm from all the other cavities or external boundaries.

- Vibration and Erosion phenomena

Despite the fact that erosion mechanisms between copper and ultrapure water are still issue to be further investigated, water velocity on channel walls has been set to be as close as possible to the maximum one reached into present design solution (15 m/s).

- Geometrical constraints

The design of the cooling channel has to take into account the present of the cavity (6.4 mm x 4.4 mm) to host SESM magnets.

- Technological limit

The required penetration depth of the milling machine limits the mill minimum diameter to 1.2 mm. Such value has then to be taken as the minimum height of the designed cooling channels.

- Design Flexibility

The realized designs should be able to be implemented on the different electrostatic grids hence granting the universality of the cooling solution for the all accelerating stage. It is also recommended to prefer, as far as reasonably possible, cooling channels design which could guarantee the vertical and horizontal symmetry of the electrostatic grid in order to avoid any possible error during the mounting phases.

3.8. Boundary Conditions

The boundary conditions applied in the different modeling configurations (Injector and test facility) result equivalent apart from the applied thermal loads applied on the upstream surface.

Table 3.1 - List of boundary conditions appleid to the numerical models.

Fluid inlet conditions:	
- **Water Inlet Mass flow**	0.29375 kg/s
- **Water Inlet Temperature**	35°C

Fluid outlet conditions:	
- **Relative External Pressure**	0Pa

Copper boundary conditions:	
- **Channel Wall Roughness**	2 µm
- **Upstream Thermal Load**	From AG4 - 1160 kW/m²
- **Downstream Thermal load**	58.854 kW/m² - Insulated
- **Opening Thermal load:**	722.267 kW/m² - Insulated
- **Other surfaces**	Insulated

The different input in the copper boundary conditions table refers respectively to the injector-like and test bed-like configuration. Water and Copper domain have been modeled with temperature dependent thermofluid-dynamical and physical properties withdrawn from IAPWS libraries and Material Properties Database (MPDB).

3.9. Novel enhanced Proposals

After an extensive CAE campaign, ten innovative design solutions have been considered of technical interest and worth to be manufactured as prototypes.
The present MITICA cooling solution acted as the starting point for the development of the novel proposals.
Two parallel guidelines have been followed:

- Approaching the channel walls to the heat load footprint, thus reducing the thermal conducting resistance of the interposed copper material;
- Increasing the liminar heat transfer coefficient with the introduction of extended surfaces able to improve the energy transport and turbulent mechanisms at the heated surface.

These solutions can be categorized in four classes:

a) Single Straight Channel:

This option (A) represents the original cooling solution for the electrostatic grids of the injector. Despite the incompatibility of such design with the requirements imposed on accelerating grids segment, it has been inserted in the set of prototypes to be manufactured due to its suitability to compare the experimental results with the analytical correlations derived from the literature.

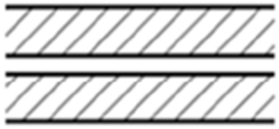

Figure 3.8 - Single Straight Channel cooling module detail (Option A).

b) Increasing channel wall surface through sub-channels insertion:

Option B1 is the solution currently applied inside the MITICA experiment, with a doubling channel pattern in correspondence of the beamlet apertures.
Options B2, B3, B4 and B5 are characterized by an increased streamline curvature (overall bend amplitude has been increased from 12 to a maximum of 17 mm) in order to further enhance the coupling with the thermal load footprint. The different cooling solutions are characterized by the same minimum width of the sub-channels (1.2 mm), able to guarantee the highest ratio between wet surface and transversal cross section.
B2 is a straight variation of the NICE design with a modified overall curvature of the channels (15 mm).
B3, B4 and B5 are more elaborated alternative concepts. They are all characterized by the same overall curvature of the extreme channels (17 mm) while changing the number and shape of the inner copper elements separating the different sub-channels.

Figure 3.9 - NICE Channel cooling module detail (option B1).

Figure 3.10 - NICE Upgrade Channel cooling module detail (option B2).

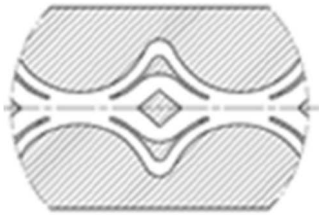

Figure 3.11 – Baffle Channel cooling module detail (option B3).

Figure 3.12 – Criss Cross Channel cooling module detail (option B4).

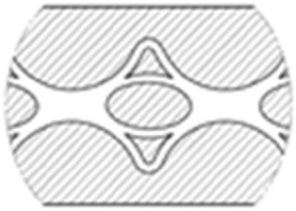

Figure 3.13 - Diverted Channel cooling module detail (option B5).

c) Increasing channel wall surface through channel height modification:

Option C1 and C2 proposes a single or doubling cooling channel where the increasing channel height is compensated by a reduction of channel depth.
As far as C2 option is concerned the particular topology of the heat load has suggested the interposition of a central body in order to increase the wet surface and re-routing the flow in areas characterized by higher heat loads. A drawback is the corresponding reduction of the channel depth in order to limit hydraulic losses.

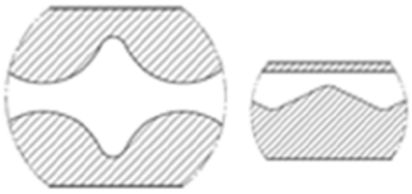

Figure 3.14 – Duned Channel cooling module detail (option C1).

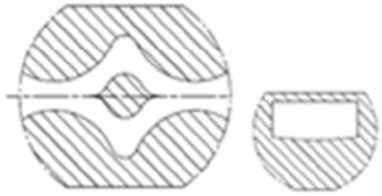

Figure 3.15 – Duned Drag Channel cooling module detail (option C2).

d) Insertion of turbulent injector devices:

This latter class of proposal is, in terms of design, the exact reference solution (option B1), but with the introduction of additional turbulence injector devices. Such injector devices consist of 11 blended ribs tilted with respect of the streamline direction by an angle of 90° (i.e. perpendicular to the plate surface) in D1 or 45° in D2. These ribs are designed with a radius of 0.25 mm, along a wall curvature of 9.25 mm so that the minimum distance from the aperture is kept the 1 mm, satisfying the constrains. The depth of the ribs has been set to 2 mm as reasonable trade-off for increasing heat transfer coefficient without severe penalization in terms of pressure drops.

Figure 3.16 – NICE Turbotron cooling module detail (option D1).

Figure 3.17 – NICE Tilt Turbotron cooling module detail (option D2).

All the different proposals have been assessed with sensitivity analysis, evaluated in steady state CFD simulations and compared in terms of thermo-hydraulic characteristics. Among these, particular attention was given to pressure drop, laminar velocity and cooling performances.

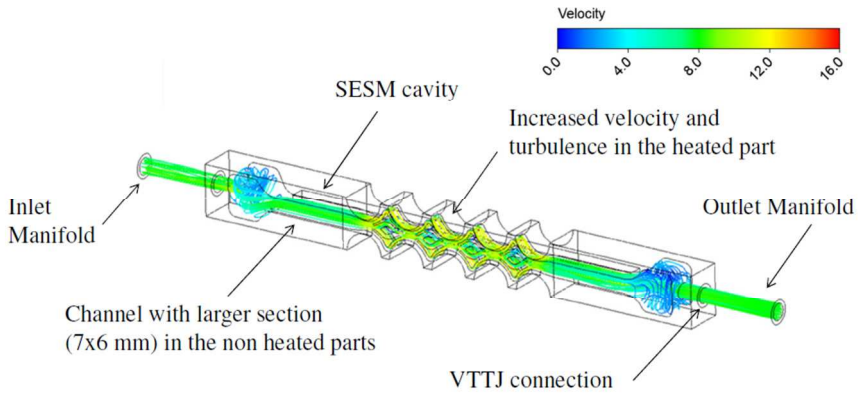

Figure 3.18 – Overview of the main characteristics of SCP in injector-like configuration.

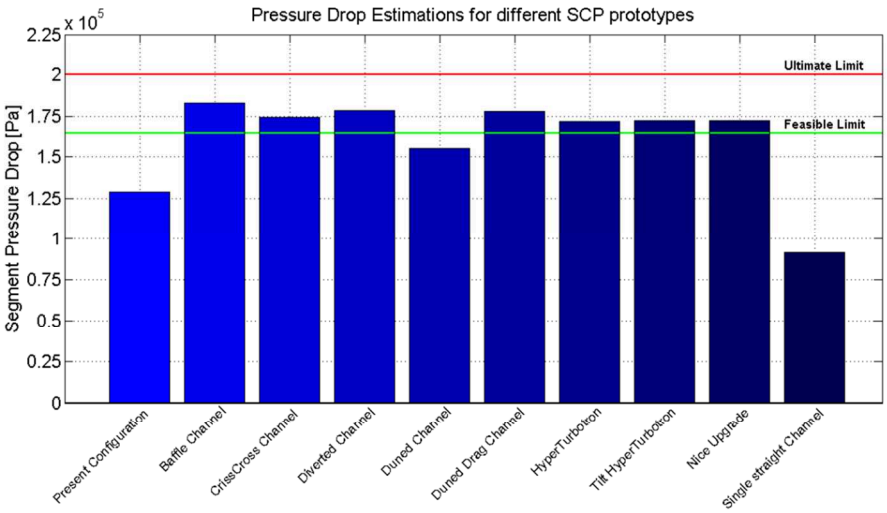

Figure 3.19 – SCP Pressure drop in injector-like configuration.

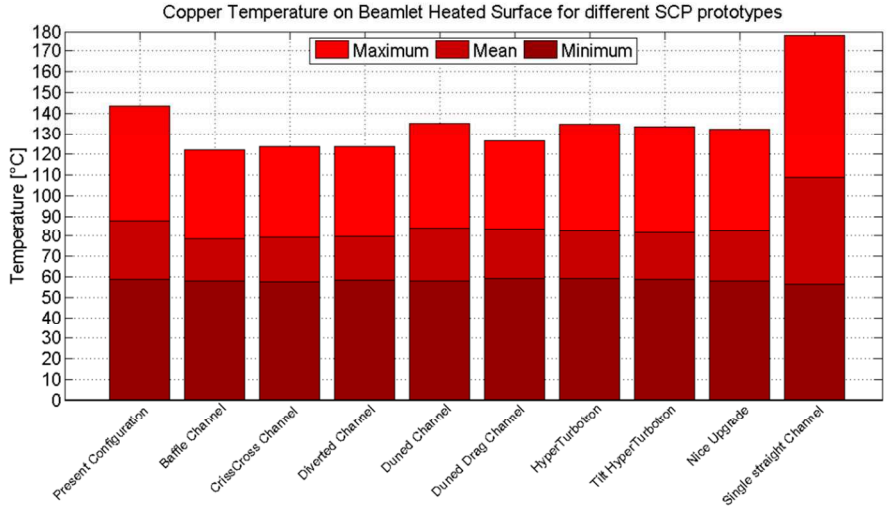

Figure 3.20 – SCP copper temperature on beamlet heated surface in injector-like configuration.

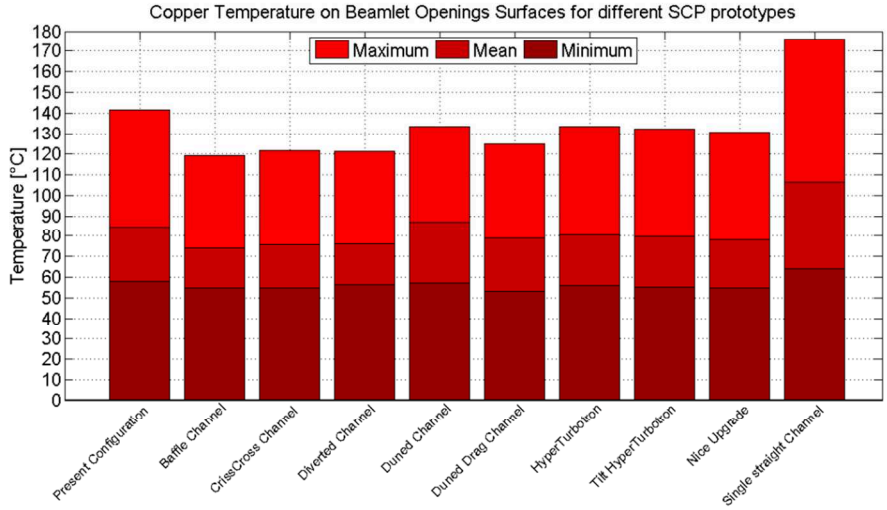

Figure 3.21 – SCP copper temperature on beamlet opening surfaces in injector-like configuration.

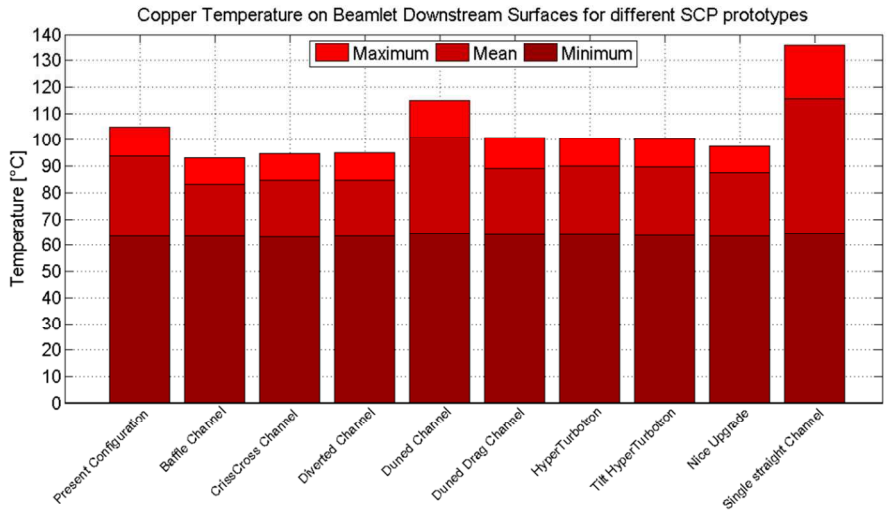

Figure 3.22 – SCP copper temperature on downstream surface in injector-like configuration.

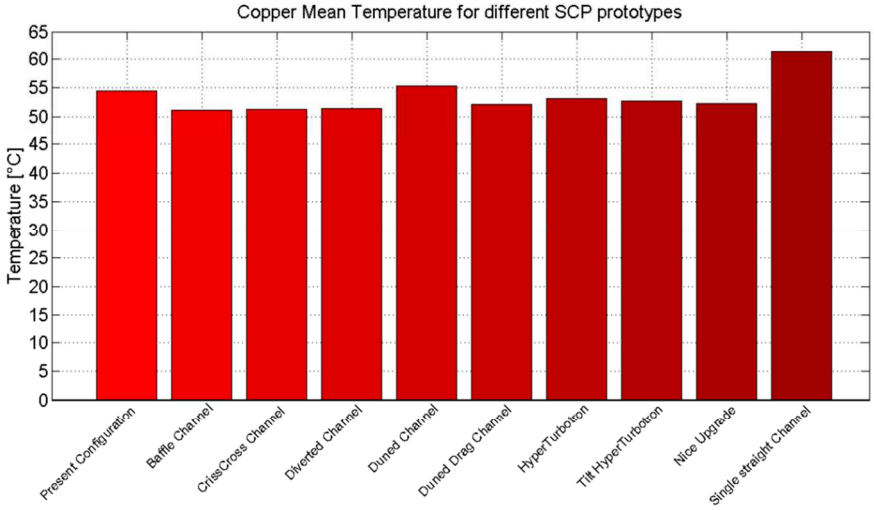

Figure 3.23 – SCP copper mean temperature in injector-like configuration.

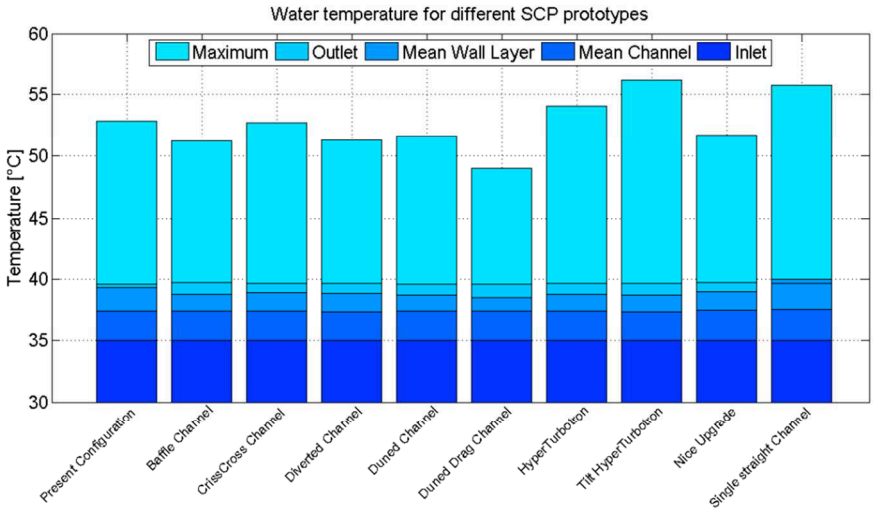

Figure 3.24 – SCP water temperature in injector-like configuration.

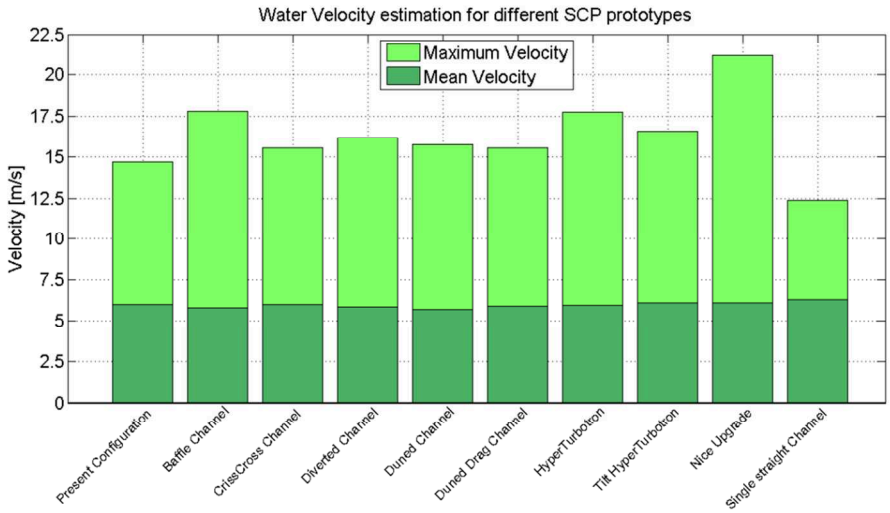

Figure 3.25 – SCP channel water velocity in injector-like configuration.

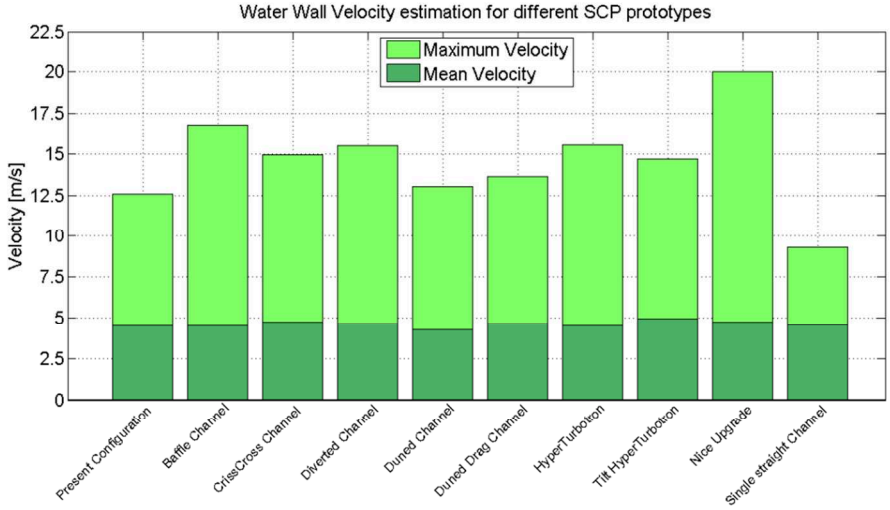

Figure 3.26 – SCP channel water wall velocity in injector-like configuration.

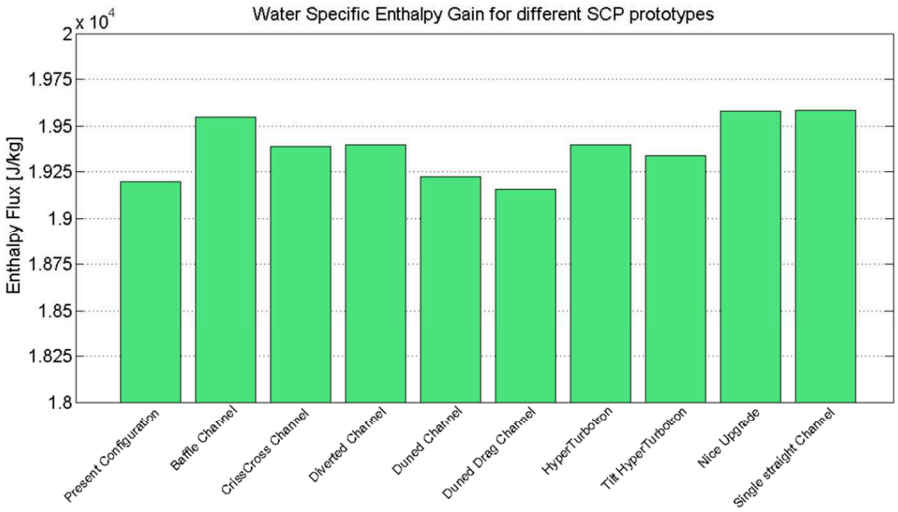

Figure 3.27 - SCP channel water specific enthalpy gain in injector-like configuration.

In Figure 3.19 the feasible and ultimate pressure limits have been set taking into consideration the estimated pressure drop along the electrostatic grids with present design configuration (NICE). During such numerical analysis campaign the overall hydraulic losses over the accelerating segment attested to 4.60 bar, providing 1.40 bar of margin from the maximum tolerable loss admitted by the cooling circuit performance.
Such pressure drop can then be equally distributed to the four cooling modules in the respective beamlet groups (0.35 bar) which added to the present insisting on the SCP with NICE configuration of the cooling channels (1.29 bar) leads to the possibility of realizing SCP proposals being characterized by an overall hydraulic loss of about 1.65 bar without infringing the 6 bar pressure drop requirement over the full scale segment grid.
Despite 1.65 bar prescription as feasible pressure limit for the different SCP design a further one has been imposed and set to 2.00 bar (ultimate pressure limit) in order to be able to explore a wider range of solutions which could be able to perform better cooling solutions containing the hydraulic losses in a reasonable range for next generation of accelerating grids (7.5 bar).
The analyses have been replicated with the heat loads foreseen during the tests in the experimental facility (1.16 MW/m^2). For the sake of brevity the results are resumed in Table 3.2. Moreover, some options are highlighted to show the best cooling configuration, the design with the lowest pressure drop penalty, and the geometry which obtains the best compromise between the thermal gain and the additional cost in terms of pressure drop.

Table 3.2 – Numerical estimation of Pressure Drop, Maximum Temperature and Channel Wall Velocity.

		NBI Configuration			ICE Configuration		
	Design Solution	Δp [bar]	T_{max} [°C]	V_{wall} [m/s]	Δp [bar]	T_{max} [°C]	V_{wall} [m/s]
✓	Baffle Channel	1.83	120.86	16.68	1.76	61.75	16.43
	Criss-Cross Channel	1.76	130.02	15.13	1.67	67.32	15.24
	Diverted Channel	1.79	123.54	15.51	1.68	62.95	15.82
✓	Duned Channel	1.56	131.96	14.04	1.49	68.59	13.57
	Duned Drag Channel	1.78	126.44	13.66	1.70	64.89	12.95
✓	NICE Channel	1.29	143.48	12.60	1.22	73.83	12.57
	NICE Upgrade	1.73	132.46	20.04	1.63	68.78	19.47
	Turbotron Channel	1.72	134.91	15.52	1.64	69.48	14.86
	Tilt Turbotron Channel	1.70	133.64	14.67	1.59	68.83	14.42
✓	Straight Channel	0.92	178.31	9.29	0.85	84.58	9.14

✓ Present Project Design ✓ Best Thermal Behaviour ✓ Best Hydraulic Behaviour ✓ Best Coupled Thermal-Hydraulic Behaviour

3.10 SCP Manufacturing

The manufacturing of the Single channel prototypes has been realized through successive steps:

- Machining of the cooling channels on the OFHC (Oxygen Free High Conductivity) copper plate;
- Copper electrodeposition to close the cooling channels with 1.5 mm layer;
- SCP Cutting and insertion of the AISI 316-L SS feeding and draining tubes;
- Copper electrodeposition to couple the AISI 316-L SS feeding and draining tubes through Vacuum Tight Threaded Junction (VTTJ) technique [19];
- Machining of the thermocouple's housing grooves;
- Finishing;

During the machining of the cooling channels on the OFHC copper plate the different geometries have been realized with high accuracy by the machinery owned by the supplier demonstrating the technological reliability of the manufacturing process.

Figure 3.28 - Manifold milling operation

Figure 3.30 - Baffle channel cooling group milling.

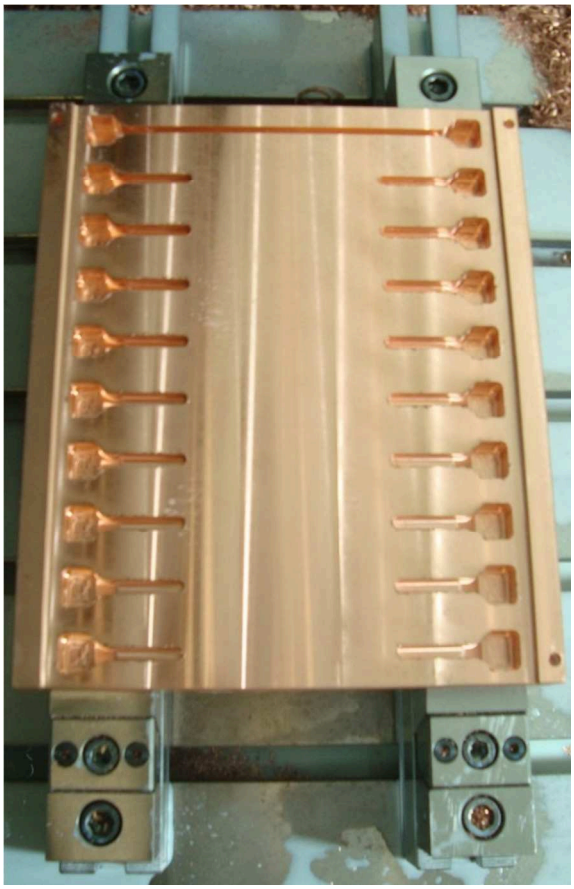

Figure 3.29 - Completion of inlet and outlet frame sections.

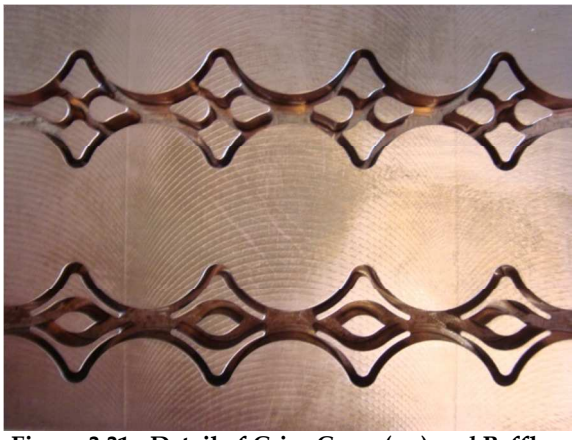

Figure 3.31 - Detail of Criss-Cross (up) and Baffle (down) Channels cooling groups.

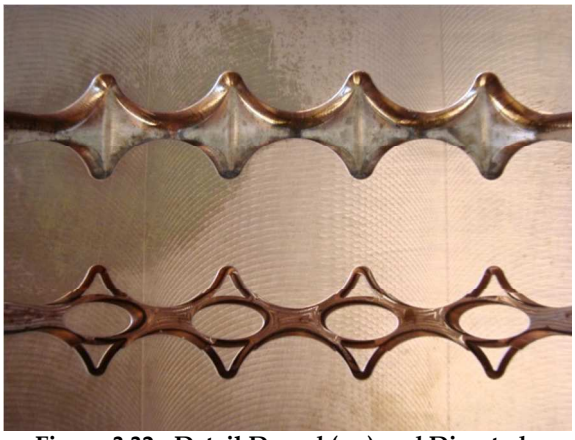

Figure 3.32 - Detail Duned (up) and Diverted (down) Channels cooling groups.

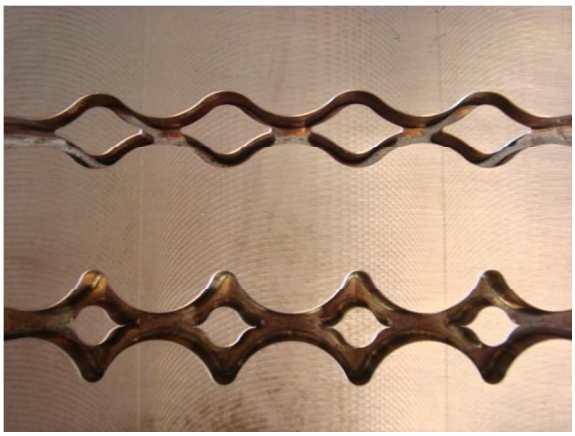

Figure 3.33 - Detail of NICE (up) and Duned Drag (down) Channels cooling groups.

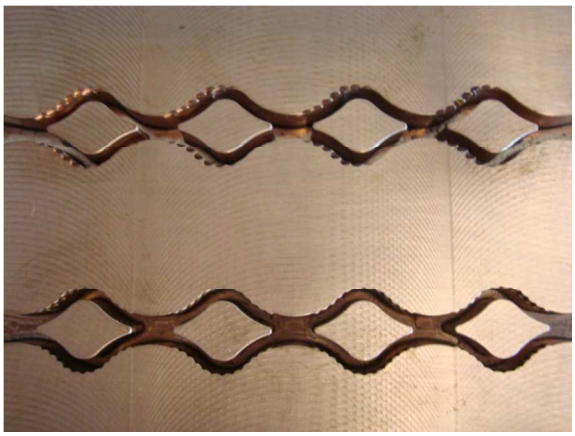

Figure 3.34 - Detail of Tilt Turbotron (up) and Turbotron (down) Channels cooling groups.

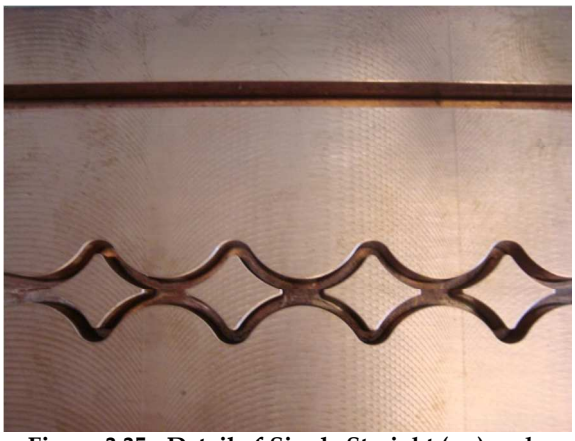

Figure 3.35 - Detail of Single Straight (up) and NICE Upgrade (down) Channels cooling groups.

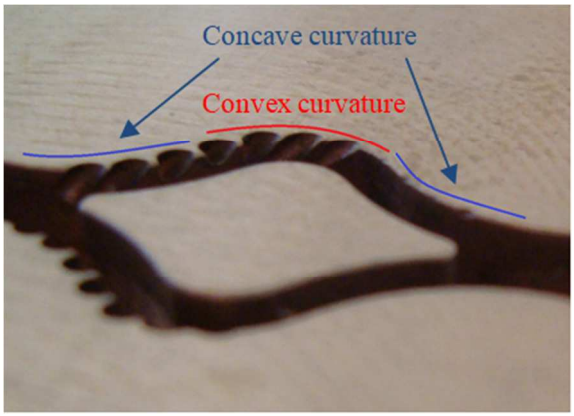

Figure 3.36 - Detailed view of the inclined ribs in Tilt Turbotron Channel.

Some difficulties were faced during the realization of the inclined ribs of the Tilt Turbotron channel option, due to the employment of a 3-shafts milling rather than a 5-shafts one. The ribs were indeed projected with a fixed tilt of 45° along the streamline direction and inclined in the transversal plane in order to follow the channel wall

curvature. This feature did not allow a correct penetration of the mill along the designed direction realized on the CAD. The ribs were eventually created just in those regions where the curvature did not turn from concave to convex along the milling direction, as shown in Figure 3.36. In all the others the bad curvature trend did not permit to the mechanical tool to be held in position by a sufficient material thickness.
If the D2 option would reveal to be so performing to justify its larger manufacturing complexity, the present shortcoming can be avoided either by employing a 5-shafts tool machine or prototyping with a higher accuracy the position where the mill would start the realization of the ribs. Other two possible criticalities identified during the design phase were the minimum copper thickness (0.8 mm) in the B3 option and the realization of the narrowest sections inside water channels (1.2 mm) of B3, B4 and B5. Both issues were successfully accomplished and in case the most performing geometries would be these ones, it could be taken into consideration to prototype the next generation of samples with a more challenging specification (0.7 mm for the copper gap and 1 mm as the minimum water channel cross section).
Before starting the electro-deposition process the copper plate with all the SCPs, shown in Fig.7, has been characterized in terms of channel wall roughness. The measurements defined an average roughness of 1.3 µm along the frame regions and 1.6 µm inside different heat transfer groups.

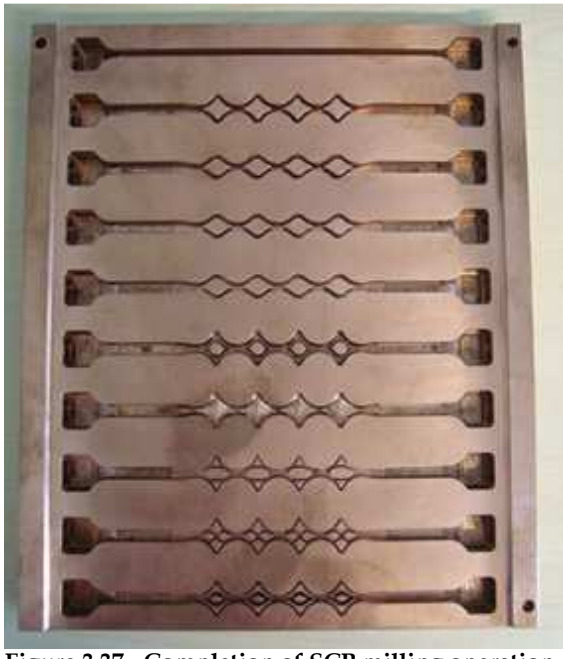

Figure 3.37 - Completion of SCP milling operation.

The supplier was eventually asked to provide the global manufacturing time for each prototype in order to get a preliminary comparison in term of realization costs for the different cooling channel designs.

Table 3.3 - SCP manufacturing time.

Geometry	Manufacturing Time
Baffle channel	4 h 00 min
Criss-Cross channel	4 h 40 min
Diverted channel	5 h 45 min
Duned Channel	1 h 00 min
Duned Drag channel	1 h 30 min
NICE channel	1 h 00 min
NICE Upgrade	1 h 00 min
NICE Turbotron	2 h 30 min
NICE Tilt Turbotron	3 h 15 min
Single Straight	50 min

After the completion of the SCP milling operation the OFCH copper plate was brought to perform to first electro deposition stage in order to close the cooling channels. The operations were carried out starting from filling the channels cavities with wax and a successive accurate leveling. Afterwards the wax surfaces were covered with silver paint in order to activate them for the subsequent electrodeposition process.

Once accomplished the galvanic process the overabundant copper crystals were removed and the plate heated up with free gas flame in order to evacuate the wax still contained inside the channels.
The copper plate was then brought back to the mechanical workshop in order to proceed with the insertion of the stainless steel feeding and draining tubes and sent back to the electrodeposition company to ultimate the VTTJ operations.

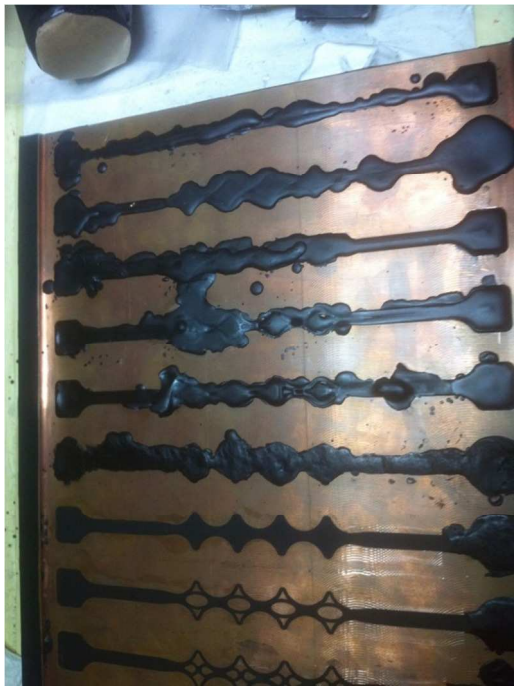

Figure 3.38 - Channel filling with wax.

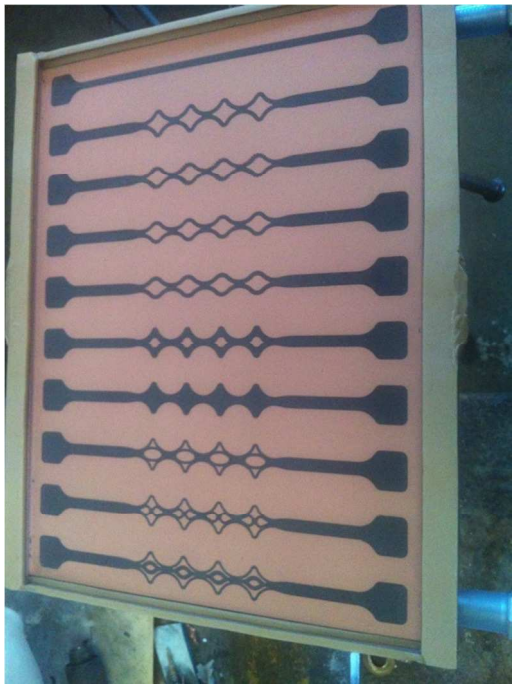

Figure 3.39 - Levelling of channels upper surface.

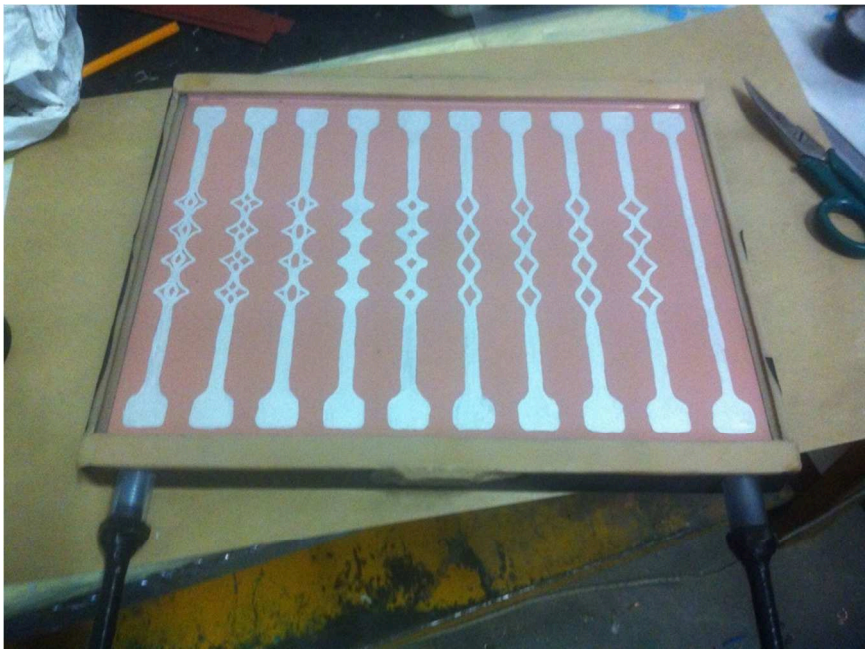

Figure 3.40 - Covering of the channel surface to be electrodeposited with activation silver paint.

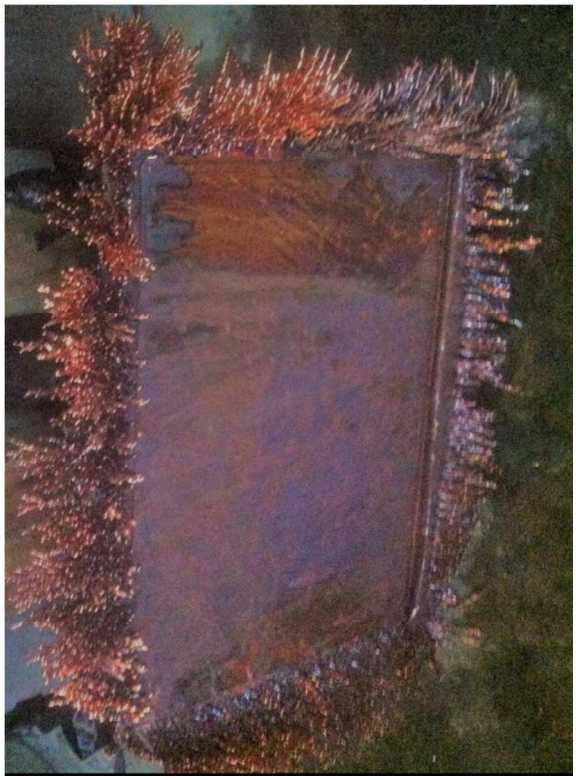

Figure 3.41 - Pulling out of the copper plate from the galvanic bath.

Figure 3.42 – SCP copper plate after completion of the electrodeposition process.

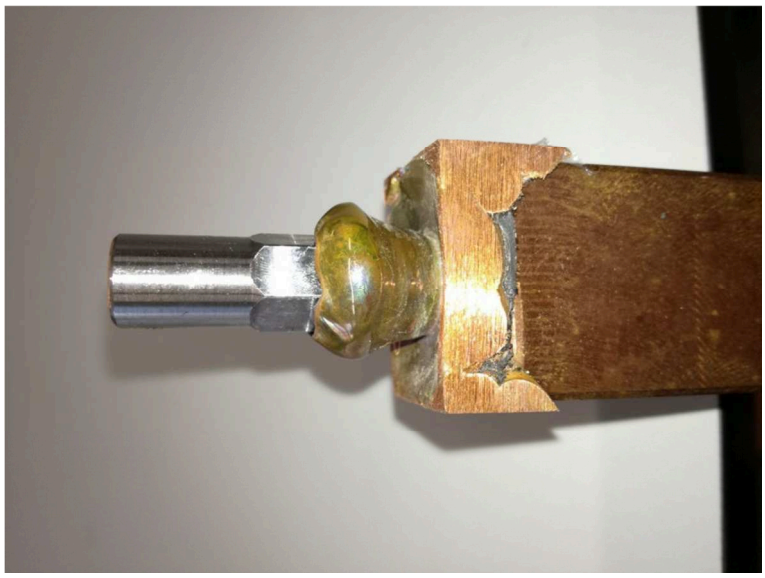

Figure 3.43 - Electrodeposited layer on SS pipes connections.

In order to measure the temperature in a significant portion of the SCP copper domain a set of six threaded grooves have been realized in each SCP in order to host the same number of thermocouples. This has been carried out as the final manufacturing activity. In order to guarantee a flexibility in the employment of the thermal probes and cost containment it has been chosen to exploit a set of thermocouples inserted in an independent M3 x 12 mm screw (0.5 mm pitch) which could be mounted and

unmounted from the different SCP when needed. The thermocouples are of type K as the diagnostic apparatus of the experimental facility can be coupled just with such category of probes. The location of the different thermocouples have been determined as a trade-off position between the channel walls, where the corresponding measures of temperature would be too much levelled by cooling fluid one, and the distance from the heated surface, where a too close position to external face would not be permitted due to the mechanical encumbrance of the groove.
Comparing the different estimated thermal condition of the SCPs a proper position for the thermocouples has been evaluated in 3mm from the heated surface and 5 mm away from the channel walls.

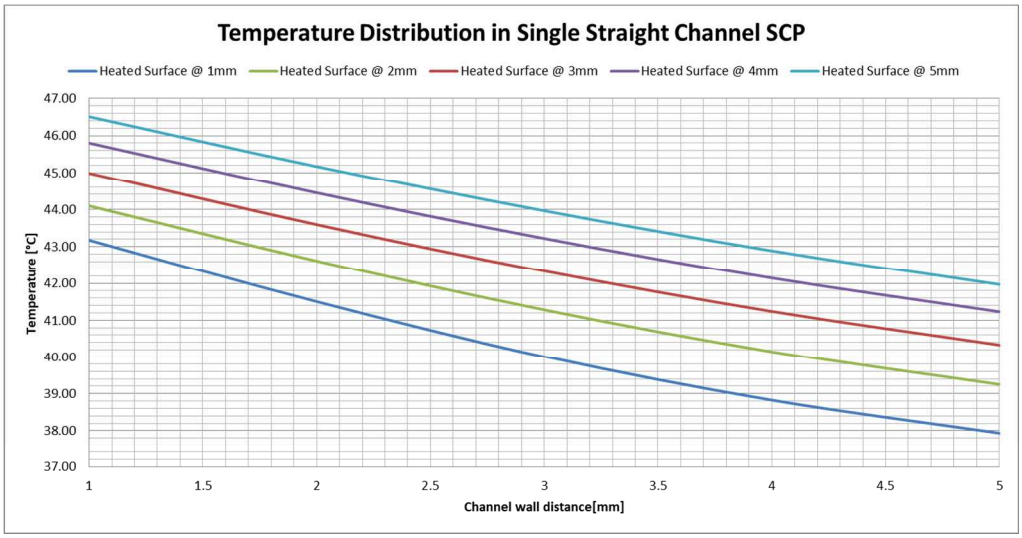

Figure 3.44 - Temperature distribution in Single Straight Channel prototype.

All the different thermocouples have been located symmetrically in between the different cooling modules for all the different SCPs in order to perform a double check of the symmetricity of the analysis and to verify the evolution of copper thermometric state along the direction of the flow of the cooling fluid. The thermocouples have been inserted perpendicularly to the lateral surfaces of the SCP in order to minimize the length the kapton insulated cables inserted into the prototype.

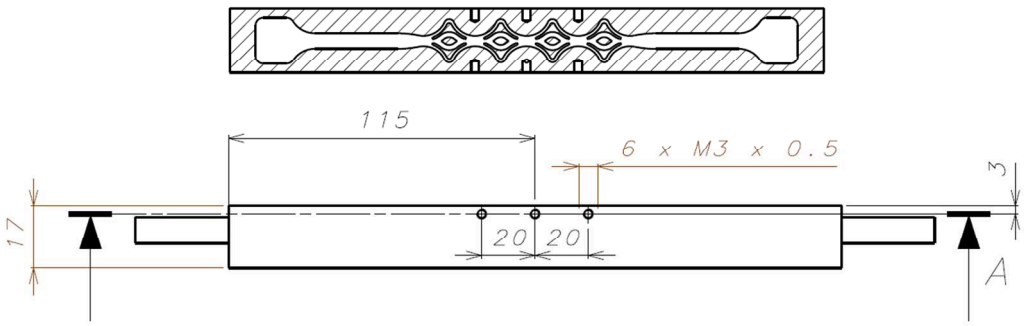

Figure 3.45 - Technical Drawing of Baffle Channel SCP with TCs grooves (side view and A-A section).

4

4. Testing of SCP performance

The different SCPs have been tested in a multipurpose test bed called Insulation and Cooling Experiment (ICE) which has been designed in order to perform thermo-hydraulic and thermo-electric tests on prototype components for the SPIDER and MITICA experiments [20].
The plant is mainly a closed circuit fed by normal or ultrapure water, but it has been conceived to be compatible even with different cooling fluids. In addition, to perform experimental investigations in working conditions relevant for the ITER NBI, a vacuum chamber has been designed.
Different measurement systems have been installed, commissioned and integrated in the control system in view of the bigger PRIMA auxiliary plants.
The ICE plant is characterized by a high degree of flexibility since the full control of any part of the plant allows the test-bed facility to easily adapt to perform new types of tests.
The first section of present chapter presents such multipurpose test bed facility where different fluid-dynamic and thermofluid-dynamic tests on the SCPs have been performed. The experimental campaign has been built with the aim of verifying the results obtained so far numerically and to rank the cooling performances of the different prototypes according the data recorded during the experimental tests.
The out coming results of the thermo-fluid hydraulic tests performed on the SCPs in the ICE plant are then given. The last section of this chapter deals instead with the validation of the numerical predictions obtained through the exploited Computational Fluid Dynamics models.

4.1 General Description of the ICE plant

The ICE plant has been conceived with two test sections, one where the ultrapure cooling water resistivity and degradation are tested and one for thermo-hydraulic experiments. The two parts share services like water pumps, reservoirs and heat exchangers to distribute the coolant fluid with controlled temperature and flow rate to the inlet of the test sections.

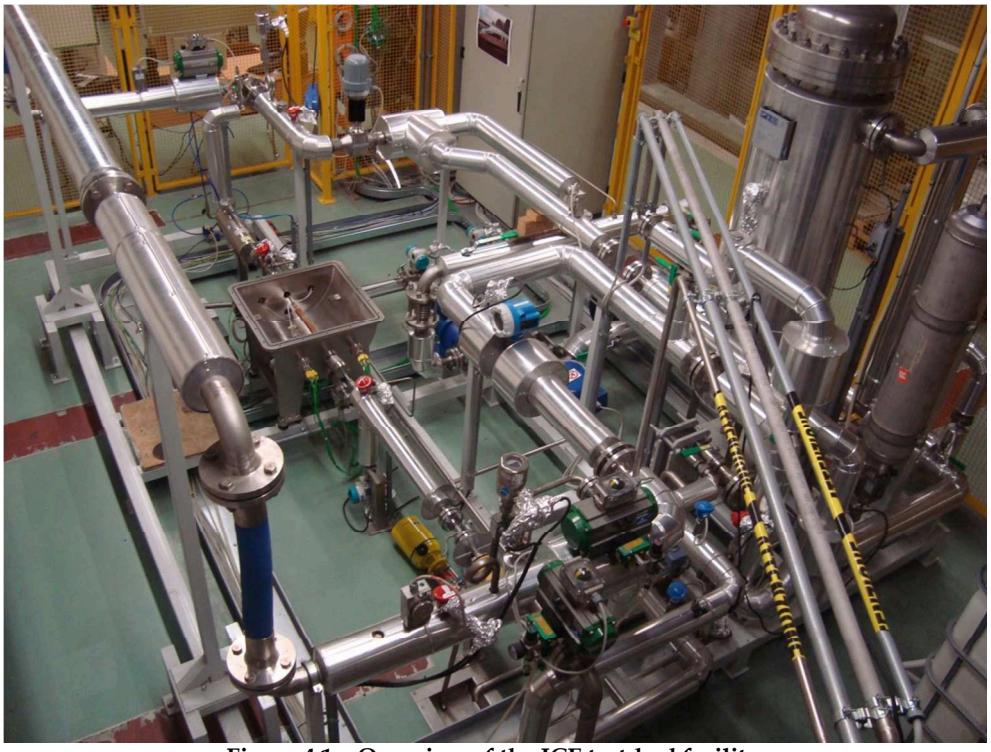

Figure 4.1 – Overview of the ICE test-bed facility.

The parts of the circuit equipped with the common services and the ultrapure water test section, where higher flow rates are needed, are connected with a DN50 circuit. The thermo-hydraulic test section is set up on a DN15 circuit.

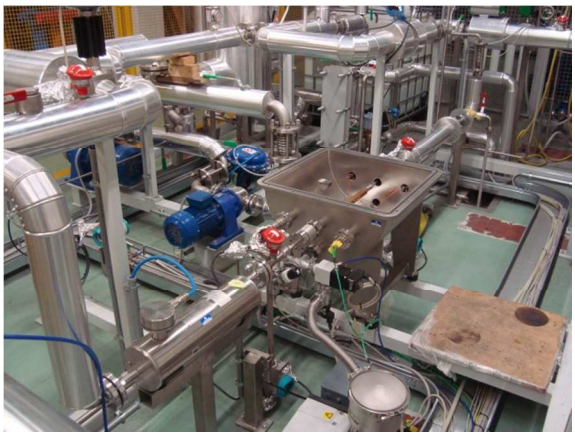

Figure 4.2 – Thermo-hydraulic test line.

Figure 4.3 – Thermo-electric test line.

Two different size circulating pumps are present in the test bed both driven by variable speed motors. In this way, a flow rate ranging from 100 to 8000 kg/h can be produced in the different test sections.
The circuit can be filled with normal water or with ultrapure water stored inside a dedicated electro polished stainless steel reservoir.

Figure 4.4 –P8 (left) and P2 (right) circulating pumps.

Figure 4.5 - Electro polished stainless steel reservoir and four purification modules for water deionization process.

A measuring conductivity cell is installed on the inlet pipe to measure the water conductivity. The fluid reservoir can be heated in order to supply the ultrapure water at different inlet temperatures up to 180 °C.
If needed, a plate heat exchanger fed by cold water can cool down, up to 12 kW, the circulating fluid exiting from the thermo-hydraulic branch to allow the control of inlet water temperature. The heat exchanger performance is controlled by a three way valve installed on the heat exchanger cold side.

Figure 4.6 - Water conductivity sensor head.

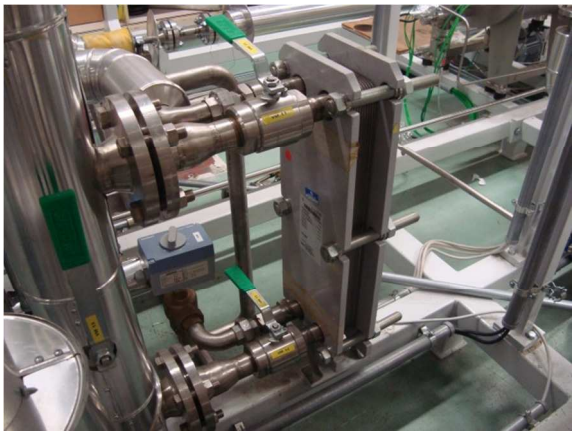

Figure 4.7 - Plate heat exchanger.

In reason of the maximum circuit working pressure (20 bar) and maximum test temperature (180°C) the experimental plant in equipped with safety components like valves, thermostats, pressure and flow switches.

In order to avoid fluid leakage in case of damage at electrical breaks, two fast pneumatic valves are provided to close the circuit in case of excessive water pressure drop.
A fast pneumatic opening valve and a bypass branch have been installed to avoid water hammer and to precisely control the flow rate but are currently out of service.

Figure 4.8 - Boiler (left), pressurizer (right) and safety aspiration gate (above).

4.2 Thermo- Hydraulic tests sections

The thermo-hydraulic test section has been conceived in order to perform thermo-fluid dynamics investigations on electrodeposited copper prototypes at conditions relevant for SPIDER, MITICA and future devices.
The test bed is designed to fulfil the following requirements and working parameters:

- the prototypes shall be tested in vacuum conditions (~0.5 Pa);
- different values of heat loads shall be applied to the prototypes by means of ceramic electrical heaters;
- the water temperature at the inlet sections shall be controllable and adjustable up to 180 °C;
- the mass flow rate at the inlet of test section shall be controllable and adjustable from 0.03 up to 1.5 kg/s;
- the water pressure shall be adjustable from atmospheric pressure up to 20 bar.

Electrical ceramic heaters are foreseen in the prototype test section to reproduce the heat loads deposited on the grid. These high performance electric heaters are made of aluminum nitride incorporating a thermally matched heating element and an embedded K-type thermocouple.

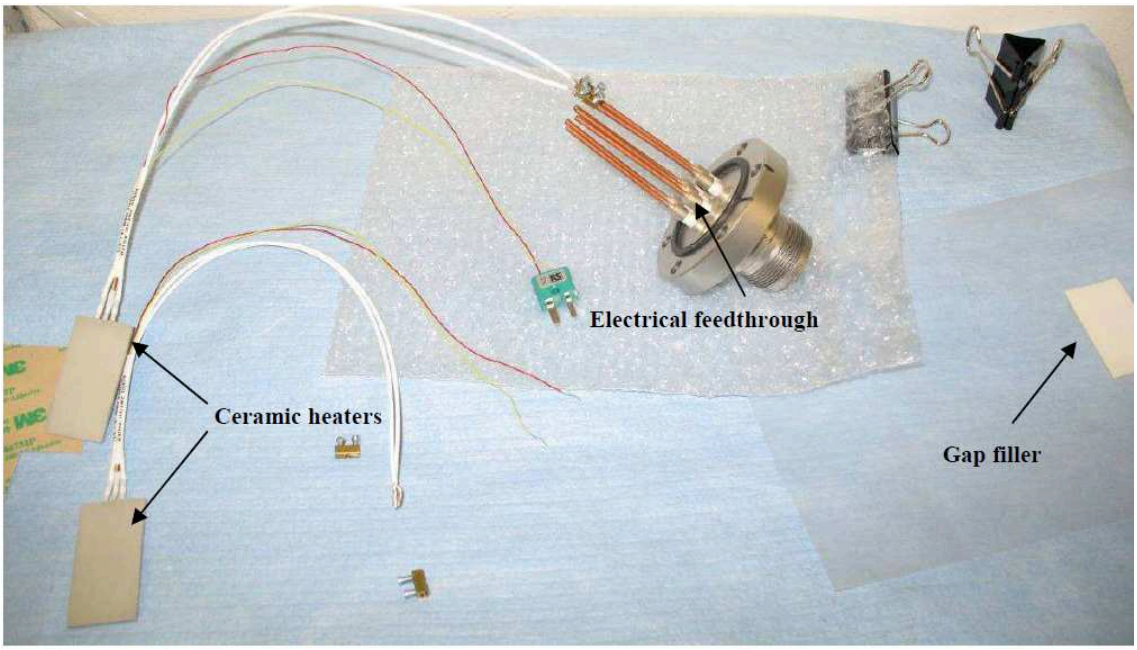

Figure 4.9 - Ceramic electrical heaters, electrical feedthrough and gap filler.

Each heater can apply a maximum power of 1222 W at 220 V and has dimensions of 50x25x2.5 mm, which corresponds to a maximum power density of 978 kW/m^2.
The maximum operating temperature for the heater is 400 °C. Two heaters are fixed along one cooling channel prototype, giving a maximum power of ~2.5 kW on a single channel.
Nevertheless, since during the heating process the temperature of the heater increases, also the electrical resistivity increases with an increasing factor of about 0.0025 K^{-1}. Thus, the power transferred to the load according to the Ohm's low decreases with the rising of the electrical resistance ($P=V^2/R$).
This fact lowers the maximum value of the heating power that can be applied to the SCPs. When the duty cycle is 100%, the heater temperature reaches about 250 °C and the corresponding heating power is about 750 W each.
Since the heat transfer investigations were supposed to be carried out under vacuum a specific stainless steel vacuum chamber is required. This chamber has overall dimensions of approximately 300 mm in diameter and 600 mm in length to house the prototypes. The vacuum chamber is equipped with water, electrical and thermocouple feedthroughs and an inspection window.
The vacuum is obtained by means of a rotary pump to achieve the 0.5 Pa comparable to the gas pressure surrounding the electrostatic grids in current fusion experiments.
The flow rates are measured by a high accuracy mass flow meter.

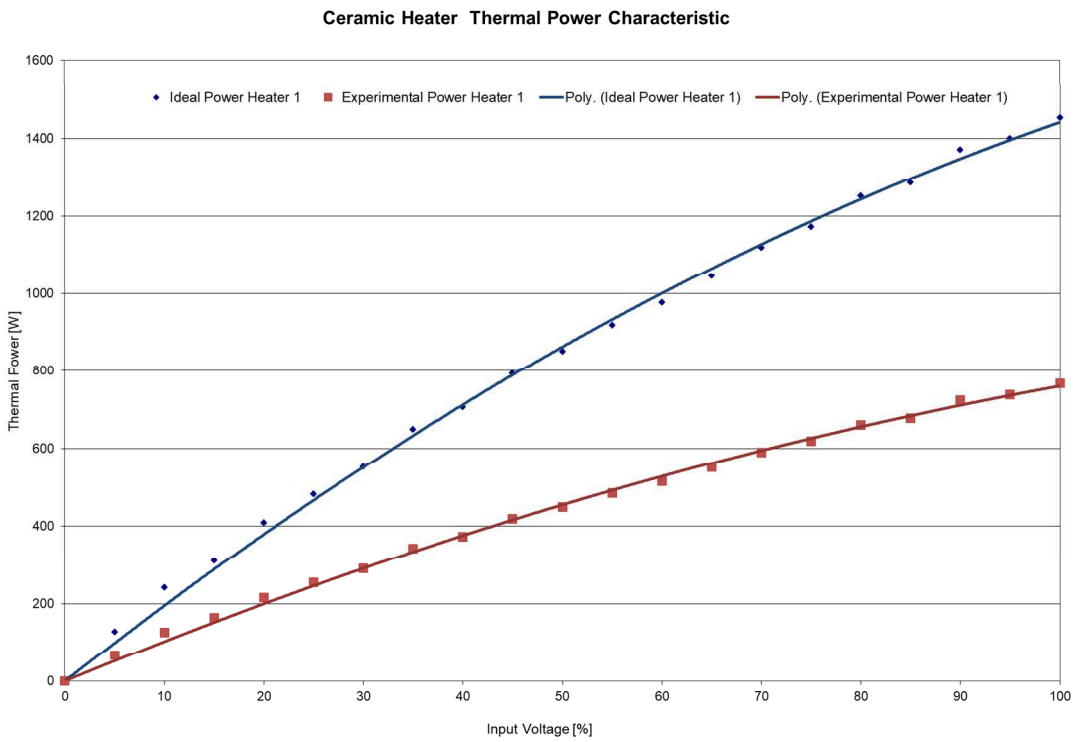

Figure 4.10 - Input voltage characteristic of Ceramic heater thermal power.

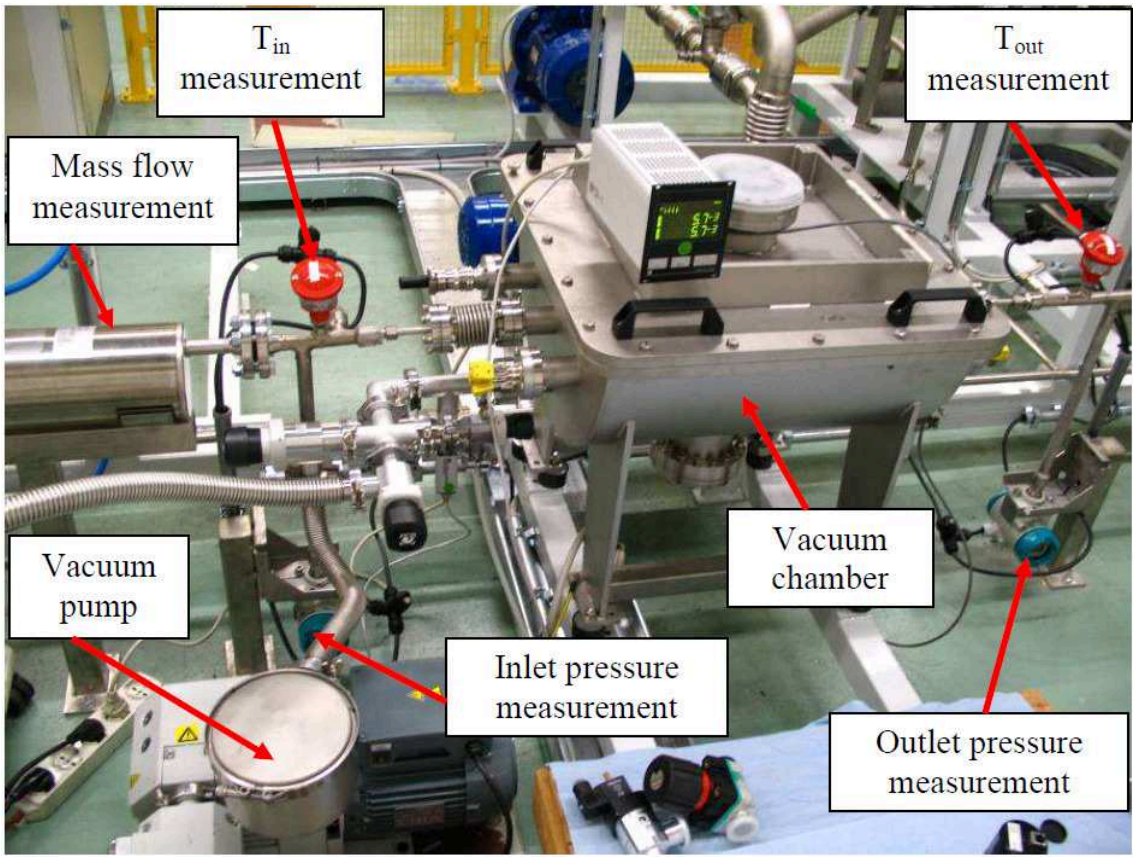

Figure 4.11 - Thermo-hydraulic test section components.

4.3 Sensors for plant control and experimental tests

The installed instrumentation which has been exploited during the execution of the thermo fluid-dynamic tests has the double purpose to keep under control important parameters for the correct and safe operation of the plant (such as temperature and pressure) and to be able to acquire all the thermo-hydraulic data in order to fully characterize the SCPs in terms of heat exchange and pressure loss.
The thermodynamic parameters that have been monitored during the experimental activity are:

- Temperature;
- Pressure;
- Mass flow rate;

As far as thermometric measurements are concerned, two resistance thermometers PT100 (Tin and Tout) are installed just at the inlet and at the outlet of the test section in order to measure the water temperature upstream and downstream the SCP.
In this way it is possible to measure the temperature increment due to the heat load applied through the ceramic heaters to the prototype. Each resistance thermometer is characterized by Class A precision according to IEC 751 with -200÷400 °C as operational range.
In order to be able to acquire the signals derived from the thermocouples be directly applied to the system a stand-alone acquisition system (34980A Multifunction Switch/Measure Unit by AGILENT) is provided and integrated with the data logging system. The device is characterized by 40 2-wire channels, 300 V, 1 A switch, 2 A carry current, 100 ch/s scanning, mix 2- or 4-wire configurations, built-in thermocouple reference junction, 4 current channels, latching armature relays, with relay counter. In the experimental activity configuration it is capable of 500 ms acquisition speed of 7 thermocouple channels.
For pressure measurements two kinds of instruments are installed: absolute/relative pressure transducers and differential pressure transducers. There are two water absolute pressure transducers by SIEMENS (APS1, APS2), two water relative pressure transducer by Endress+Hauser (APS3, APS4), two water differential pressure transducers by SIEMENS (DPS1 and DPS2), and one air pressure (APS5).
With DPS1, it is possible to measure the differential pressure between two points respectively upstream and downstream the vacuum chamber, so having a direct measurement of the pressure drop in that section.
With such measurement it is possible to determine the pressure drop inside the SCPs, once the plant idle losses have been accounted.
On the other hand DPS2 measures the pressure drop all through the plant, having the two water plugs just upstream and downstream the pumps.

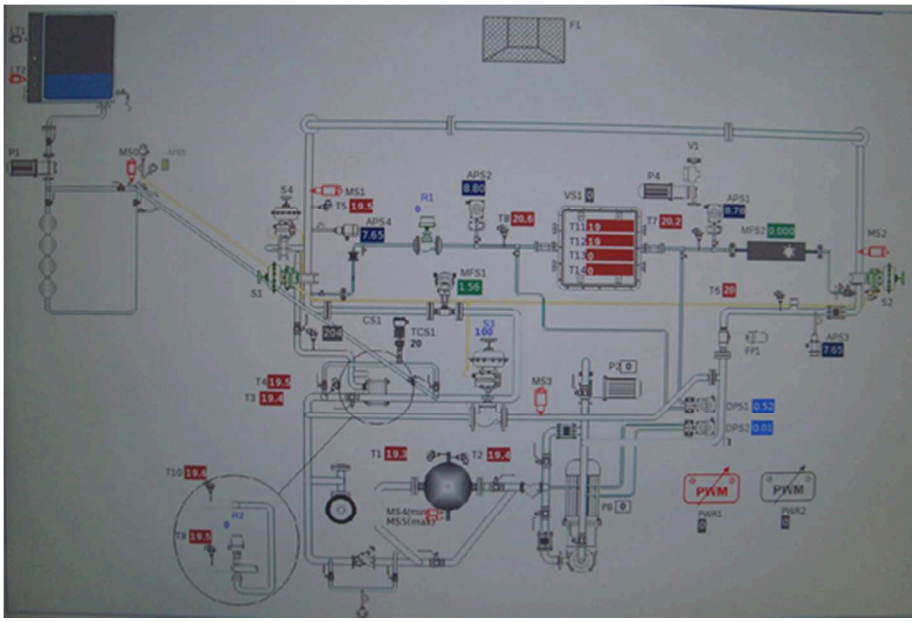

Figure 4.12 – Layout of the experimental plant with sensor location.

Two mass flow meters are installed: one Coriolis mass flow meter (MFS2 by SIEMENS) is located on the thermo-hydraulic DN15 branch upstream the test section and one vortex flow meter (MFS1 by Endress+Hauser) is installed just after the end connection between the thermo-hydraulic and ultrapure water test section. The first one allows a more precise measure at low mass flow rates, since it is based on a direct measure of the mass flow, whereas the second one measures the volume flow and the mass flow is calculated, but it can be used on a much wider flow range.
In reason of the experimental conditions to be performed the Coriolis mass flow meter signal has been the only one to be used for data post-processing.

4.4 ICE plant tests and commissioning

In order to experimentally determine the pressure drop through the SCPs, a differential and two absolute pressure transducers are installed (respectively DPS1, APS1 and APS2).
The water plugs for both the differential and absolute pressure transducer are located in the DN15 pipe just upstream and downstream the vacuum chamber. Once the SCPs are installed, the relative pressure measurements are referred to the entire branch between the two water plugs and not only to the prototypes.
In order to determine the pressure drop referred to the SCPs only, hydraulic calculations have been performed to provide a mass-flow dependence estimation of the losses through the stainless steel pipe between the water plugs of the pressure transducers and the connection between the SCP and the DN15 stainless steel pipe of the plant (connections made by means of Swagelok® fittings).

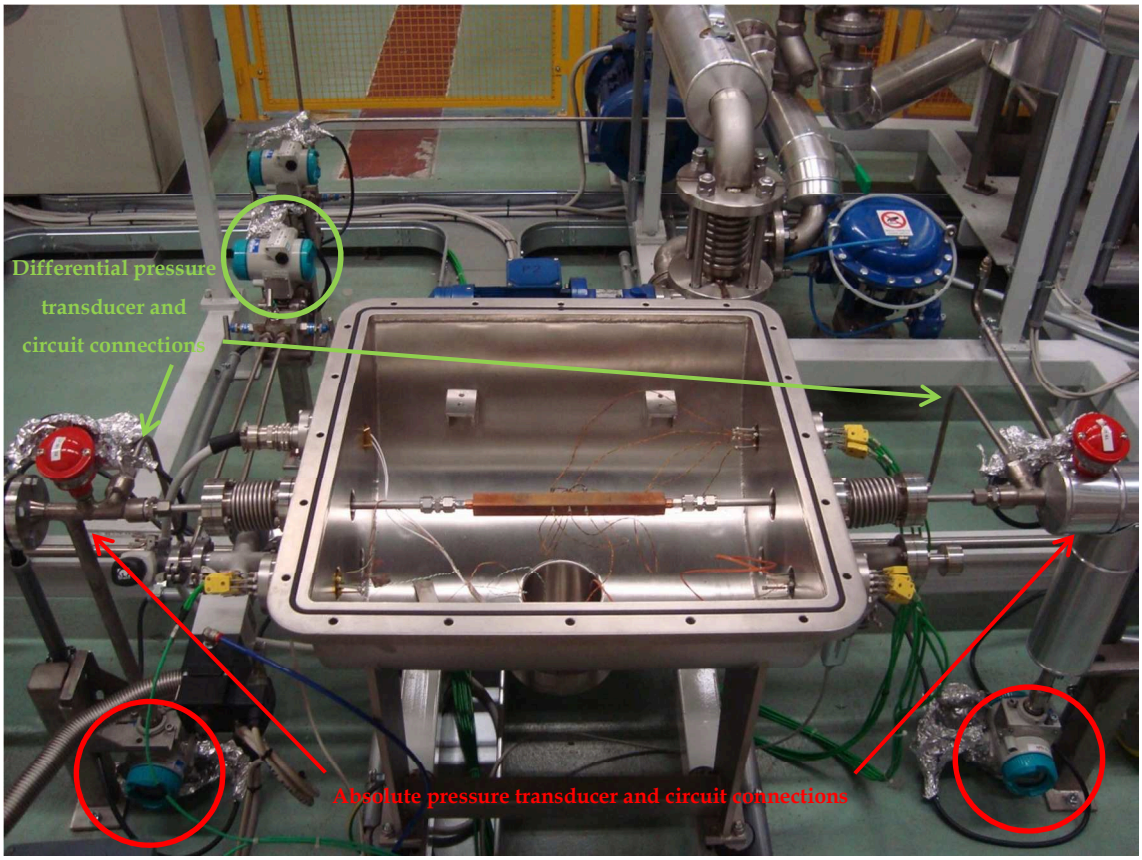

Figure 4.13 – Spatial disposition of the absolute and differential pressure transducers.

In order to characterize the pressure drop behaviour of the DN15 stainless steel branch between the two water plugs, a specific test has been carried out. A copper tube instead of the SCP has been connected to the stainless steel pipe with Swagelok® fittings.
Theoretical calculations have been performed in order to characterize the hydraulic behaviour of the copper tube in terms of pressure drop. The test has been carried out varying the flow rate in the overall operative range of P2 (0-100%) resulting into a mass flow spectrum up to a maximum of 0.588 kg/s.
Given the internal diameter of the copper tube (8 mm) and the temperature of the water, the water properties and the corresponding fluid velocities and Reynolds numbers have been calculated.
Since the all tests have been carried out with flow velocities corresponding to Re>2300 (transition zone in the Moody diagram), the friction factor f has been calculated with an iteratively resolution of the Colebrook-White equation.

$$\frac{1}{\sqrt{f}} = -2\log\left(\frac{2.51}{Re\sqrt{f}} + \frac{\varepsilon/d}{3.71}\right) \tag{4.1}$$

Then the Darcy-Welsbach equation has been used to calculate the pressure drop (Δp) in the copper tube:

$$\Delta p = f \cdot \frac{L}{D} \cdot \rho \frac{v^2}{2} \tag{4.2}$$

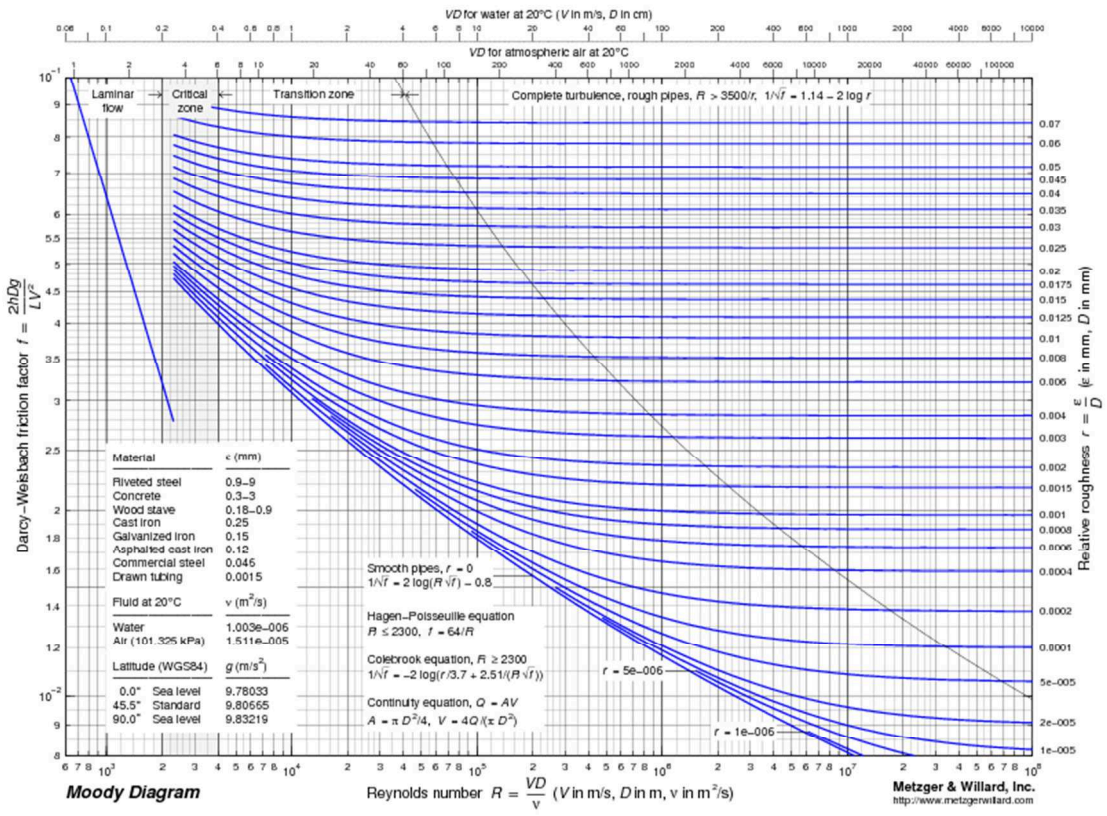

Figure 4.14 - Moody's diagram.

The characteristics of the copper tube and water properties used for calculations are summarized in Table 4.1.

Table 4.1 - Copper tube characteristics and water properties.

Copper Tube		Water properties	
Internal Diameter	$8 \cdot 10^{-3}$ [m]	Temperature	24 [°C]
Roughness	$2 \cdot 10^{-6}$ [m]	Pressure	10 [bar]
Relative Roughness	$2.5 \cdot 10^{-4}$	Density	997.706 [kg/m^3]
Length	0.3 [m]	Dynamic Viscosity	$9.1049 \cdot 10^{-4}$ [kg·m/s]

The different estimation provided by DPS1 and APS1-APS2 signals have been cross-checked and compared with the theoretical Δp of the copper tube in order to define the hydraulic losses of the stainless steel DN 15 pipe between the two water plugs of the differential and absolute pressure transducer.

The static conditions of the hydraulic circuit have been exploited in order to establish the zero correction between the two absolute pressure transducers.

The resulting plant characteristic curves are depicted in Figure 4.15 and show two important characteristics: the theoretical hydraulic losses are modeled with a better accuracy by the absolute pressure transducers rather than the differential one, in addition this last device saturates its measurements at 1.8 bar.

Such pressure upper limit signal could reveal a problem in the assessment of the thermofluid-dynamic performance of some SCPs since part of them are characterized by pressure drops estimations which attest even above such threshold.

As a matter of fact the idle losses associated to hydraulic circuit comprised between the pressure sensors have been modeled and compared with the measurement provided by differential and absolute transducers.
By knowing the plant contribution to the measured pressure drops during the test in the SCPs it has been possible to determine the effective Δp associated to the Single Channel Prototypes by subtracting the idle losses contribution to the probe measurements.

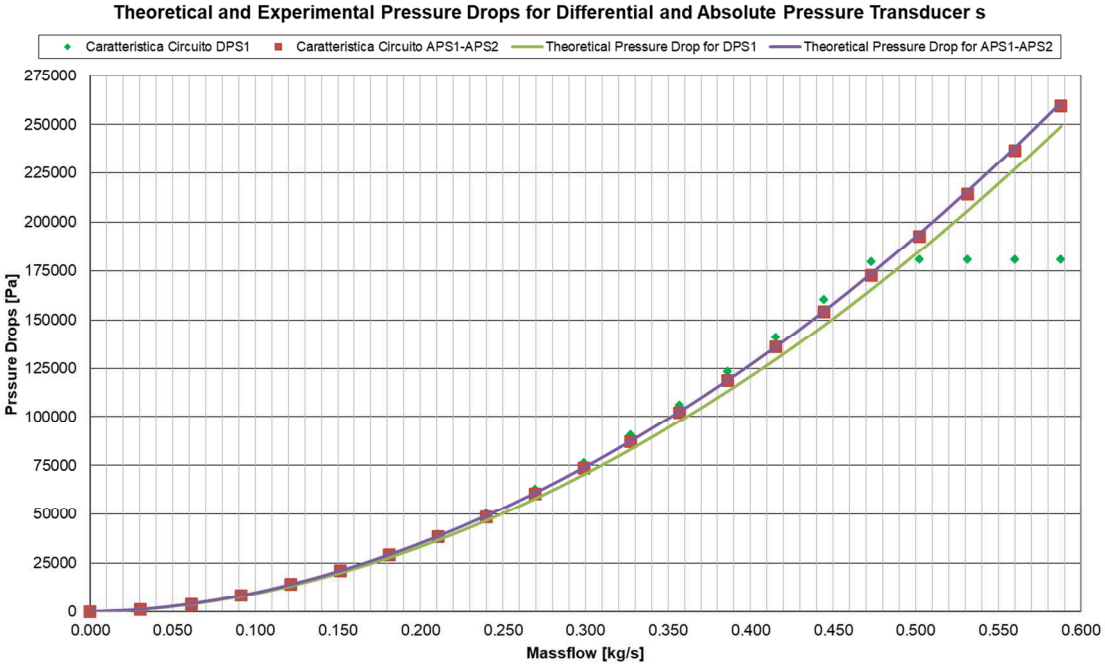

Figure 4.15 – Theoretical and experimental pressure drops for differential and absolute pressure transducers.

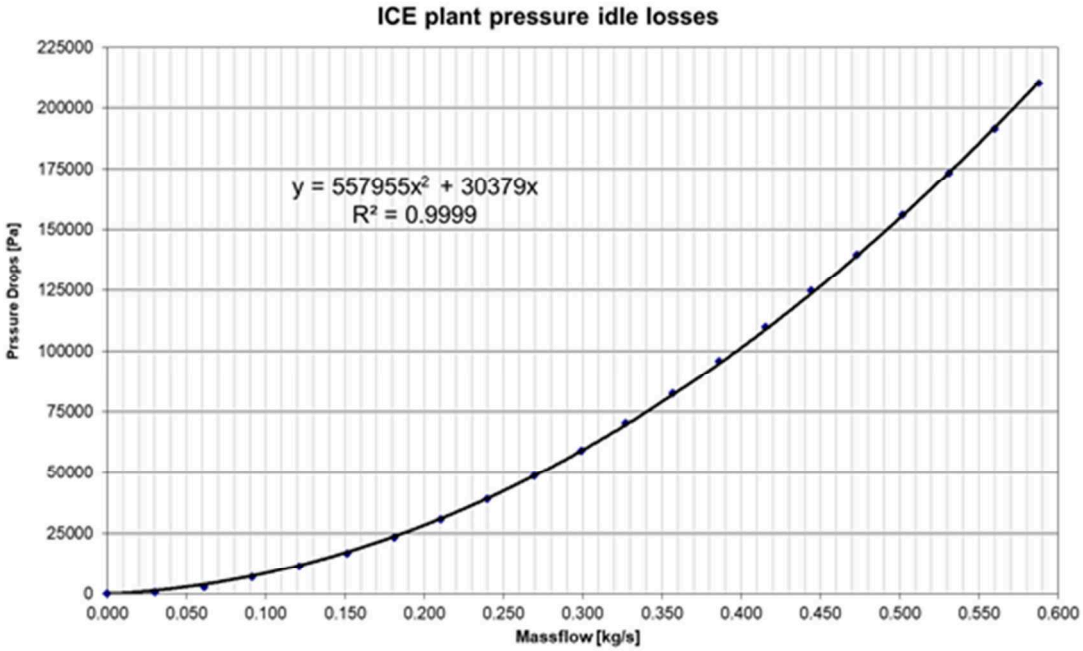

Figure 4.16 - ICE plant pressure idle losses with associated trend-line and characteristic equation.

4.5 Thermo-Hydraulics tests on the SCPs

Several thermo-hydraulic tests have been performed on the Single Channel Prototypes (SCPs). The main aims of the foreseen thermo-hydraulic tests are here listed.

1) Measurements of pressure drops through the measurements obtained by differential pressure sensors by varying coolant velocity;

2) Measurements of water and Cu temperatures and calculation cooling efficiency under different operational conditions.

All the different prototypes have been equipped with screw independent thermocouples in order to measure the temperatures in determined positions inside the copper domain. Calorimetric measurements are also performed by means of water flow rate measurements and temperature sensors at the inlet and outlet of the prototypes.
At first it has been thought to perform the thermofluid-dynamic test in stationary operations, evaluating the different temperature signals from the various thermocouples under different operative configurations in terms of heat loads provided by ceramic heaters and circulating mass flow rate.
Unfortunately a failure to the potentiometer regulating the input power to the two ceramic heaters occurred and it was no more possible to control and assess the heat flux provided by the devices to the different prototypes with an acceptable degree of accuracy nor to repair the device in a sufficiently short period able to guarantee the possibility to perform the prescribed experimental campaign..
A set of test in stationary regime has been performed but the relevant uncertainties affecting the experimental apparatus provided poorly correlated results.
On the contrary the evaluation of the cooling performances in transient operations gave the possibility to assess the heat exchange efficiency of the different samples with an acceptable degree of accuracy.
Before the test campaign, the copper surfaces of each prototype have been opportunely cleaned with acetone in order to remove all the greases traces.

4.6. Experimental plan

The experimental plan has been organized in order to collect all the information relevant to support and verify the SCPs design and to provide experimental data for actively cooled components in severe heat transfer conditions.
After the plant characterization, the SCPs have been tested in order to measure:

- the differential pressure between upstream and downstream of the prototypes as a function of the mass flow rate;

- a set of localized temperatures of the SCPs and the water temperature at the outlet of the prototypes during the heating process using ceramic electrical heaters;

The tests have then been followed by data post-processing in order to calculate:

- the actual pressure drops through the SCPs channel taking into account the plant characterization curve;

- the actual cooling efficiency of each SCP.

The details are reported in the following sections.

4.7. Pressure and Leak Tests

The most important aspect to be checked before starting the experimental test campaign is the vacuum tightness of the VTTJ connection and of the electrodeposited copper layer embedding the cooling channels.
Two tests have been carried out to detect possible leaks in the most delicate parts of the samples:

- Pressure test at high pressure with water at 25 bar;
- Vacuum He leak tests.

The tests have been performed in such order with the aim of inducing, during pressure tests, a tensile stress fields in the parts to be carefully investigated. In such conditions, if the galvanic operations have been characterized by off-nominal parameters, the electrodeposited copper could lose its tightness characteristics leading to formation of cracks which could either result in water leaks, if enough extended, or successive helium leakages during the helium tests.
In other to perform the pressure test, the samples have been filled with water pressurized at 25 bar minimum. Due to the elastic behaviour of water if the leak is too small to be visually detected, it would nevertheless result in a macroscopic loss of internal pressure. The different samples have remained under pressure test condition for 24 hours. The pressure tests have been performed in a cage to avoid risks of damages and accidents in the case of break of electrodeposited parts.
In the vacuum leak test, considering the small dimensions of the volume to be set under vacuum conditions (i.e. the cooling channels), the samples have been directly connected to the leak detector. Helium is sprayed with a helium gun to deposit a very thin layer on the electrodeposited parts and the leak value is recorded by the leak detector. Leaks can be evaluated by measuring the helium gas presence in comparison with the reference value, once the system has reached the steady state condition.
The concentrated leaks detected shall be smaller than $1 \cdot 10^{-9}$ mbar l/s in He.

Figure 4.17 - Pump with tank reservoir for pressure tests.

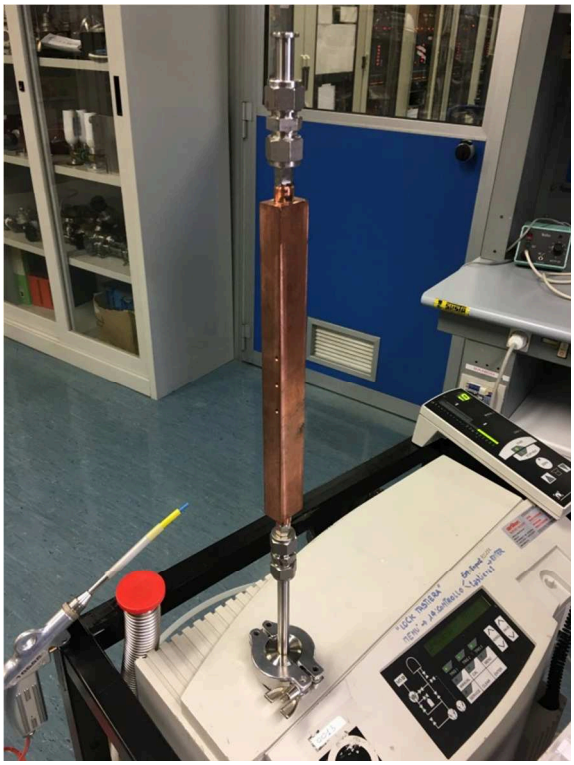

Figure 4.18 - Vacuum Helium leak test operations.

Table 4.2 – Pressure tests overview.

SCP Design	Initial internal water pressure	Final internal water pressure
Baffle Channel	25 bar	25 bar
Criss-Cross Channel	26 bar	26 bar
Diverted Channel	27 bar	27 bar
Duned Channel	25 bar	25 bar
Duned Drag Channel	26 bar	26 bar
NICE Channel	27 bar	27 bar
NICE Turbotron Channel	28 bar	28 bar
NICE Tilt Turbotron Channel	26 bar	26 bar
NICE Upgrade	27 bar	27 bar
Single Straight Channel	25 bar	3 bar

Table 4.3 – Vacuum He leak test overview.

SCP Design	Vacuum test measured value at prototype	Operating pressure
Baffle Channel	$1.4 \cdot 10^{-10}$ mbar·l/s	0.220 mbar
Criss-Cross Channel	$< 1 \cdot 10^{-11}$ mbar·l/s	0.340 mbar
Diverted Channel	$4.3 \cdot 10^{-11}$ mbar·l/s	0.019 mbar
Duned Channel	$2.6 \cdot 10^{-8}$ mbar·l/s	0.012 mbar
Duned Drag Channel	$1.8 \cdot 10^{-10}$ mbar·l/s	0.320 mbar
NICE Channel	$3.2 \cdot 10^{-10}$ mbar·l/s	0.243 mbar
NICE Turbotron Channel	$1.4 \cdot 10^{-10}$ mbar·l/s	0.290 mbar
NICE Tilt Turbotron Channel	$1.1 \cdot 10^{-10}$ mbar·l/s	0.022 mbar
NICE Upgrade	$2.6 \cdot 10^{-10}$ mbar·l/s	0.02 mbar
Single Straight Channel	Out of range	76 mbar

As depicted in Table 4.2, it can be noted that the Single Straight Channel failed the pressure test. The water internal pressure created indeed an opening on the electrodeposited surface covering the cooling channel which could be detected eye-naked.
As far as the helium leak test are concerned, see Table 4.3, the different SCP demonstrated the vacuum tight resistance of the electrodeposited layers having all the leak flow rate measurement below the sufficient acceptable limit for Swagelock ® technology (i.e. 10^{-9} mbar·l/s). Just the Duned Channel recorded higher values but that was due to the Helium saturation of the device consequently to the test of the Single Straight Channel prototype.
As a matter of fact all the prototypes have undergone to thermo-hydraulic tests with exception of the Single Straight Channel which was sent to the laboratory to be recovered, trying to fill the opening with araldite bi-component glue.

4.8. SCPs pressure drop characterization

All tests have been performed with ambient temperature water (~20 °C). The mass flow rate has been varied in the overall range which can be realized through the exploitation of P2 volumetric pump with the motor speed varying from 0% to 90% of the maximum nominal one (with a 5% step between the configuration and the subsequent one). This has been performed by equipping the volumetric pump with a variable frequency driver.
The nominal foreseen flow rate and test flow rates values (minimum and maximum) for each type of prototype are shown in Table 4.4.
It is worth noting that the NICE Tilt Turbotron Channel is the only design that is not symmetric with respect to the central vertical axis. As a matter of fact it has the possibility to be tested in a duplex configuration, the former with the ribs draining water from the heated surface toward the bulk region of the channel and the latter with the ribs feeding water to the heated surface from the bulk region of the channel.

Table 4.4 - SCP nominal and test flow rate ranges.

SCP Design	Nominal Flow rate [kg/s]	Minimum Flow rate [kg/s]	Maximum Flow rate [kg/s]
Baffle Channel	0.29375	0.030	0.498
Criss-Cross Channel	0.29375	0.030	0.497
Diverted Channel	0.29375	0.029	0.496
Duned Channel	0.29375	0.028	0.503
Duned Drag Channel	0.29375	0.030	0.505
NICE Channel	0.29375	0.031	0.565
NICE Turbotron Channel	0.29375	0.030	0.470
NICE Tilt Turbotron Channel (draining water ribs)	0.29375	0.029	0.501
NICE Tilt Turbotron Channel (feeding water ribs)	0.29375	0.025	0.500
NICE Upgrade	0.29375	0.029	0.467
Single Straight Channel	0.29375	[-]	[-]

In Figure 4.19-4.28 the pressure drops through the different SCPs are respectively. Each plot has been obtained by measuring the pressure drop for increasing water flow rates and by subtracting the contribution to the losses given by the plant idle losses as described in Section 4.4. The second order zero crossing fitting curves have been also calculated.

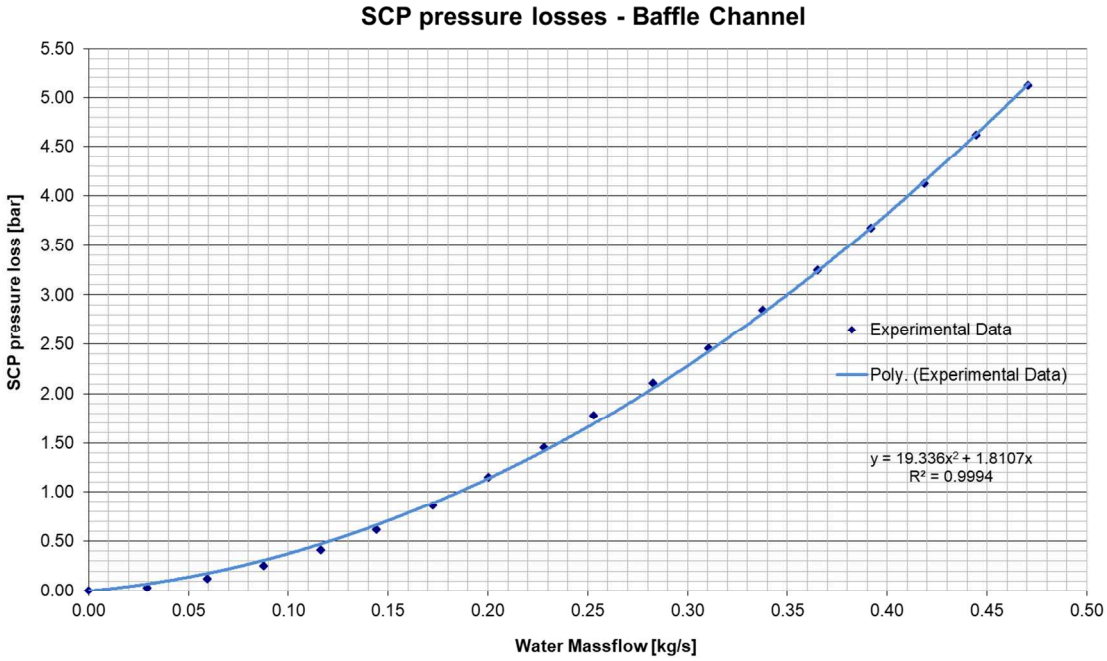

Figure 4.19 - Baffle channel hydraulic characteristic.

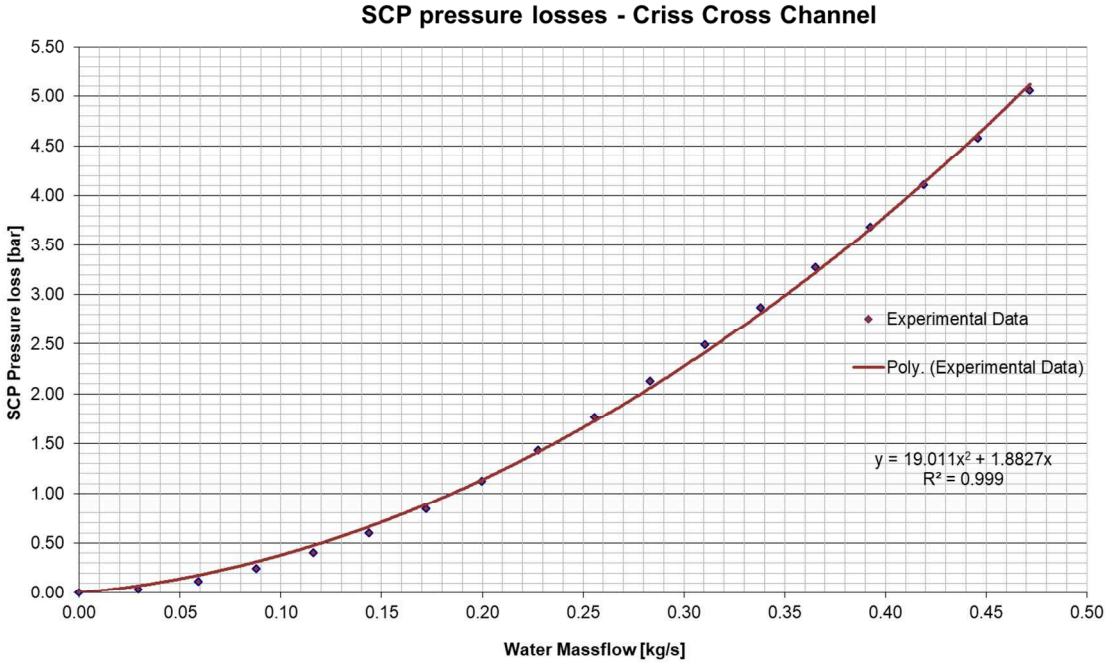

Figure 4.20 - Criss-Cross channel hydraulic characteristic.

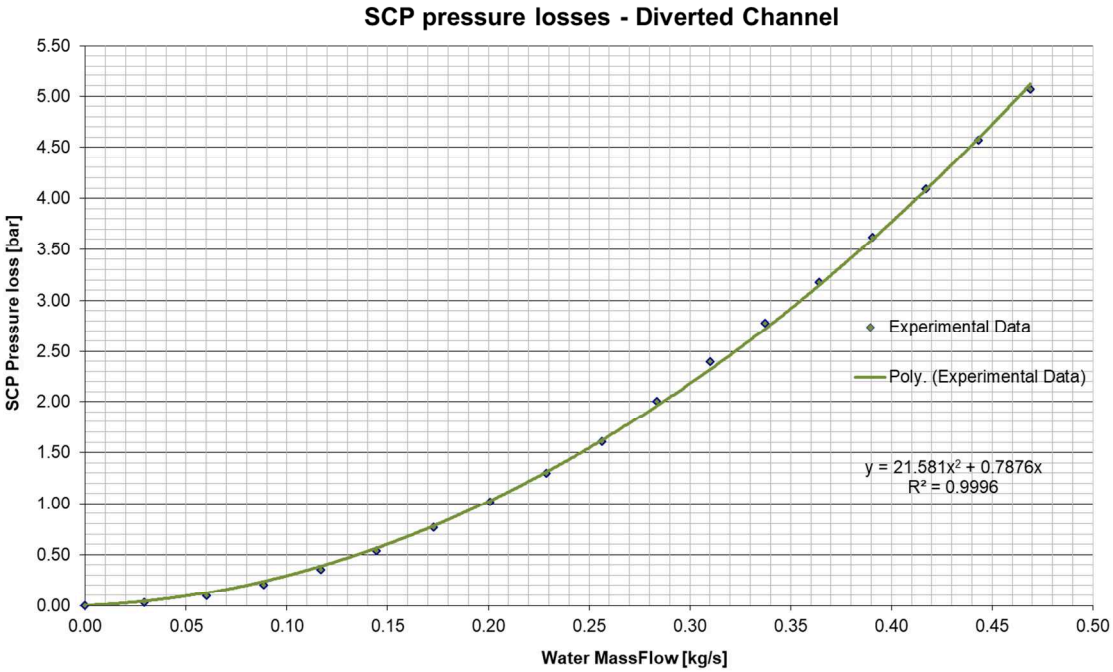

Figure 4.21 - Diverted channel hydraulic characteristic.

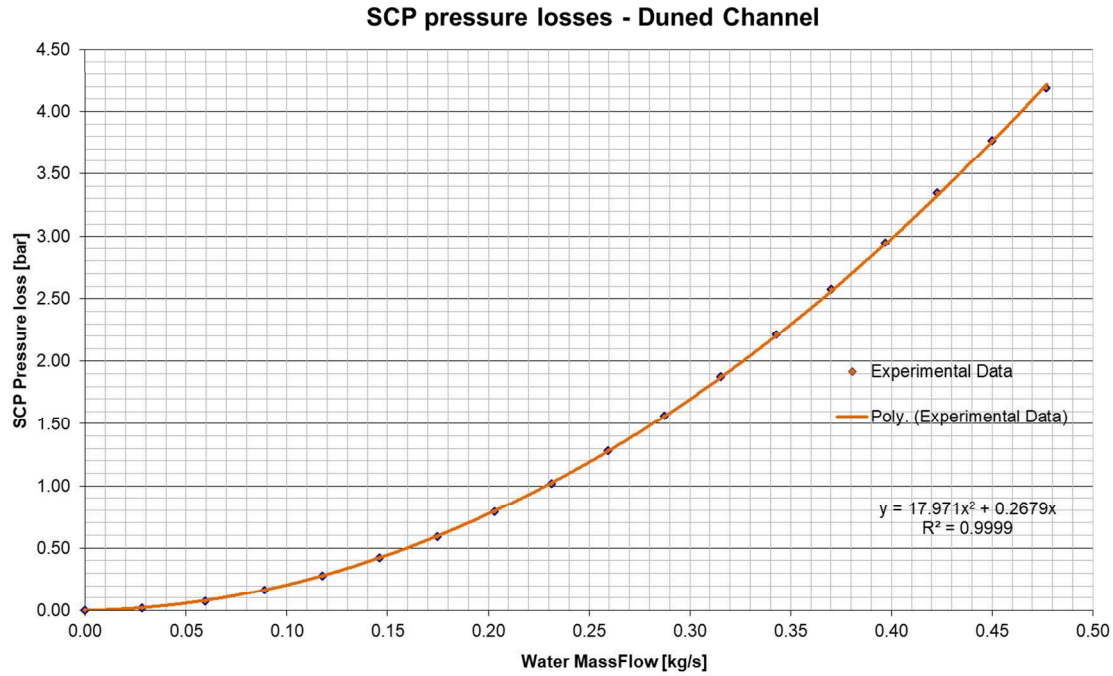

Figure 4.22 - Duned channel hydraulic characteristic.

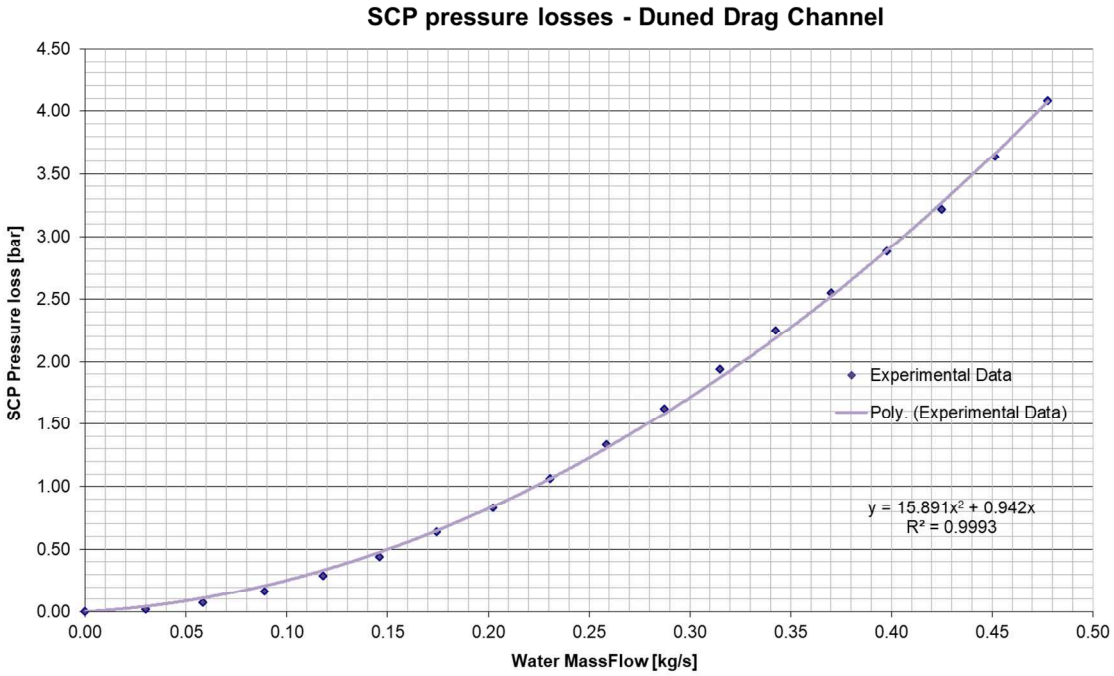

Figure 4.23 - Duned Drag channel hydraulic characteristic.

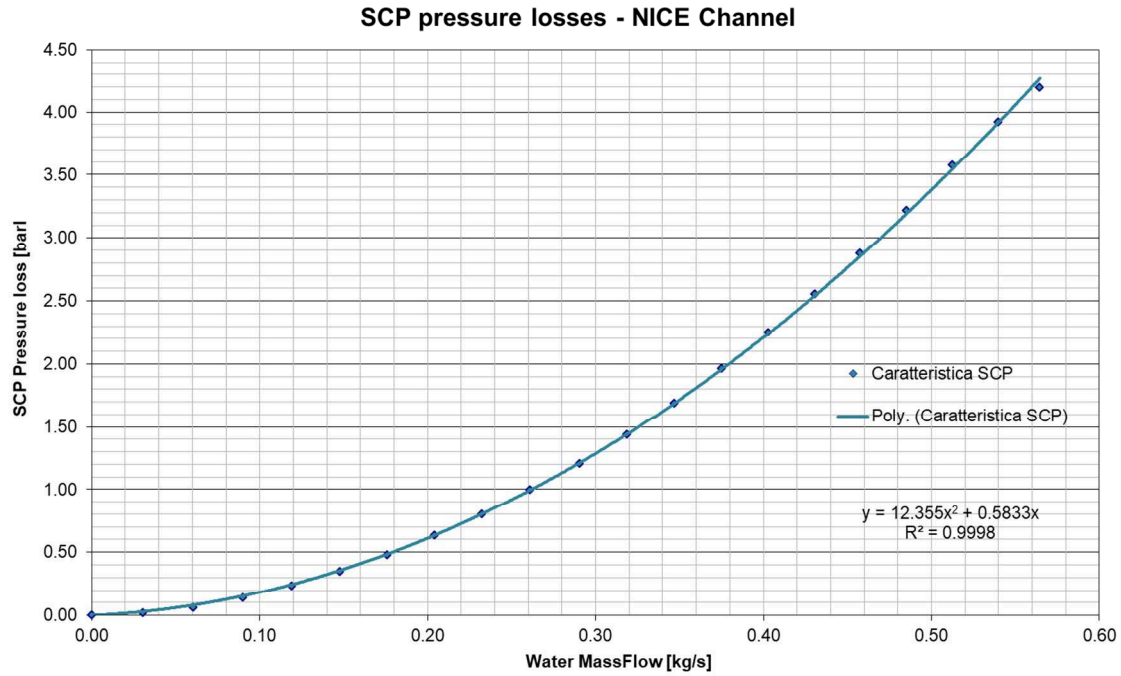

Figure 4.24 - NICE channel hydraulic characteristic.

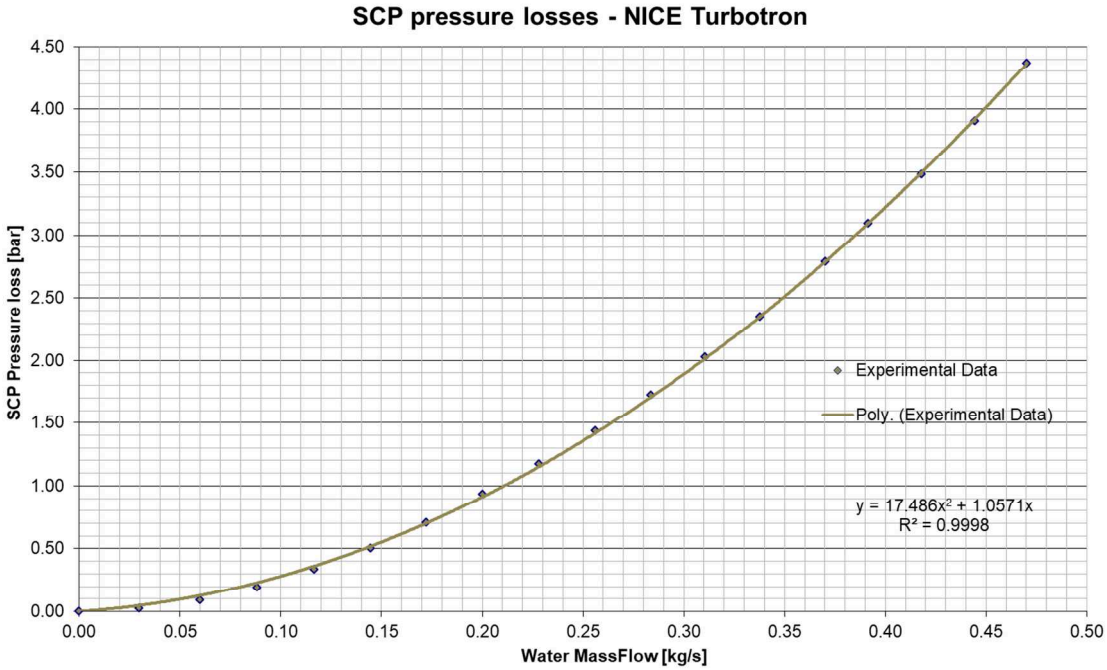

Figure 4.25 - NICE Turbotron hydraulic characteristic.

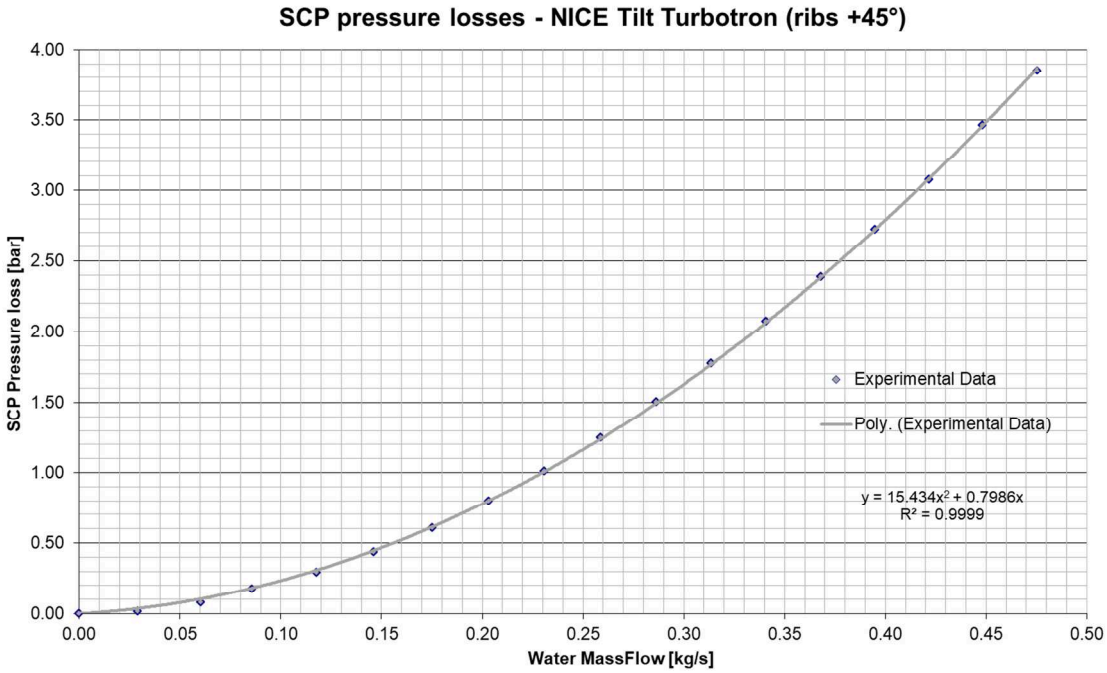

Figure 4.26 - NICE Tilt Turbotron (ribs +45°) hydraulic characteristic.

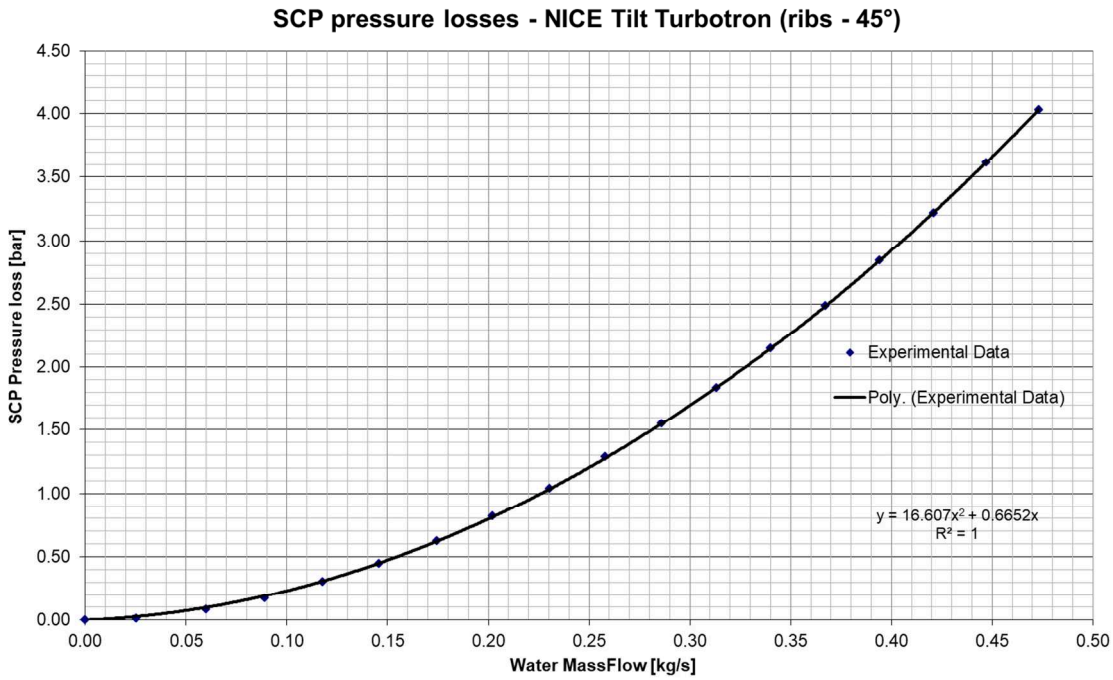

Figure 4.27 - NICE Tilt Turbotron (ribs -45°) hydraulic characteristic.

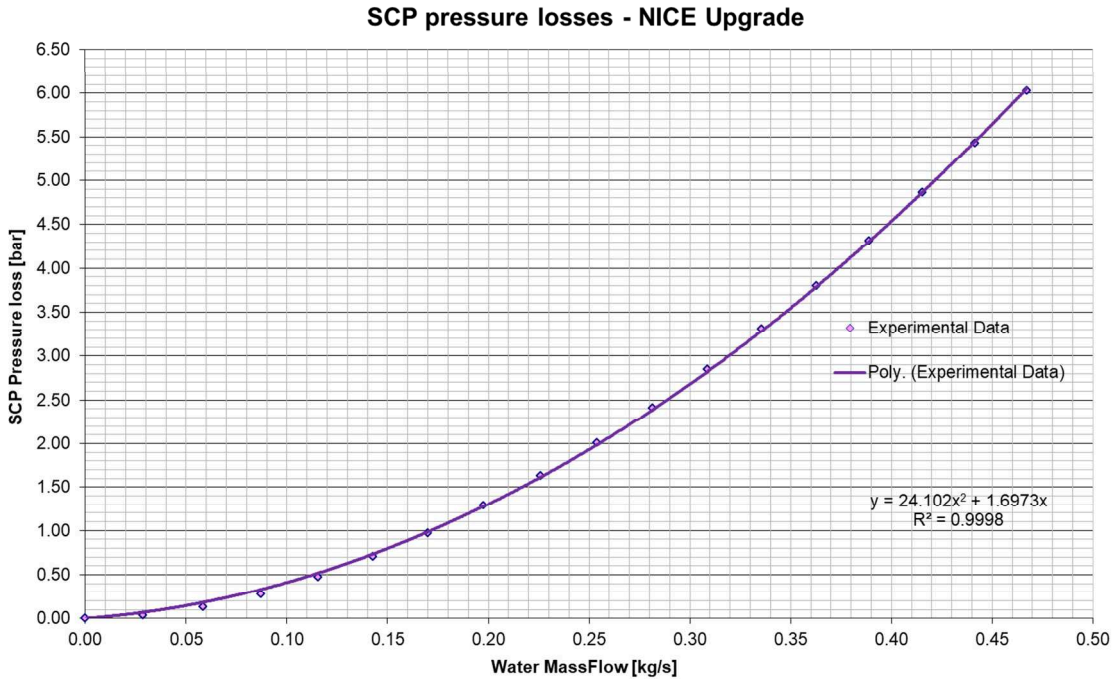

Figure 4.28 - NICE Upgrade hydraulic characteristic.

An additional set of fluid-dynamic tests have been performed with the objective of attesting the circulating water mass flow as close as possible to the nominal one (0.29375 kg/s) in order to have a direct evaluation of the SCP pressure drop without any exploiting any interpolating operation. The obtained results are listed in Table 4.5.

Table 4.5 - SCP pressure drop in nominal mass flow operations.

SCP Design	Water Mass Flow [kg/s]	Pressure Drop [bar]
Baffle Channel	0.29388	2.058
Criss-Cross Channel	0.29385	2.123
Diverted Channel	0.29378	2.032
Duned Channel	0.29375	1.532
Duned Drag Channel	0.29404	1.584
NICE Channel	0.29378	1.236
NICE Turbotron Channel	0.29358	1.555
NICE Tilt Turbotron Channel (draining water ribs)	0.29390	1.619
NICE Tilt Turbotron Channel (feeding water ribs)	0.29378	1.732
NICE Upgrade	0.29344	2.562
Single Straight Channel	[-]	[-]

4.9. SCPs cooling efficiency test

The variable parameters of the heat transfer tests have been the mass flow rate and the initial temperature of the SCPs.
The heating process has been performed by means of two rectangular ceramic heaters (made of Al-N) connected to a power regulation system based on a Pulse Width Modulation (PWM) system. Although this system allowed a precise regulation of the thermal power transferred to the prototypes, it was not possible to control and regulate the power directly from the control system by varying the duty cycle due to a failure of the device.
Being not capable of measuring through the control system the instantaneous power transferred to the load by averaging the direct integration of the product between voltage and current parameters over the period T, it was not possible to exploit the ceramic heater ohmic power as input parameter during the execution of the thermofluid-dynamic tests.
The two ceramic heaters have been positioned on the surface of the prototypes as shown in Figure 4.29.

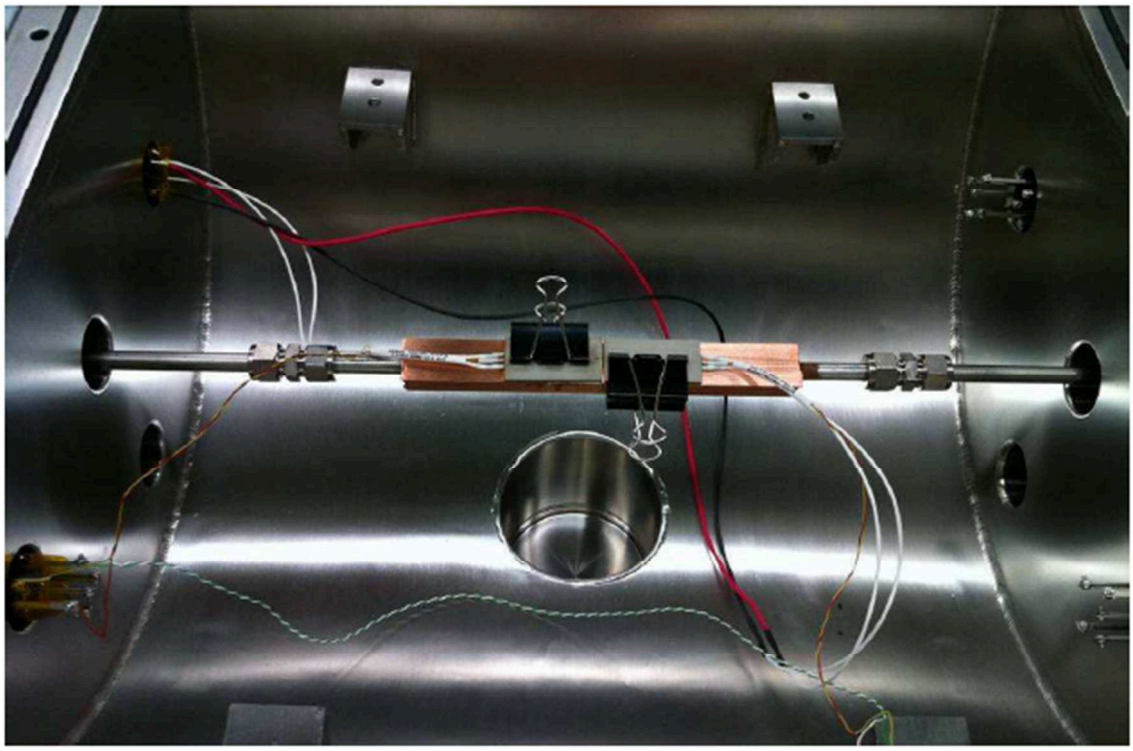

Figure 4.29 - SCP mounted in the thermo-hydraulic test section, inside the vacuum chamber.

In order to guarantee a uniform contact between the ceramic heaters and the copper surface, high conductivity Boron Nitride filled Silicone elastomer gap filler interface sheets (thermal conductivity 6 W/mK and thickness of 0.5 mm) have been interposed between the heaters and the prototype surface.
In this way the heat transfer process is more uniform and the thermal contact resistance is considerably lower, as confirmed by experimental measures with and without the gap filler.
Nevertheless, due to the fragility of the ceramic heater the contact pressure has been conveniently limited to 30 kPa given by the metal clip. Furthermore, the clip is made of a thin elastic metal sheet and has a very small contact area with the heater, so it has a relatively high thermal resistance and then very little power is transferred to the inferior surface of the SCP.
The experimental test have been performed with a two steps approach: at first the ceramic heaters were turned on while no mass flow was induced in the cooling channel.
In this stagnant water configuration the temperature raised pretty fast since no adequate heat sink was provided to the realized thermodynamic system. When all the different thermocouples signals overcome the 180°C the heaters were turned off, subsequently removed from the SCP surface in order to avoid any inertial effect of the ceramic elements. Immediately after the removal of such devices the volumetric pump was turned on at the proper motor frequency realizing the sought nominal mass flow in the different SCP.

Each cooling phase has been recorded by means of the six thermocouples inserted in the prototypes till the extinguishment of the thermal transient phase. Figure 4.30 depicts the different SCPs thermal transient overlapping them one on to the others.

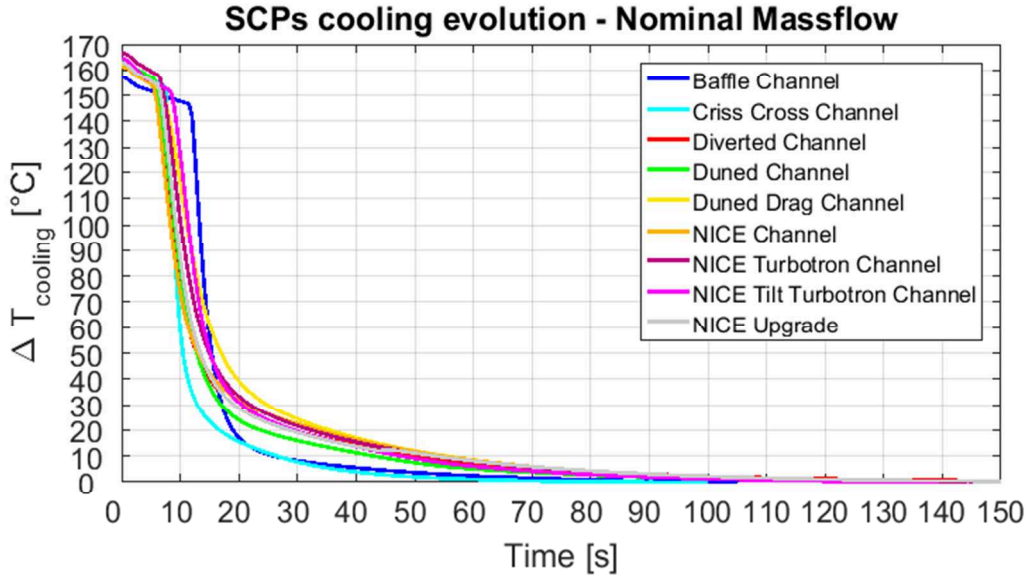

Figure 4.30 - SCP cooling evolution at nominal mass flow operations.

During the initial phases of the transient (approximatively in the first 10 seconds) the cooling phase is determined by the natural convective phenomena imposed by the surrounding environment. The different tests could not be executed in vacuum in reason of the need of removing the ceramic elements from the copper heated surface in order to extinguish any inertial phenomenon imposed by the heaters.
Successively all the different curves evolves with an exponential trend in reason of the instauration of the heat sink provided by the force convection phenomena inside the cooling channel as a result of starting the volumetric pump.

4.9.1. Equivalent electrical circuit

Exploiting the electrical analogy the thermocouple can be seen as the node depicted in Figure 4.31 with an incoming flux (provided by the ceramic heaters) and two sinks for the flux disposition (i.e. the actively cooling channels and the outer environment through natural convection).
With a broader approach the transient operations of the actively cooled thermodynamic system can be translated through a lumped parameter approximation into the simplified circuit depicted in Figure 4.32.

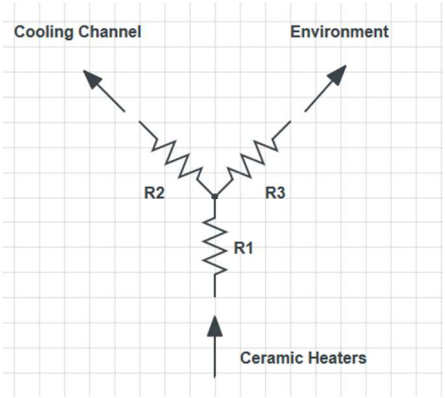

Figure 4.31 - Electrical modelization of thermocouple node.

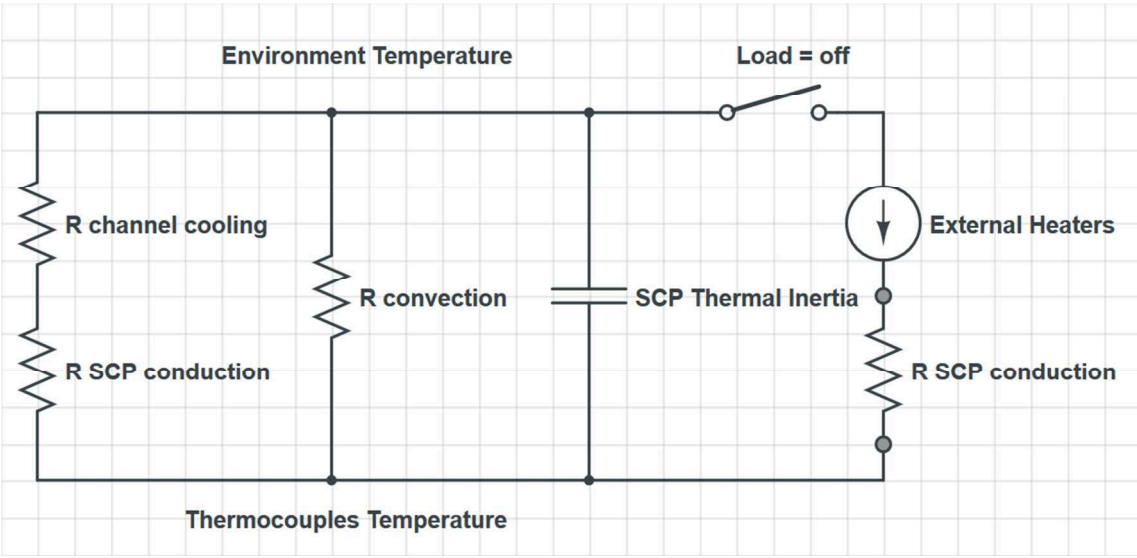

Figure 4.32 - Lumped parameter electrical circuit modelization of the thermodynamic system.

The resolution of the dynamic of present circuit provides a direct correspondence with the thermodynamic system, with the following correspondences:

Voltage (V)	⟶	Temperature (T)
Current (I)	⟶	Thermal Power (Φ)
Electrical Resistance (R_{el})	⟶	Thermal Resistance (R_{th})
Capacity (C)	⟶	Thermal Capacity (m·c)
Current Generator (A)	⟶	External Load (P_{ext})
Electrical Charge (q)	⟶	Thermal Energy (Q)

A switch is inserted in the equivalent model, discriminating the time interval during the application of the heat load (pulse on) where it is set in closed position and the time after the removal of source (pulse off) where it is set in open position.
The last configuration is the one of interest for present application. During the cooling phase P_{ext} is indeed switched off and the accumulated thermal energy during the heating phase is exhausted by the coolant and the external environment until the final equilibrium state is reached.

It is worth noting that the inferior wire electrical potential corresponds to the temperature measurements provided from the different thermocouples. This measurement is lower than the one coming from the surface where the heaters are located in reason of the $R_{SCP,conduction}$ resistance insisting between the heaters and the thermocouples themselves. On the contrary the superior wire electrical potential corresponds to the temperature of the surrounding environment and of the water at the bulk of the cooling channels.
As a consequence of the characteristics of the ICE hydraulic circuit, the coolant water can be considered at constant temperature equal to the one of the external environment along the all duration of the cooling process.
The heat flux by thermal radiation can be neglected since much smaller than the ones disposed by convection to the coolant and conduction through the samples.
The governing equations for the different component of the electrical circuit are listed in Table 4.6.

Table 4.6 - Governing equation in thermodynamic and electric approach.

	Thermal Equation	Electrical Equation
Electrical Capacitor	$Q = mc\,\Delta T$	$q = C\Delta V$
Current Generator		
SCP Conduction Resistor	$\Phi = k_{th,copper}\,\frac{A}{s}\,\Delta T$	$\Delta V = RI$
Convection Resistor	$\Phi = h_{wall} A \Delta T$	$\Delta V = RI$
Channel Cooling Resistor	$\Phi = \left(h_{wall} + \frac{k_{th,water}}{s}\right) A\Delta T$	$\Delta V = RI$

k_{th} is the thermal conductivity, A and s are the characteristic section area and thickness for the thermal conduction process while h_{wall} is the liminar convective heat transfer coefficient at the interface between two different media domains.
Taking into consideration the different orders of magnitude of the standard liminar convective heat transfer coefficient in single phase forced convection (~50'000 $W/m^2°C$) and in natural advective phenomena (~5 $W/m^2°C$), the characteristic time of the two processes it can be easily observed that the $R_{convection}$ resistor can be neglected when the two heat disposal process are running simultaneously.
During the "pulse off" and actively cooling condition of the prototype the system can be described by the Kirchhoff equation applied with the utilizer convention to the loop containing the capacitor and the resistors describing the thermal fluxes exchanged through the forced convection mechanism.

$$\frac{Q\,(t)}{mc} + \Phi(t)\,R_{th,eq} = 0 \tag{4.3}$$

The thermal power Φ can be indeed written as the temporal derivative of the thermal energy $Q\,(t)$ turning the equation into a differential one.

$$\frac{Q\ (t)}{mc} + \frac{\mathrm{dQ(t)}}{dt} R_{th,eq} = 0 \tag{4.4}$$

$$\frac{\mathrm{dQ(t)}}{Q\ (t)} = -\frac{dt}{mcR_{th,eq}} \tag{4.5}$$

The temporal evolution of the thermal energy stored in the SCP during the cooling process can be written as:

$$Q\ (t) = Q_o e^{-\frac{t}{mcR_{th,eq}}} \tag{4.6}$$

$$Q\ (t) = Q_o e^{-\frac{t}{\tau}} \tag{4.7}$$

Where τ is the characteristic time of the cooling process and corresponding to:

$$\tau = mcR_{th,eq} \tag{4.8}$$

With the given assumptions of neglecting $R_{convection}$ and $R_{SCP\ conduction}$ or considering them as fix parameters among the different SCP tests together with copper mass and heat capacity it is possible to obtain from such analysis a first evaluation of the thermal cooling conductance of the different cooling channel designs.
Before starting with comparing the different characteristic time it is therefore necessary to verify the different copper mass constituting the various SCPs.

Table 4.7 – SCP mass estimations.

SCP Design	SCP Mass [g]	SCP cooling module mass [g]
Baffle Channel	671.5	251.2
Criss-Cross Channel	677.6	257.2
Diverted Channel	677.9	257.5
Duned Channel	680.1	259.8
Duned Drag Channel	672.1	251.8
NICE Channel	681.6	261.3
NICE Turbotron Channel	683.0	262.7
NICE Tilt Turbotron Channel	684.1	263.7
NICE Upgrade	680.0	259.7
Single Straight Channel	694.8	274.5

The different prototypes are characterized by a very limited deviation in mass properties (23.26 g from the most massive one, the Single straight Channel and the least massive one, the Baffle Channel).
Nevertheless it is convenient to evaluate if this absolute mass difference considering the overall prototype domain would lead to a higher localized higher deviation in the region where the thermocouples are applied. If this was the case the deviations in the

estimation of the characteristic cooling time among the different prototype could be affected by higher dependence from the mass parameter. Taking into consideration the region where the thermocouples are applied (i.e. the 80 mm central cooling modules) it can be calculated that the former mass absolute difference produces a relative deviation from the two prototypes in the order of 9.26%.
Excluding the Single Straight Channel, the maximum relative deviation in terms of mass between the remaining prototypes is further reduced to 4.98% leading to the possibility of assuming the SCP copper mass as a constant for the different prototypes.
In order to proceed with the evaluation of the characteristic cooling time for the different SCP designs the thermal signal coming from the different thermocouples have been scaled into a double logarithmic scale, leading to the possibility to perform a linear fit through the data points. The resulting angular coefficient of the straight line provides a direct estimation of τ.

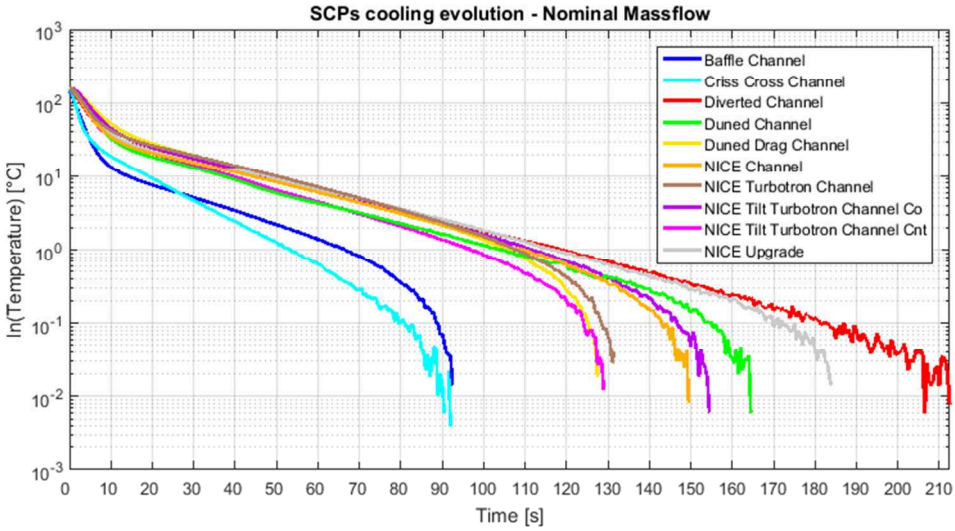

Figure 4.33 - SCP cooling evolution at nominal mass flow operations (logarithmic scale).

It can be noted that the actively cooling mechanism can be distinguished in two different phases. The former characterized by a fast evolution (~10 s) with a very fast decrease of copper temperature and the latter features a much slower evolution (> 60 s) where the temperature of the SCP, recorded by the thermocouples, decrease much slower as saturation of the thermal process has been reached.
As a matter of fact the proper time interval for the evaluation of the cooling efficiency of the different design is the former one.
Figure 4.35-4.40 depicts the different signals recorded by the six thermocouples during the first 10 seconds of cooling at the nominal mass flow rate. The thermal probes are labelled according the configuration illustrated in Figure 4.34.

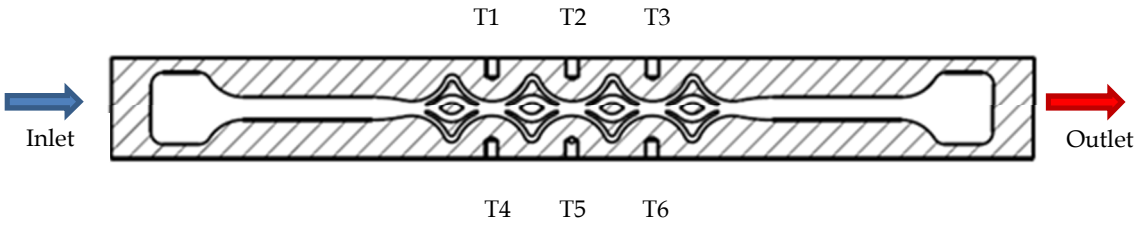

Figure 4.34 – Schematic representation of the positioning of the six thermocouples.

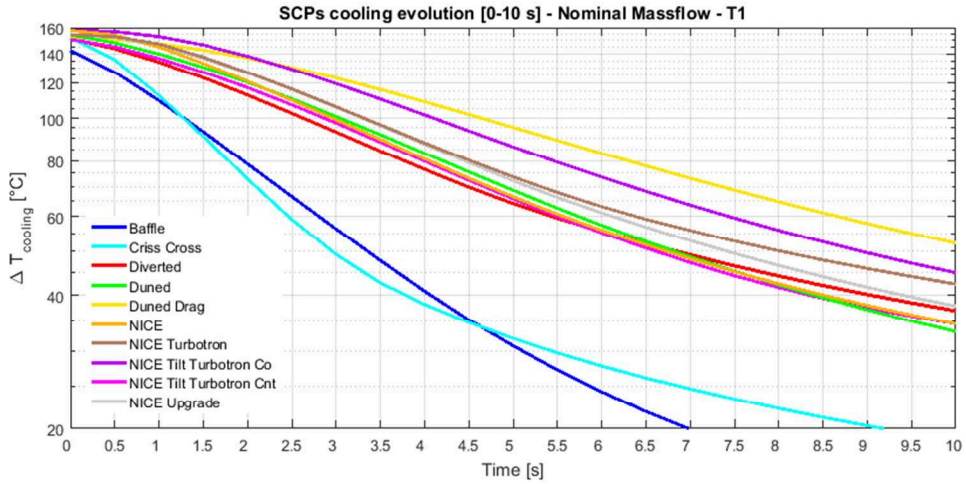

Figure 4.35 – Cooling evolution recorded by thermocouple 1 for the different SCPs.

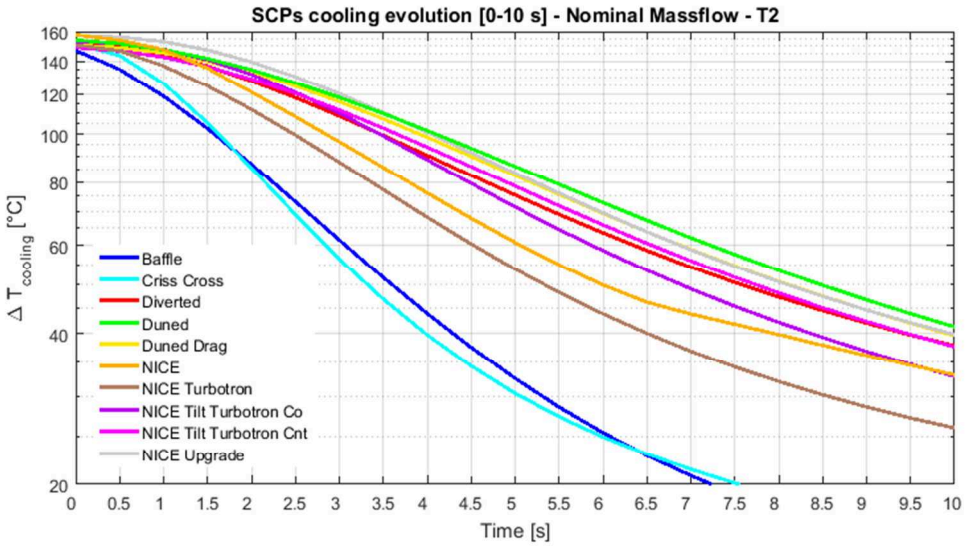

Figure 4.36 – Cooling evolution recorded by thermocouple 2 for the different SCPs.

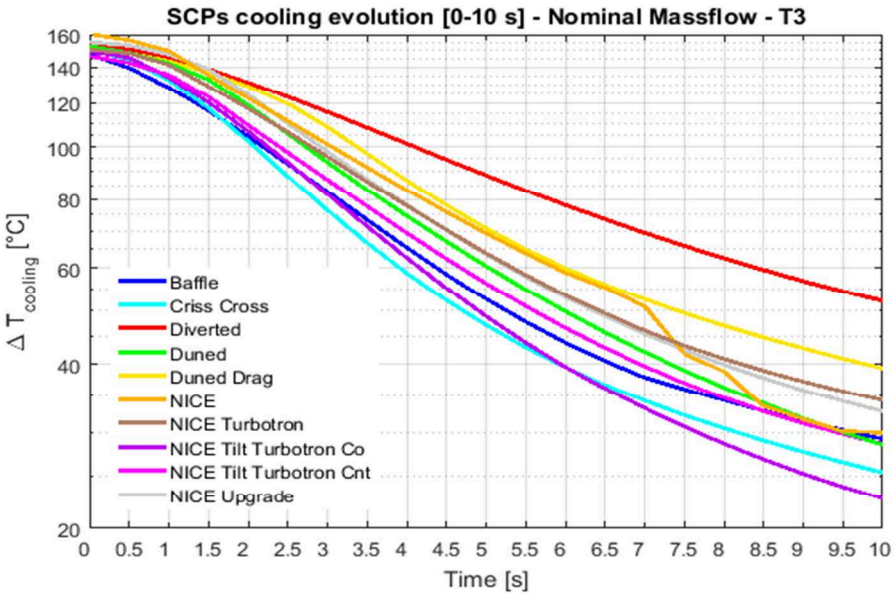

Figure 4.37 – Cooling evolution recorded by thermocouple 3 for the different SCPs.

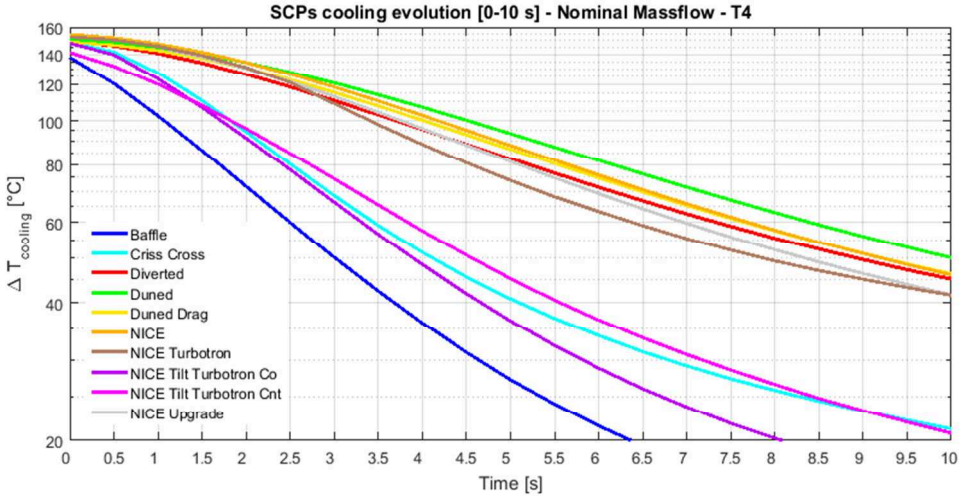

Figure 4.38 - Cooling evolution recorded by thermocouple 4 for the different SCPs.

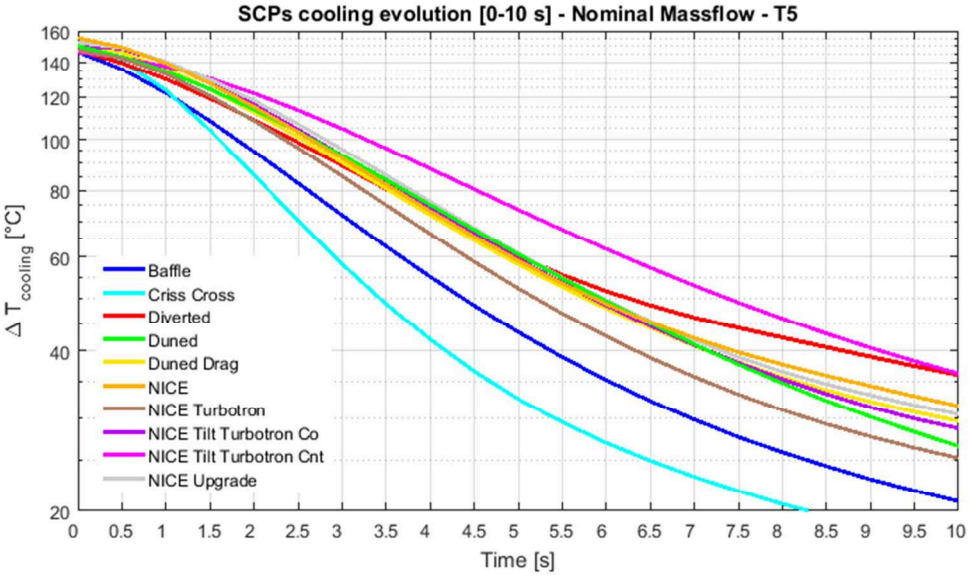

Figure 4.39 - Cooling evolution recorded by thermocouple 5 for the different SCPs.

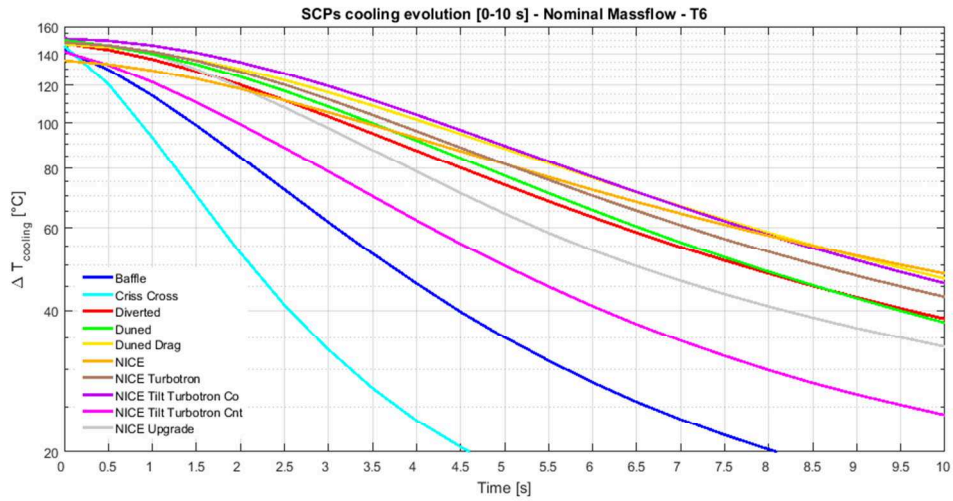

Figure 4.40 - Cooling evolution recorded by thermocouple 6 for the different SCPs.

The linear fitting has been performed in the most suitable range (but with a minimum duration of 3 s) of for each thermocouple in the in the different SCP. The characteristic time resulting from the data analysis are listed in Table 4.8.

Table 4.8 – Cooling characteristic time for the different SCPs.

SCP Design	T1	T2	T3	T4	T5	T6
Baffle Channel	3.115 s	3.024 s	4.390 s	2.909 s	3.791 s	3.279 s
Criss-Cross Channel	2.428 s	2.544 s	3.623 s	3.263 s	2.727 s	1.897 s
Diverted Channel	5.400 s	5.546 s	7.770 s	7.052 s	5.179 s	6.394 s
Duned Channel	5.311 s	6.361 s	4.634 s	8.097 s	4.907 s	6.154 s
Duned Drag Channel	8.098 s	5.952 s	5.336 s	7.008 s	4.746 s	7.305 s
NICE Channel	5.028 s	4.382 s	5.322 s	7.364 s	4.726 s	8.319 s
NICE Turbotron Channel	5.543 s	4.125 s	5.112 s	5.565 s	4.225 s	6.583 s
NICE Tilt Turbotron Channel Co.	6.274 s	4.708 s	3.834 s	3.224 s	4.527 s	6.887 s
NICE Tilt Turbotron Channel Cnt.	5.176 s	5.767 s	4.513 s	4.016 s	5.928 s	4.468 s
NICE Upgrade	5.333 s	5.540 s	4.721 s	6.369 s	4.552 s	4.983 s
Single Straight Channel	N.D.	N.D.	N.D.	N.D.	N.D.	N.D.

In principle the various thermocouples installed one SCP should not detect relevant difference in term of characteristic times due to the symmetry of the cooling modules and to the fact that the water fluid-dynamic regime is so high that the variation of property of the fluid along the flow could be neglected.
Nevertheless a quite large spread of the result is noticeable. That could be ascribed to the fact that the different tests were executed in temperature control configuration and not heat flux one. Being the spatial distribution and temporal evolution of the thermal flux provided by the heaters unknown it could have been verified the possibility that at the time where the ceramic devices were turned off the thermal fluxes flowing in the copper matrix of the different SCPs could deviated from a steady state configuration, hence perturbing the local cooling characteristic time.

Despite such shortcoming it is however possible to verify that the Baffle and Criss-Cross design demonstrate a far higher cooling performance capability with respect to all the others channel prototypes.
It is worth noting that such consideration do not necessarily state the other design realize this difference in performance even in the accelerating grid setup due to the different boundary conditions in term of heat flux, both topologically and in terms of amplitude.

4.10. Modelling and Validation

In this paragraph the numerical models used to benchmark the experimental results are described. Unfortunately the unexpected experimental condition encountered and the impossibility of exploiting the Single Straight Channel prototype led to the impossibility of extend the validation process beyond to the thermal-fluid dynamic tests and to compare the specific experimental set of experimental results with suitable analytical model proposed by the literature.
As a matter of fact it has been possible to validate the codes just for the fluid-dynamic tests providing a limited set of adopted parameters and assumptions to be to verified in view of the nominal design to be performed in next full scale experiments.
Numerical analyses have been performed in ANSYS Workbench environment exploiting the Computational Fluid Dynamics (CFD) with CFX solver.

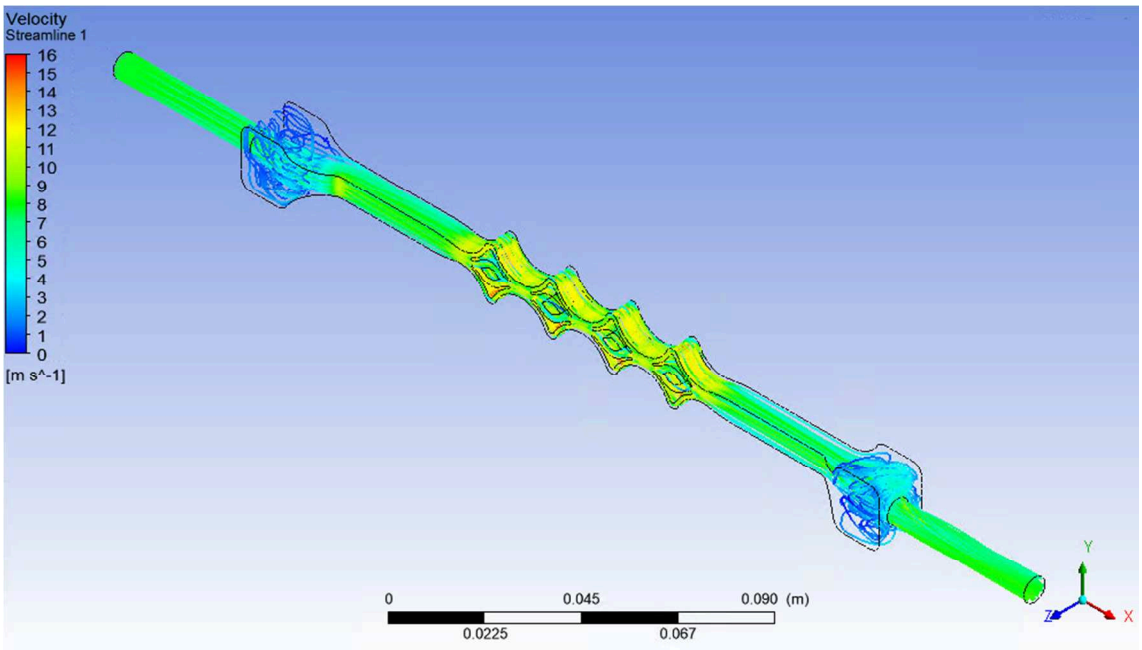

Figure 4.41 - Baffle Channel SCP pressure drop model: streamlines.

Within this solver both RANS (Reynolds Average Navier Stokes) and RSM (Reynolds Stress Models) fluid models have been exploited building for each one a suitable and

coherent parameters setup [21]. The fluid models which have been considered inside this benchmarking analysis are the following:

- K-ε;	-K-ε RNG;	- K-ε (EARMS);	- K-Ω;
- SST;	- BSL;	- BSL EARSM;	- BSL Reynolds Stress;
- SSG Reynolds Stress;	- QI Reynolds Stress;	- Ω Reynolds Stress;	- LRR Reynolds Stress;

- Eddy Viscosity Transport Equation;

In present CFD models only the fluid domain is reconstructed, since there is no heat exchange to be modeled. The main input parameter in this set of analyses are the water mass flow set to the nominal one (0.29375 kg/s), the channel wall roughness (1.6 μm) and the water inlet temperature (20°C) on the other hand the output results derived from the simulations are the pressure drop calculated as the difference between the average total pressure at inlet and outlet and the velocity field produced in the cooling channels. Typical post-processing graphical outputs are shown in Figure 4.42-4.43

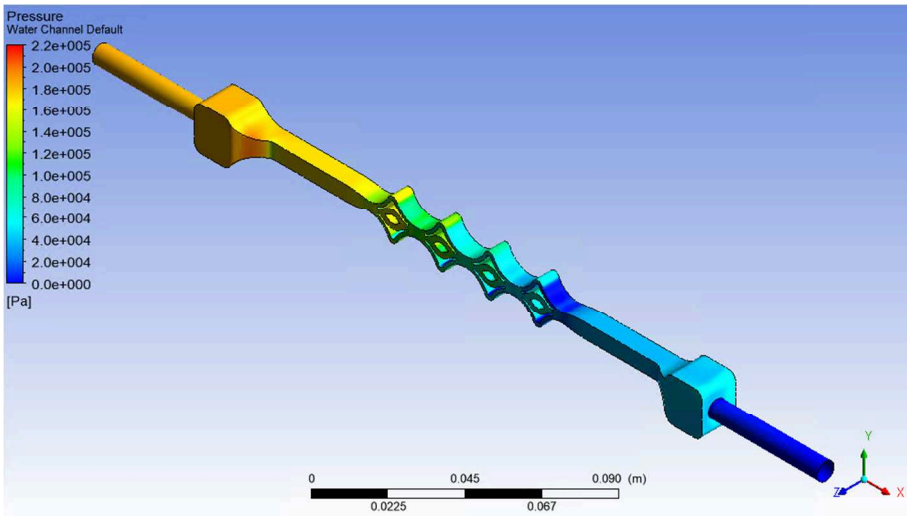

Figure 4.42 - Baffle Channel SCP pressure drop model: pressure drops.

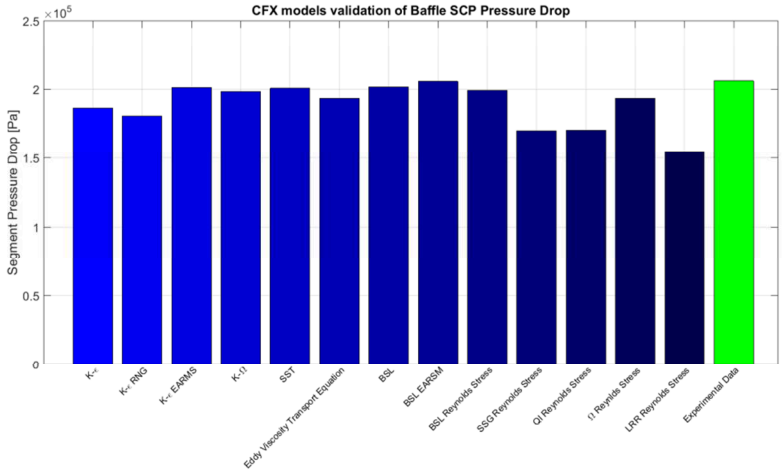

Figure 4.43 - Baffle SCP Pressure Drop validation.

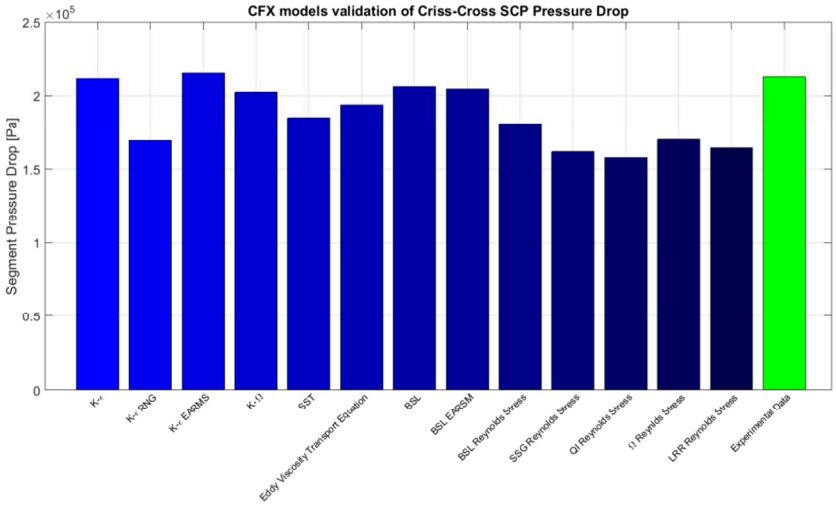

Figure 4.44 - Criss-Cross SCP Pressure Drop validation.

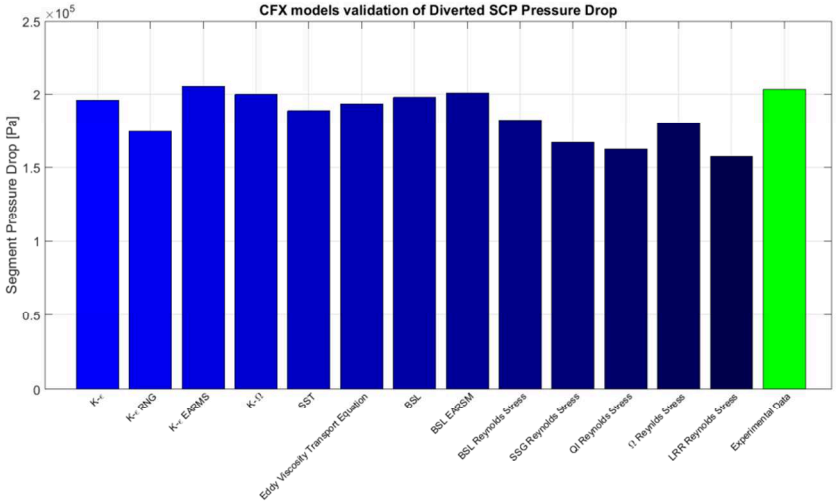

Figure 4.45 - Diverted SCP Pressure Drop validation.

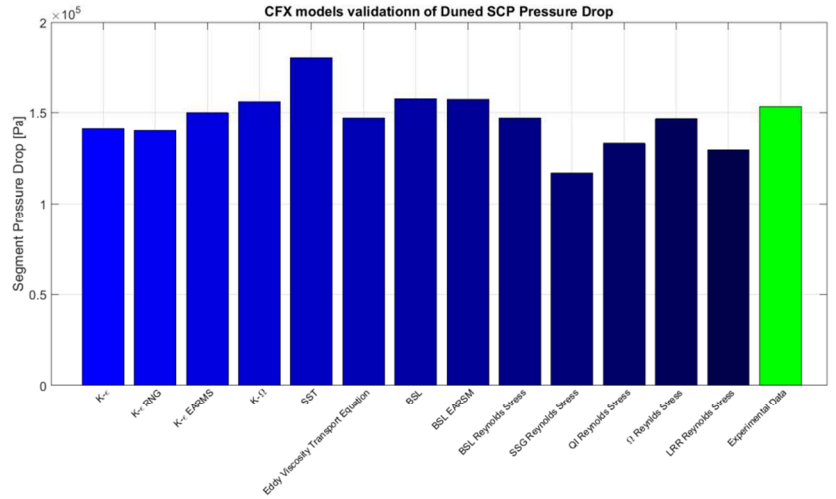

Figure 4.46 - Duned SCP Pressure Drop validation.

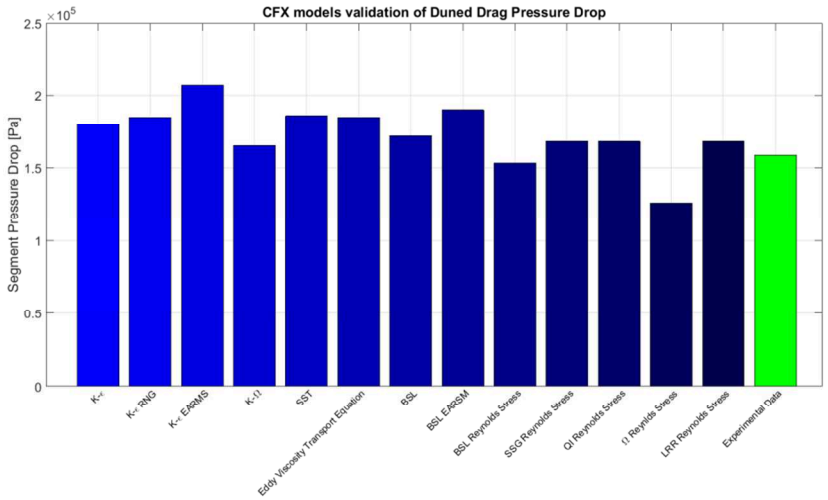

Figure 4.47 - Duned Drag SCP Pressure Drop validation.

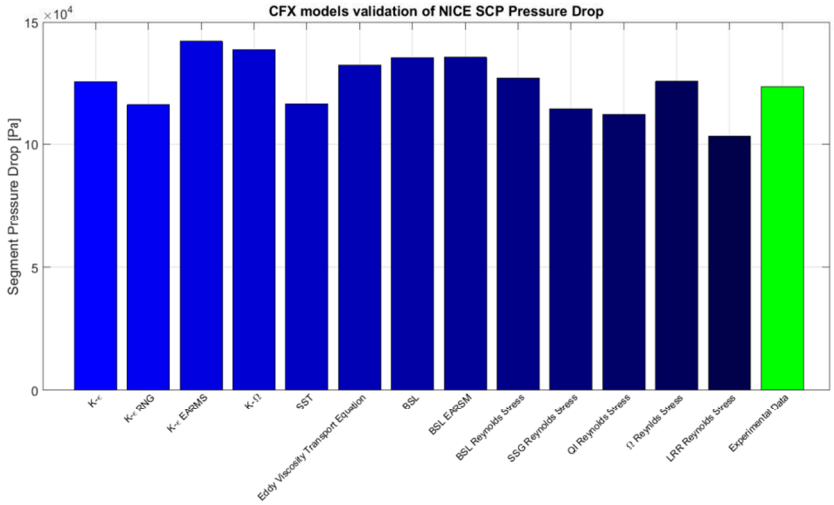

Figure 4.48 - NICE SCP Pressure Drop validation.

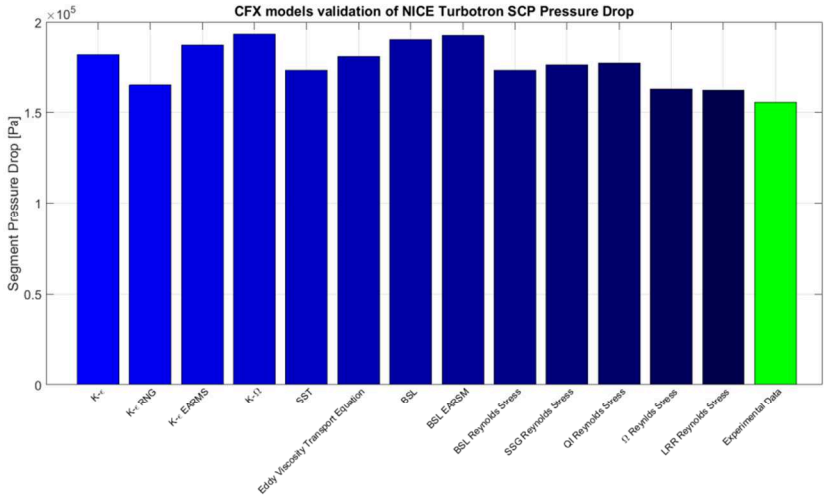

Figure 4.49 - NICE Turbotron SCP Pressure Drop validation.

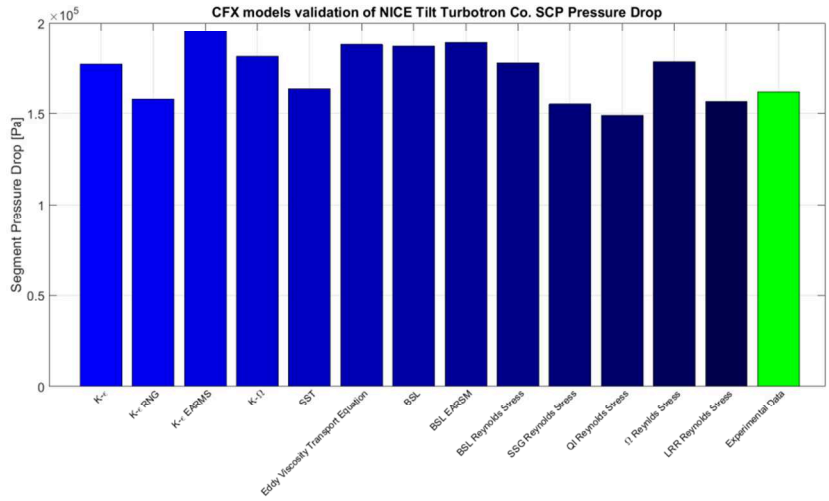

Figure 4.50 - NICE tilt Turbotron Co. SCP Pressure Drop validation.

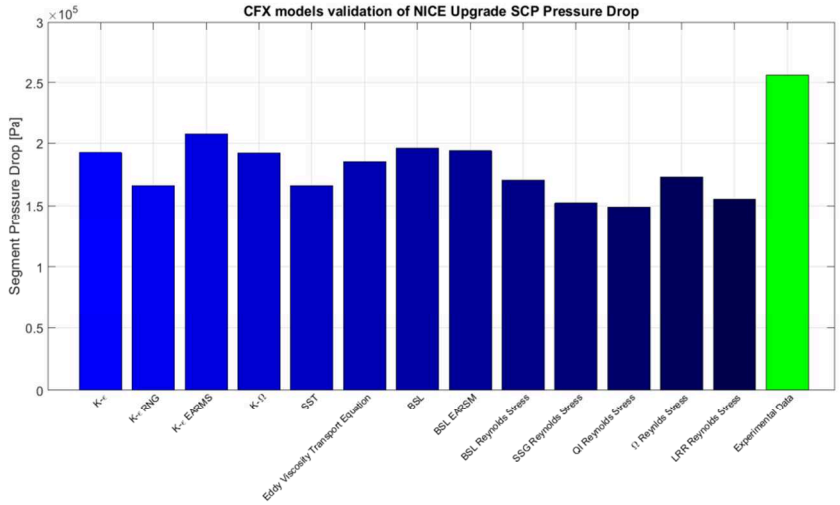

Figure 4.51 – NICE upgrade SCP Pressure Drop validation.

As clearly shown in Figure 4.43-4.52, the all different SCP can be properly described from in their fluid-dynamic behaviour but the NICE Upgrade one.
No particular difference can be appreciated between the Reynolds Stress Models (RSM) and the Reynolds Average Navier-Stokes (RANS) one for all the different geometry. It is therefore possible to limit the numerical cost of analyses and the computational time required in order to reach the converged solution exploiting the latter family of fluid models (i.e. K-ε, K-ε EARMS, K-Ω, SST and Eddy Viscosity Transport Equation).
As far as the discrepancy between the experimental and the numerical predictions of NICE Upgrade pressure drop is concerned, the result is quite surprising also considering the relative simplicity f the geometry to be modeled.
It would be worth verifying the correspondence between the channels as designed in CAD environment and the realized one. This test could be performed through an infrared camera detecting the thermal footprint of the channel wall when subjected to a

fast cooling transient. It could be indeed the case that the electrodeposition process could eventually result in a partial obstruction of the channel cross section leading to unavoidable increase of the associated hydraulic losses.

5

5. *Full scale application and Optimization of the novel cooling solutions*

The SCP conceptual geometries designed in order to increase the cooling performance in the electrostatic grids of the injector beam source are in this chapter applied to the full-scale geometry in order to numerically verify the possible enhancement in the reference operative conditions.

As a first step the heat loads acting on the whole segment of the accelerating grid have been analyzed in order to detect the presence of possible spatial inhomogeneities between the different beamlet groups and the cooling channel rows.

If this is the case a modulation of the different novel cooling solution could be thought in order to be able to contain the maximum thermal gradients occurring in copper structure below a given threshold.

The different novel cooling solutions have then been applied in the in the full scale models evaluating their performance both under the fluid-dynamic point of view and thermo-mechanical one with a particular attention to the estimated fatigue-life expectation.

Two additional alternative designs, one from the hydraulic point of view and the other from the mechanical one, have been investigated in order to evaluate the corresponding qualitative and quantitative variation in terms of performance.

Basing on the results obtained from the fluid-dynamic and thermo-mechanical point of view, the present design cooling solution (NICE) is then subjected to an optimization analysis with the objective of further minimizing the thermal field realized in the components, paving the way for a promising approach aimed to perform further improvement of performances in terms of fatigue life for the different designs.

5.1 Segment models

The SCP conceptual geometries designed in order to increase the cooling performance in the electrostatic grids of the injector beam source needs to be applied to segment geometry in order to numerically verify the possible enhancement in the full scale application.

To accomplish such objective the different grids have been investigated by means of three dimensional fully self-consistent fluid-thermal-structural models representing a whole grid segment. Such models exploit two combined approaches: on one hand the CFX computational fluid dynamics code permits to evaluate water parameters and the grid temperature in every point, on the other the ANSYS finite element code is instead exploited to calculate the resulting stresses, strains and deformations in the copper. An elastic-plastic model of copper was adopted, using the material properties measured during a comprehensive testing campaign carried out on electrodeposited samples produced with the same process foreseen for the grids.

As already mentioned in Chapter 3 the segment domains here considered consists of a 840 x 395 x 17mm planar grids. The planarity along the longitudinal direction of the segment is a CAD simplification since each opening group is indeed slightly deflected along the horizontal direction in order to provide the correct aiming to the accelerated beam.

From the fluid-dynamic point of view the accelerating grids segment are characterized by 12 inlet and outlet feeding and draining ducts connected to 2 inner manifolds. Between these two manifolds is comprised the cooling system constituted by 17 cooling channels connected in parallel. The overall mass flow feeding the one electrostatic grid segment is the one associated to the nominal operating scenario (4.7 kg/s).

From the mechanical point of accelerating grids are characterized by 15.5 mm slits, both in the frame and core regions, in order to help with thermal stress flux relieving.

On the corners and half of the height side there are the six slots designed for the required pins needed to maintain the accelerating grids in the exact positions in the injector beam source.

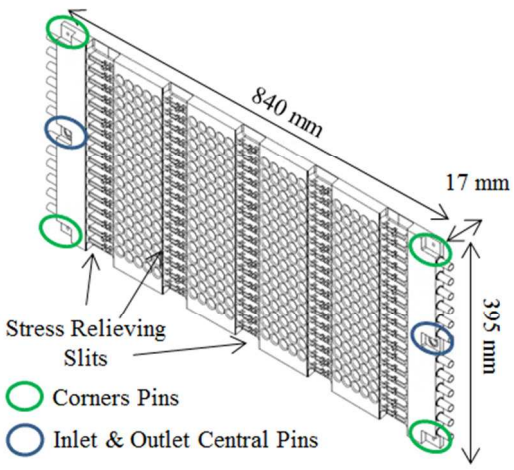

Figure 5.1 - Isometric view of the segment grid model.

5.2 SCP design implementation

Before proceeding with the implementation of the different SCP design in the full scale model, an evaluation on the characteristics of the input heat load (AG4) has been carried out. Particular attention has been given to the possible presence of non-homogeneous spatial distribution between the different beamlet groups and the upstream surface regions afferent to the different cooling channels in terms of thermal power disposal.

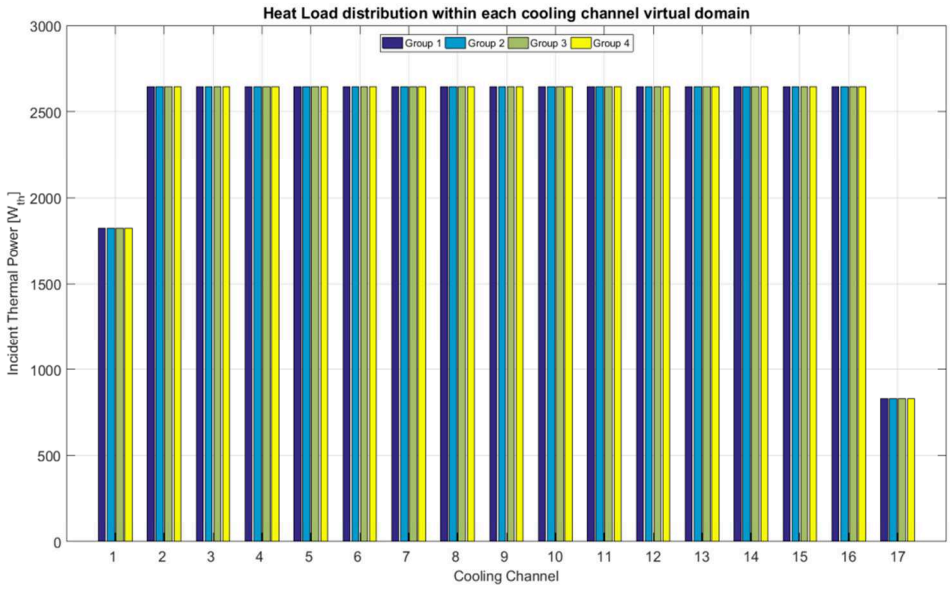

Figure 5.2 - AG4 heat load distribution along the different cooling channel and beamlet groups.

The results depicted in Figure 5.2 states that there is a homogenous spatial distribution between the different cooling channel composing a beamlet and between the four beamlet groups in terms of heat loads applied to the upstream heat surface.
The only deviation from this uniform behaviour is constituted by the two extreme channels which, being coupled with one superior or inferior half to the beamlet groups openings surfaces, experience a smaller incoming heat flux. In addition the last vertical row of opening experiences a sensible a smaller load than the one at the bottom of the grid.
As a matter of fact the 17 parallel cooling channels are not implemented in the grid in the same way. The 15 channels realized in the regions between two opening rows have been realized in full size, while the remaining two along the upper and lower distribution of apertures have been realized as half of the original design as they are required to dispose, in average, half of the thermal load with respect to the others.
Additional cooling of region not subjected to heat loads would indeed lead to increased thermal gradient leading to decrease of performance in terms of containment of the equivalent Von Mises strain and hence in terms of fatigue life expectation.
Among the innovative SCP design, just nine solutions been upgraded to the cooling solution inside the accelerating grid segments.

With respect to the original set of cooling proposals, the Tilt Turbotron Channel geometry has, indeed, not been assessed. The reason behind this choice is double: on one side it was observed a strong difficulty in solving the related numerical problem, on the other the correspondent manufactured prototype is not meeting the original CAD design, introducing a further lack of experimental verification of the results numerically obtained.

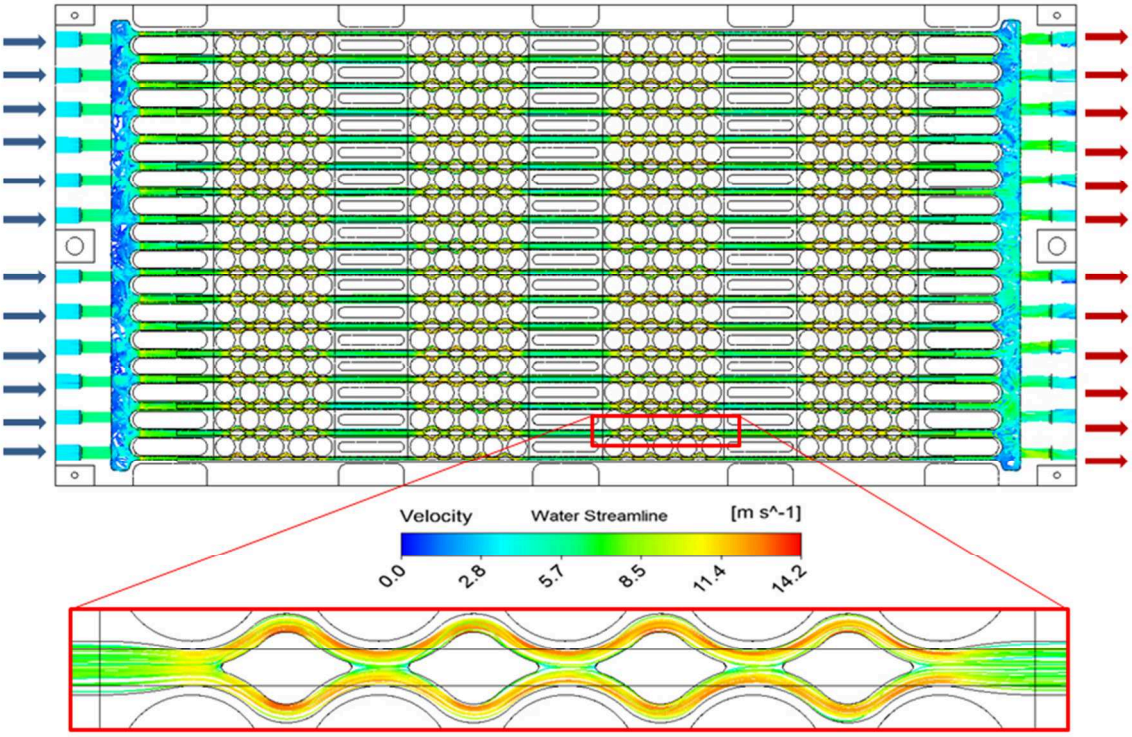

Figure 5.3 - - Schematic representation of the segment cooling circuit with NICE channel design.

5.3 Cooling and mechanical performance assessment

The results obtained by the CFD analyses for the different cooling solutions of the electrostatic grid segment are reported in Table 5.1. The thermofluid-dynamic quantities that have been assessed are:

- the pressure drop between the inlet and outlet sections;
- the maximum and mean temperature of copper;
- the maximum coolant velocity at channel walls;
- the maximum and mean heat transfer coefficient;
- the maximum copper temperature at the channel walls;
- the maximum water temperature at the channel walls;
- the maximum temperature gradient at the channel walls between copper and water domain.

The last set of three parameters is of particular interest in assessing the cooling efficiency of the heat transfer mechanism.

Table 5.1 - CFD results of the segment model analyses.

Design Solution	Segment Model (with mechanical slits)								
	Δp [bar]	Tmax [°C]	Tmean [°C]	Max Vwall [m/s]	HTC max [W/m²°C]	HTC mean [W/m²°C]	Tmax Copper Interface [°C]	Tmax Water Interface [°C]	Interface Max Gradient [°C]
Baffle Channel	7.82	137.40	60.87	15.03	159553	59618	104.55	71.42	33.13
Criss-Cross Channel	7.34	135.45	61.22	13.85	130133	59562	106.48	70.85	35.63
Diverted Channel	6.45	139.27	61.78	11.89	248495	58002	109.98	78.09	31.89
Duned Channel	5.10	146.57	66.70	13.86	123512	59674	123.96	74.77	49.19
Duned Drag Channel	5.63	137.80	62.59	15.86	681628	59690	115.32	79.33	35.99
NICE Channel	3.55	147.06	65.06	11.57	129358	58363	112.09	71.97	40.12
NICE Upgrade	7.07	135.532	61.97	18.51	148144	62738	109.54	67.55	42.00
Turbotron Channel	5.69	144.15	63.87	14.67	129587	60708	109.50	72.66	36.84
Single Straight Channel	2.29	183.73	74.17	13.13	135118	62961	119.62	79.13	40.49

The thermofluid-dynamic results have successively been imported on the structural model in order to assess the segment from the mechanical point of view.
The constraints acting on the grid have been introduced on the six pins cavities obtained along the two lateral sides of the copper segment, as shown in Fig. 5.1.
The central pin at the inlet side locks the grid along the longitudinal and vertical directions; the central pin at the outlet side locks along the vertical direction, while the remaining four at the corners lock in the out of plane direction.
Table 5.2 illustrates the results obtained from the FEM analyses with the implementation of the nine different cooling channel designs inside the grid.

Table 5.2 – Maximum and minimum FEM results of the segment model analyses (1).

Design Solution	Segment Model (with mechanical slits)							
	X-direction Deformation [mm]		Y-direction Deformation [mm]		Z-direction Deformation [mm]		Total Deformation [mm]	
Baffle Channel	0.606	-0.066	0.206	-0.228	0.872	-0.058	0.906	0.000
Criss-Cross Channel	0.611	-0.069	0.208	-0.232	0.912	-0.060	0.947	0.000
Diverted Channel	0.620	-0.069	0.211	-0.235	0.912	-0.060	0.950	0.001
Duned Channel	0.684	-0.115	0.265	-0.288	1.876	-0.125	1.896	0.002
Duned Drag Channel	0.628	-0.078	0.221	-0.244	1.084	-0.072	1.116	0.002
NICE Channel	0.653	-0.083	0.234	-0.260	1.100	-0.073	1.132	0.001
NICE Upgrade	0.613	-0.076	0.214	-0.237	0.983	-0.065	1.016	0.001
Turbotron Channel	0.635	-0.076	0.226	-0.249	0.992	-0.066	1.028	0.001
Straight Channel	0.780	-0.095	0.307	-0.336	1.492	-0.097	1.526	0.001

Table 5.3 - Maximum and minimum FEM results of the segment model analyses (2).

Design Solution	Segment Model (with mechanical slits)								
	Equivalent elastic strain [mm/mm]		Equivalent plastic strain [mm/mm]		Equivalent total strain [mm/mm]		Equivalent stress [MPa]		Fatigue Life [cycles]
Baffle Channel	0.064%	4.44E-08	0.034%	0.000%	0.092%	0.000%	70.979	5.14E-03	594411
Criss-Cross Channel	0.063%	3.42E-08	0.036%	0.000%	0.096%	0.000%	72.191	3.98E-03	477866
Diverted Channel	0.064%	5.50E-08	0.040%	0.000%	0.101%	0.000%	73.958	6.41E-03	382240
Duned Channel	0.080%	8.23E-08	0.089%	0.000%	0.169%	0.000%	90.975	8.11E-03	50165
Duned Drag Channel	0.063%	6.38E-08	0.049%	0.000%	0.111%	0.000%	72.980	7.43E-03	248634
NICE Channel	0.067%	1.21E-07	0.053%	0.000%	0.121%	0.000%	76.977	1.32E-02	178125
NICE Upgrade	0.060%	3.45E-08	0.040%	0.000%	0.100%	0.000%	69.604	3.99E-03	401509
Turbotron Channel	0.065%	3.88E-08	0.047%	0.000%	0.112%	0.000%	74.502	4.51E-03	243174
Straight Channel	0.102%	1.33E-07	0.140%	0.000%	0.242%	0.000%	117.100	1.43E-02	8848

With respect to the results obtained in the numerical analyses performed on SCPs'domain, a different hierarchy in terms of cooling performance can be noticed. As

far as the segment model is concerned, the Criss-Cross design is the solution which guarantees the best heat disposal in terms of minimization of the maximum temperature reached in the copper grid.
The different thermal expansions of the grid, which identify a correspondent equivalent total strain whose maximum limits the grid fatigue life is however driven by a combined effect of the maximum and mean temperature of the segment. From this point of view the design of the Baffle Channel is once again the solution able to increase to the maximum extent the fatigue life of the accelerating segments.
On the other hand the four designs (Baffle Channel, Criss-Cross Channel, Diverted Channel and NICE Upgrade Channel) which are providing the best cooling and mechanical performance are the ones affected by the highest pressure drops along the circuit.
It is worth noticing that the simplest solution described by the Straight Channel is the one which is characterized by the best hydraulic performance but is not able to accomplish at all the requirements set on the mechanical behaviour of the grids.
As things stand, from the numerical point of view the best compromise solution is the Duned Drag Channel which is able to extend the fatigue life of about 40% with respect to the present design solution (i.e. 178125 beam on-off cycles with NICE Channel cooling) without penalizing too much the hydraulic performance of the cooling circuit.
In order to further limit the pressure losses along the electrostatic segment it has been thought to modify the design of the extreme superior and inferior channel. As already state these channels are just the half of the other 15 central ones (with the cooling modules oriented toward the beamlet openings) due to the lower heat load they have to dispose.
However dividing the cooling channels in two halves does not imply the pressure drop to follow a decreasing trend, but on the contrary due to the reduction of the hydraulic diameter they tend to increase with respect to the original configuration.
Such consideration led to the idea of replacing the extreme halves channels of the considered SCP design with those coming from the NICE design for the all nine analyses performed. This operation would also lead to improve the feasibility of the manufacturing operations in reason of the design simplification of the narrowest cooling channels.
As a matter of fact the NICE Channel and the Single Straight Channel are excluded from such set of additional analyses, the former because the insertion of the new channels at the extremities of the cooling circuit would not lead to any difference from the original starting configuration, the latter since the new channels at the extremities of the cooling circuit would not lead to higher hydraulic losses with respect to the original starting configuration with 7x2 mm straight channels.

Table 5.4 - CFD results of the segment model analyses with modified extreme channels.

	Segment Model (with mechanical slits) Extreme Channel								
Design Solution	**Δp [bar]**	**Tmax [°C]**	**Tmean [°C]**	**Max Vwall [m/s]**	**HTC max [W/m²°C]**	**HTC mean [W/m²°C]**	**Tmax Copper Interface [°C]**	**Tmax Water Interface [°C]**	**Interface Max Gradient [°C]**
Baffle Channel	7.42	135.12	60.28	18.89	145999	62046	105.18	69.11	36.08
Criss-Cross Channel	7.09	134.71	60.76	18.40	144482	63115	108.34	70.87	37.48
Diverted Channel	6.34	137.36	61.62	17.34	480999	61097	111.19	78.45	32.74
Duned Channel	5.05	145.35	66.22	15.46	124655	63154	125.74	75.01	50.48
Duned Drag Channel	5.51	136.54	62.10	17.00	615674	62974	117.44	80.13	37.32
NICE Channel	-	-	-	-	-	-	-	-	-
NICE Upgrade	6.81	134.45	61.32	19.43	156486	63489	111.45	68.15	43.68
Turbotron Channel	5.54	142.76	63.13	15.68	134568	62165	111.87	73.44	37.46
Single Straight Channel	-	-	-	-	-	-	-	-	-

Table 5.5 - Maximum and minimum FEM results of the segment model analyses with modified extreme channels **(1).**

	Segment Model (with mechanical slits) Extreme Channels							
Design Solution	**X-direction Deformation [mm]**		**Y-direction Deformation [mm]**		**Z-direction Deformation [mm]**		**Total Deformation [mm]**	
Baffle Channel	0.594	-0.059	0.202	-0.219	0.900	-0.060	0.938	0.001
Criss-Cross Channel	0.603	-0.065	0.211	-0.230	0.992	0.211	1.027	0.001
Diverted Channel	0.615	-0.065	0.216	-0.234	0.976	-0.065	1.013	0.001
Duned Channel	0.679	-0.110	0.269	-0.289	1.954	-0.127	1.914	0.001
Duned Drag Channel	0.638	-0.074	0.224	-0.243	1.157	-0.075	1.178	0.001
NICE Channel	-	-	-	-	-	-	-	-
NICE Upgrade	0.627	-0.072	0.219	-0.236	1.053	-0.067	1.076	0.001
Turbotron Channel	0.643	-0.073	0.230	-0.250	1.068	-0.072	1.086	0.001
Straight Channel	-	-	-	-	-	-	-	-

Table 5.6 - Maximum and minimum FEM results of the segment model analyses with modified extreme channels (2).

	Segment Model (with mechanical slits) Extreme Channels								
Design Solution	**Equivalent elastic strain [mm/mm]**		**Equivalent plastic strain [mm/mm]**		**Equivalent total strain [mm/mm]**		**Equivalent stress [MPa]**		**Fatigue Life [cycles]**
Baffle Channel	0.061%	2.98E-08	0.040%	0.000%	0.101%	0.000%	70.814	3.46E-03	396663
Criss-Cross Channel	0.067%	3.18E-08	0.043%	0.000%	0.109%	0.000%	77.487	3.69E-03	269673
Diverted Channel	0.065%	3.28E-08	0.048%	0.000%	0.111%	0.000%	75.708	3.81E-03	245789
Duned Channel	0.082%	5.74E-08	0.094%	0.000%	0.176%	0.000%	93.451	4.46E-03	39159
Duned Drag Channel	0.062%	6.12E-08	0.053%	0.000%	0.115%	0.000%	75.684	5.47E-03	215841
NICE Channel	-	-	-	-	-	-	-	-	-
NICE Upgrade	0.061%	4.15E-08	0.046%	0.000%	0.107%	0.000%	72.689	2.47E-03	291027
Turbotron Channel	0.064%	4.01E-08	0.052%	0.000%	0.116%	0.000%	79.465	4.47E-03	208647
Straight Channel	-	-	-	-	-	-	-	-	-

Despite the improvement in term of pressure drop, though negligible since in the order of some tenths of bar, present design configuration leads to slight increases of the equivalent total strain, which due to the particular trend of the fatigue curve in electrodeposited copper produce a substantial reduction of the fatigue life of the component.

Due to the marginal low additional pumping cost with liquid fluid it is therefore preferable not to perform such pressure loss savings, since the much longer fatigue life of the components produce a higher cost saving in terms of amortization of the manufacturing price.
The last set of analyses proposes the electrostatic accelerating grid constituted by the former configuration of the cooling channels but avoiding the realization of the mechanical slits. The objective of this study is to understand if there exists some cooling solution able to satisfy alone the mechanical constraints imposed on the grids. This would be of technical interest if any issue rose from the milling operations for the realization of the grooves for the creation of the slits.

Table 5.7 - CFD results of the segment model analyses without SRS.

	Segment Model (with mechanical slits)								
Design Solution	**Δp [bar]**	**Tmax [°C]**	**Tmean [°C]**	**Max Vwall [m/s]**	**HTC max [W/m²°C]**	**HTC mean [W/m²°C]**	**Tmax Copper Interface [°C]**	**Tmax Water Interface [°C]**	**Interface Max Gradient [°C]**
Baffle Channel	7.82	137.40	60.87	15.03	159553	59618	104.55	71.42	33.13
Criss-Cross Channel	7.34	135.45	61.22	13.85	130133	59562	106.48	70.85	35.63
Diverted Channel	6.45	139.27	61.78	11.89	248495	58002	109.98	78.09	31.89
Duned Channel	5.10	146.57	66.70	13.86	123512	59674	123.96	74.77	49.19
Duned Drag Channel	5.63	137.80	62.59	15.86	681628	59690	115.32	79.33	35.99
NICE Channel	3.55	147.06	65.06	11.57	129358	58363	112.09	71.97	40.12
NICE Upgrade	7.07	135.532	61.97	18.51	148144	62738	109.54	67.55	42.00
Turbotron Channel	5.69	144.15	63.87	14.67	129587	60708	109.50	72.66	36.84
Single Straight Channel	2.29	183.73	74.17	13.13	135118	62961	119.62	79.13	40.49

Table 5.8 - Maximum and minimum FEM results of the segment model analyses without SRS (1).

	Segment Model (with mechanical slits)							
Design Solution	**X-direction Deformation [mm]**		**Y-direction Deformation [mm]**		**Z-direction Deformation [mm]**		**Total Deformation [mm]**	
Baffle Channel	0.591	-0.057	0.166	0.191	0.687	-0.052	0.738	0.000
Criss-Cross Channel	0.598	-0.059	0.168	-0.194	0.710	-0.054	0.761	0.001
Diverted Channel	0.605	-0.059	0.170	-0.197	0.699	-0.053	0.753	0.001
Duned Channel	0.671	-0.102	0.200	-0.230	1.453	-0.107	1.481	0.003
Duned Drag Channel	0.614	-0.063	0.173	-0.201	0.782	-0.059	0.832	0.001
NICE Channel	0.634	-0.071	0.182	-0.213	0.853	-0.065	0.901	0.002
NICE Upgrade	0.605	-0.066	0.170	-0.199	0.785	-0.059	0.831	0.001
Turbotron Channel	0.624	-0.066	0.179	-0.208	0.767	-0.058	0.818	0.003
Straight Channel	0.755	-0.076	0.222	-0.257	1.030	-0.084	1.087	0.003

Table 5.9 - Maximum and minimum FEM results of the segment model analyses without SRS (2).

	Segment Model (with mechanical slits)								
Design Solution	**Equivalent elastic strain [mm/mm]**		**Equivalent plastic strain [mm/mm]**		**Equivalent total strain [mm/mm]**		**Equivalent stress [MPa]**		**Fatigue Life [cycles]**
Baffle Channel	0.072%	1.53E-08	0.063%	0.000%	0.133%	0.000%	83.642	1.78E-03	128617
Criss-Cross Channel	0.074%	1.54E-08	0.063%	0.000%	0.135%	0.000%	86.079	1.79E-03	122733
Diverted Channel	0.077%	1.22E-08	0.067%	0.000%	0.142%	0.000%	89.135	1.41E-03	105025
Duned Channel	0.109%	2.74E-08	0.139%	0.000%	0.247%	0.000%	124.860	3.17E-03	13404
Duned Drag Channel	0.084%	1.48E-08	0.092%	0.000%	0.176%	0.000%	97.088	1.72E-03	39617
NICE Channel	0.091%	1.45E-08	0.095%	0.000%	0.185%	0.000%	104.920	1.68E-03	29154
NICE Upgrade	0.078%	1.47E-08	0.076%	0.000%	0.154%	0.000%	89.486	1.72E-03	76471
Turbotron Channel	0.089%	1.35E-08	0.090%	0.000%	0.179%	0.000%	102.340	1.56E-03	35353
Straight Channel	0.126%	2.96E-08	0.194%	0.000%	0.320%	0.000%	145.820	3.42E-03	4169

Since no change occurred in the design of the cooling channel it can be noted that the results listed in Table 5.7 are not moving away from those contained in Table 5.1.
From the mechanical point of view it is worth observing that avoiding the realization of the mechanical slits just four designs are nevertheless able to respect the thermo-mechanical constraints imposed on the accelerating grids.
Considering the relevant uncertainties that lie between the fluid-dynamic behaviour of the NICE Upgrade design as numerically predicted and experimentally verified the range of possible solution further decrease to the Baffle, the Criss-Cross and the Diverted channels.
The associated fatigue life prediction is however considerably lower with respect to the present design cooling solution (c.f. Table 5.1 - NICE channels with mechanical slits) leading the drawback associated to this design simplification to be very costly and worth to be discarded if not necessary.

5.4 Optimization process

Once the performances of the novel designs have been assessed on the full-scale segment model, the different geometries have been parametrized in order to perform the optimization of the channel shape. Such operation aimed at improving the cooling performances while respecting the given limitations on the channel design topology, fluid velocity at the channel walls and pressure drops.
Of these the most limiting ones for a direct implementation in a MITICA-like experiment are the hydraulic losses developed along one segment grid. In order to match the cooling circuit characteristic they should be indeed contained to 6 bar or less.
Due to the large number of analysis runs required (ca. 600) to realize an appropriate design optimization, it is necessary to perform such study on the Single Channel Prototype (SCP) model rather than on the full-scale segment ones.
Such sub-modeling would in fact reasonably limit the computational effort to a reasonable time.
On the other hand, however, the SCP model is not the smallest model able to take into consideration all the given input for an effective ultimate optimization of design. Due to the alternate magnetic deflection of the accelerated particle the smallest subsystem which is able to best describe the entire electrostatic grid is the Strip model, a double vertical set of 5 beamlet aperture constituting 1/8 of the overall beamlet group.
On this system the application of the translational vertical periodicity of the heat flux would be indeed able to accurately reproduce the thermal diffusive phenomena occurring in the overall segment model.
Let it be the SCP or the Strip model the reference domain where performing the optimization process, a construction of a proper scaling relation between the pressure drops evaluated along the chosen sub-models and the losses realized in the full segment geometry would result necessary.

Three different families of analysis provide the needed coefficients to build the sought relation, taking into account three different scaling and perturbing coefficients:

- A segment model analysis with 17 full size channels and equipartition of the mass flow between them;

- A segment model analysis with 17 full size channels and a global inlet boundary condition able to introduce a perturbation in the different mass flows circulation in the channels;

- A segment model analysis with 15 full size channels and the two extreme ones realized as half of the original design and a global inlet boundary condition able to introduce a further perturbation factor due to non-perfectly balance between the different branches of the cooling system.

Due to the large cost to pay in term of computational time needed to perform such characterization it has been opted for a much simplified approach taking into consideration what could be the ultimate pressure drop in one single beamlet group in order to maintain the global hydraulic losses below the 6 bar threshold.

Table 5.10 – Intermediate and overall pressure drops along the electrostatic grid segment for the different SCP designs.

	Segment Model (with mechanical slits)									
Design Solution	**Δp inlet [bar]**	**Δp group 1 [bar]**	**Δp frame 1 [bar]**	**Δp group 2 [bar]**	**Δp frame 2 [bar]**	**Δp group 3 [bar]**	**Δp frame 3 [bar]**	**Δp group 4 [bar]**	**Δp outlet [bar]**	**Δp [bar]**
Baffle Channel	0.41	1.78	0.04	1.77	0.04	1.76	0.04	1.74	0.23	7.82
Criss-Cross Channel	0.41	1.65	0.05	1.64	0.05	1.63	0.05	1.62	0.22	7.34
Diverted Channel	0.41	1.46	0.02	1.45	0.01	1.45	0.02	1.44	0.19	6.45
Duned Channel	0.41	1.08	0.06	1.08	0.06	1.07	0.06	1.06	0.23	5.10
Duned Drag Channel	0.41	1.18	0.05	1.23	0.05	1.23	0.05	1.24	0.18	5.63
NICE Channel	0.41	0.71	0.04	0.70	0.04	0.70	0.04	0.69	0.22	3.55
NICE Upgrade	0.41	1.57	0.06	1.56	0.06	1.55	0.06	1.54	0.25	7.07
Turbotron Channel	0.41	1.33	-0.03	1.33	-0.05	1.34	-0.06	1.32	0.09	5.69
Single Straight Channel	0.84	0.21	0.12	0.20	0.12	0.20	0.12	0.20	0.27	2.29

Table 5.10 depicts the pressure drops realized with the various cooling solutions in each different section of the grid segment. In order to satisfy the present pressure drop constraints acting on MITICA experiment the maximum hydraulic loss to be realized in each beamlet group should not exceed 1.40 bar.

Table 5.11 - Reference value for the optimization process.

Design Solution	Δp [bar]	Δp group [bar]	Tmax [°C]	Vwall [m/s]
Baffle Channel	1,830	1,209	120,37	15,05
Criss-Cross Channel	1,714	1,151	124,22	14,85
Diverted Channel	1,798	1,215	121,14	20,02
Duned Channel	1,690	1,104	133,87	14,09
Duned Drag Channel	1,781	1,098	126,44	13,66
NICE Channel	1,288	0,693	143,48	12,60
NICE Upgrade Channel	1,724	1,043	132,46	20,04
Turbotron Channel	1,720	1,120	134,91	15,52
Tilt Turbotron Channel	1,723	1,113	133,64	14,67
Straight Channel	0,917	0,223	178,31	9,29

The reference thermofluid-dynamic performances of the innovative cooling channels proposals realized on SCPs domain are illustrated in Table 5.11.
From the comparison of Table 5.10 and 5.11 it can be noted that there is not a straight correspondence between the pressure drops realized in one group of the electrostatic grid segment and in the SCP. This is particularly true for the most demanding design in terms of hydraulic losses. Such difference is ascribable to the three different perturbing coefficients aforementioned.
The first step required by the optimization procedure is the individuation of a set of input parameters associating them to a feasible range of variation. In this particular context they are all geometric ones.
The consequent design space is explored with the software modeFRONTIER resulting with the Pareto region associated to the objective of the process: the best compromise between the enhancements of the cooling performance without excessive penalization in terms of hydraulic losses.
Because of the extended time required to the resolution of each optimization stage (about 1 month), the only geometry whose assessment has been completed for the moment in such multi-objective analysis is the one associated to the present reference design (i.e. NICE channel).
The optimization work flow is organized as depicted in the schematic representation illustrated in Figure 5.

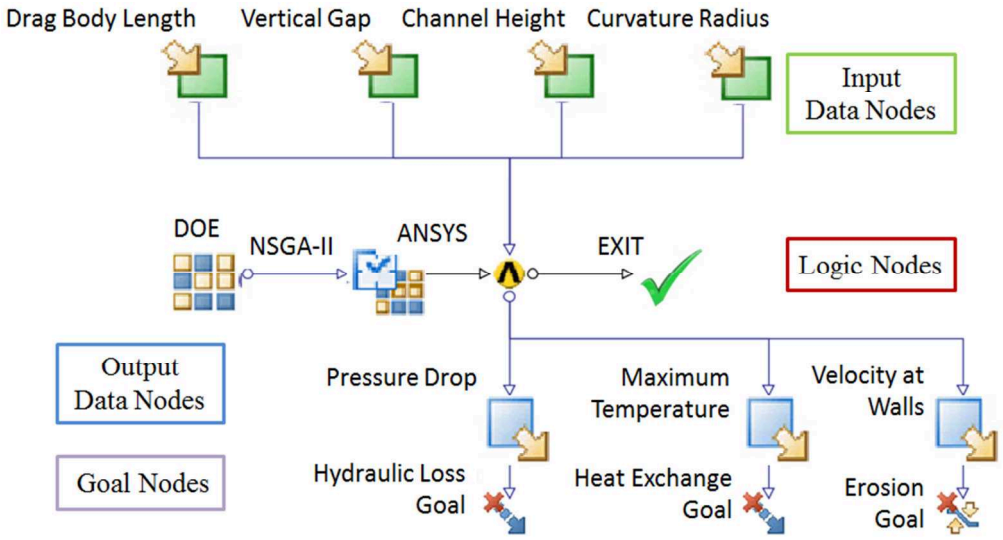

Figure 5.4 - Schematic representation of the optimization process workflow.

The first step required for the implementation of the process workflow is the definition of the input data nodes.
With respect to the NICE geometry, six different design variables have been chosen as input data nodes, each associated to a feasible range of variation, as reported in Table 5.11.

Table 5.12 - Range of variation of the variables involved in the optimization process.

	Lower bound	Upper bound
1) Drag Body Length	7.5 mm	17 mm
2) Vertical Gap	0.5 mm	5 mm
3) Channel Height	1.2 mm	3 mm
4) Curvature radius	10.2 mm	11.1 mm
5) Channel width	7.5 mm	8.6 mm
6) Electrodeposited layer	1 mm	2 mm

The drag body length parameter is the distance between the two edges of the central body detouring the flow in the two sub-channels. 7.5 mm is the lowest threshold in order to be able to build the body with a proper curvature, 17 is instead the upper limit able to guarantee a sufficient space for the two coolant fluxes to rejoin.
The vertical gap is instead limited in the range 0.5-5 mm, the former value is the one able to guarantee a 1 mm distance between the two channel walls from one side and the other of the beamlet opening, the latter is instead the present design value.
The channel height parameter is instead governing the amplitude of the cooling channels at its maximum point of curvature, 1.2 mm is the limit deriving from technological constraints on the milling machine while 3mm is the value which, considering the two sub-channel, will compose again a cross section of 7x6 mm as the one along the frame region of the grid.
The channel curvature radius is parameter governing the internal curvature of the channel bend, 1.2 mm is again the technological limit given by the milling operation while 11.1 mm is due in order to guarantee a coherent blending of the central drag body.
The channel width is instead referring to the thickness of the cooling channel along the beamlet group segment, 8.6 is the nominal distance from the upstream surface able to guarantee 1mm distance from the groove for the magnets while 5 mm is an appropriate minimum distance able to guarantee a not too sharp increase of pressure losses.

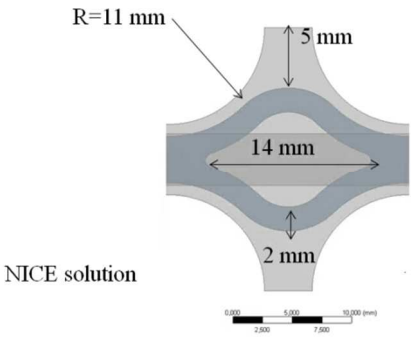

Figure 5.5 - Schematic Representation of the starting NICE design with corresponding labels on the input data nodes according the enumeration in Table 5.11.

Though the thickness of the electrodeposited layer was a given constraint set at 1.5 mm in order to guarantee a sufficient structural robustness to the grid, it was however parametrized the same during such optimization stage in order to be able to understand what could be the trade-off thickness of the layer in order to optimize the simultaneous heat transfer mechanism toward the cooling channel walls and along the longitudinal direction.

Coming back to the optimization process workflow, below the input data nodes is the logic nodes workflow. A Design of Experiments (DOE) table based on a pseudo random SOBOL sequence has been generated [22]. Such space filler algorithm works best with a number of variables from 2 to 20, producing a variable number of design configurations that are uniformly distributed in the design space (in this particular case 26).

Since the tentative designs might be characterized by a high percentage of error due to the unfeasible combination of the input data, the evolutionary algorithm that has been set to manage the scheduler is the NSGA-II (Non-dominated Sorting Genetic Algorithm) [23]. Such algorithm is particularly recommended as it implements different elitism strategies for multi-objective search and allows concurrent evaluation of the independent individuals.

The number of generations that evolve from the 26 entries in the DOE table is 23, leading an overall 598 designs to be assessed.

Figure 5.6 depicts the associated correlation matrix which evaluates a correlation coefficient r between pairs of variables according the Equation 5.1:

$$r = \frac{N\sum_N xy - (\sum_N x)(\sum_N y)}{\sqrt{[N\sum_N x^2 - (\sum_N x)^2][N\sum_N y^2 - (y)^2]}} \tag{5.1}$$

where N is the number of pairs of values and x and y a generic pair of variable to correlate.

A correlation coefficient close to -1 means that the variables in a pair are inversely correlated (i.e. increasing channel height the velocity at channel walls decreases due to the continuity law), a correlation coefficient close to 1 means that the variables in a pair are directly correlated, while a correlation coefficient close to 0 means that two variables are not correlated.

The most important issue is that the initial set of input variables must be uncorrelated in order to avoid to introduce free parameter whose effects on the system has already been taken into account by other ones.

Figure 5.7 illustrates the Pareto frontier produced by the here considered optimization process. While the general aim of a single objective optimization is to find one global optimum design, in a multi-objective one the aim is to find a set of non-dominating solutions (i.e. those designs whose performance cannot be improved without worsening the results related with other objectives).

The Pareto frontier is the edge curve composed by these non-dominating solutions. Any design contained along present frontier can be taken as a local optimum solution in accordance to the given constraints imposed to the problem.

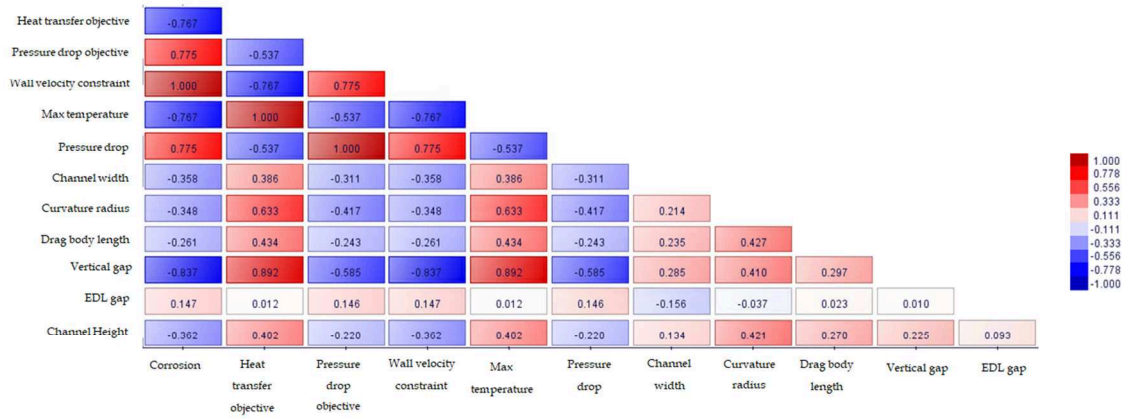

Figure 5.6 - Correlation matrix of the variables involved in the optimization process.

In this particular application the Pareto frontier is inserted in a chart representing the maximum temperature reported inside copper (Y-axis) with respect to the associated pressure drop developed between the inlet and outlet SCP sections (X-axis).
The colors of the different bubbles give instead an indication of the value associated to the parameter describing the minimum gap between the channel walls and upper and lower surfaces of the SCP inside each tentative design.
With respect of the objective of this analysis, the local optimum solution is the one that lies on the curve and best matches the pressure drop taken as the target in order not to exceed the 6 bar threshold imposed to the cooling circuit associated to the segment model.

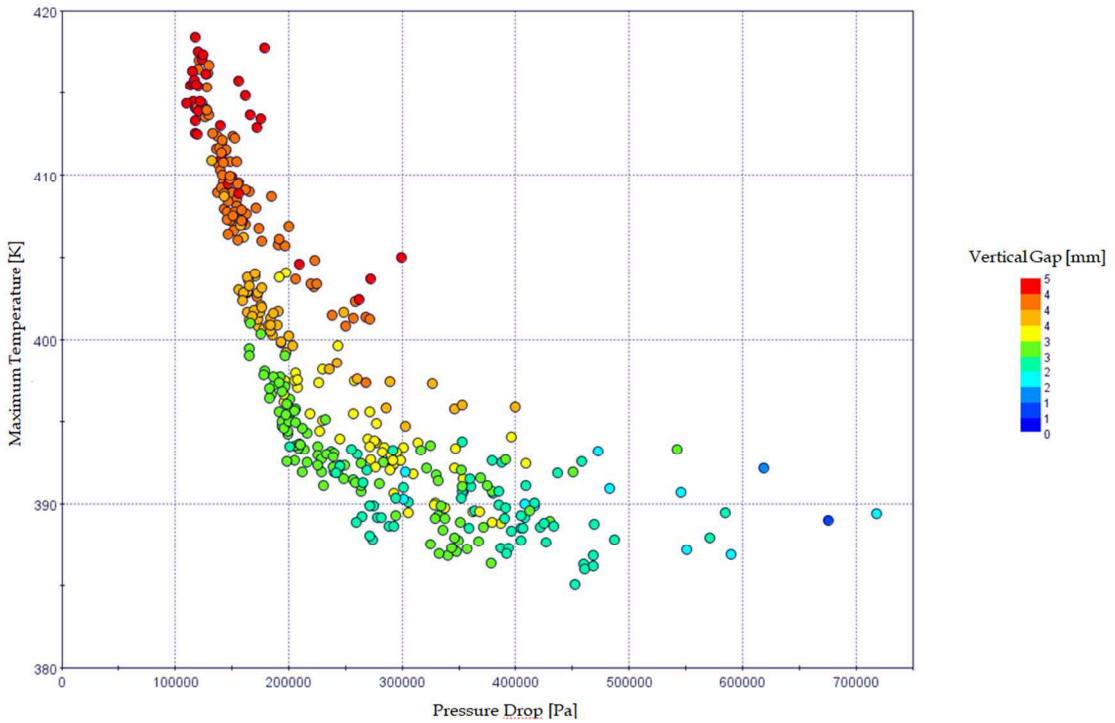

Figure 5.7 - Bubble chart showing the Pareto frontier in a Tmax- Δp plot associated to the optimization of the NICE channel.

Despite the correlation between the pressure drop realized on the SCP design and the segment model is still under investigation, it can be considered in first approximation that a loss of about 1.65 bar in the single channel model (corresponding 0.95 bar along the beamlet group region) would be able to guarantee the respect of the threshold imposed on MITICA circuit.
The application of the optimization process to such project design solution has led to the cooling module whose characteristics are described in Figure 5.8. Such design substantially decreases the SCP maximum temperature (from 144.66°C to 129.02°C), while still guarantying an acceptable hydraulic loss (1.646 bar), not excessive velocity at channel walls and reliable manufacturing process.
Such optimum solution has however to be verified with some structural considerations. The optimum thickness of the electrodeposited layer able to maximize the thermal transfer mechanism has in fact been evaluated in 1.1 mm, relatively well below the 1.5 mm in the present design.

Input variables	Value
Channel height	2.295 mm
EDL gap	1.1021 mm
Vertical gap	3.0800 mm
Drag body length	16.523 mm
Curvature radius	11.009 mm
Channel width	8.5119 mm
Output variables	Value
Pressure drop	1.6495 bar
Maximum Temperature	399.10 K
Channel wall velocity	18.706 m/s
Objectives	Value
Pressure loss	1.6495 bar
Heat Transfer	399.10 K
Constraints	Value
Corrosion	18.706 m/s

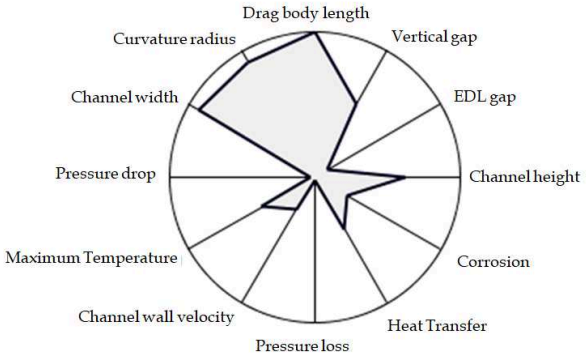

Figure 5.8 - Characterization of the local optimum solution of interest.

The optimum thickness value tells that the present design sacrifices the possibility of enhancing the cooling performance (increasing too much the distance between the upstream surface of the electrostatic grid and the channel wall) for a more robust design.
In case the reduction of the thickness is not possible the same analysis will have to run with the minimum acceptable thickness in order to preserve to the maximum extent the enhancement of the thermal transfer mechanism.
Implementing such optimized cooling design inside the segment model the overall pressure drops realized between the inlet and outlet coolant sections are estimated in 6.39 bar with a maximum predicted copper temperature of 132.1 °C and 60.79 °C as mean one. The thermo-mechanical analysis produced a maximum total equivalent Von Mises strain equal to 0.0971% associated to an estimated fatigue life of 458910 beam on/off cycles with a marginal gain of 57320 cycles with respect to present NICE upgrade design, equal to the overall amount of pulses expected to be performed during the MITICA experimental campaigns.

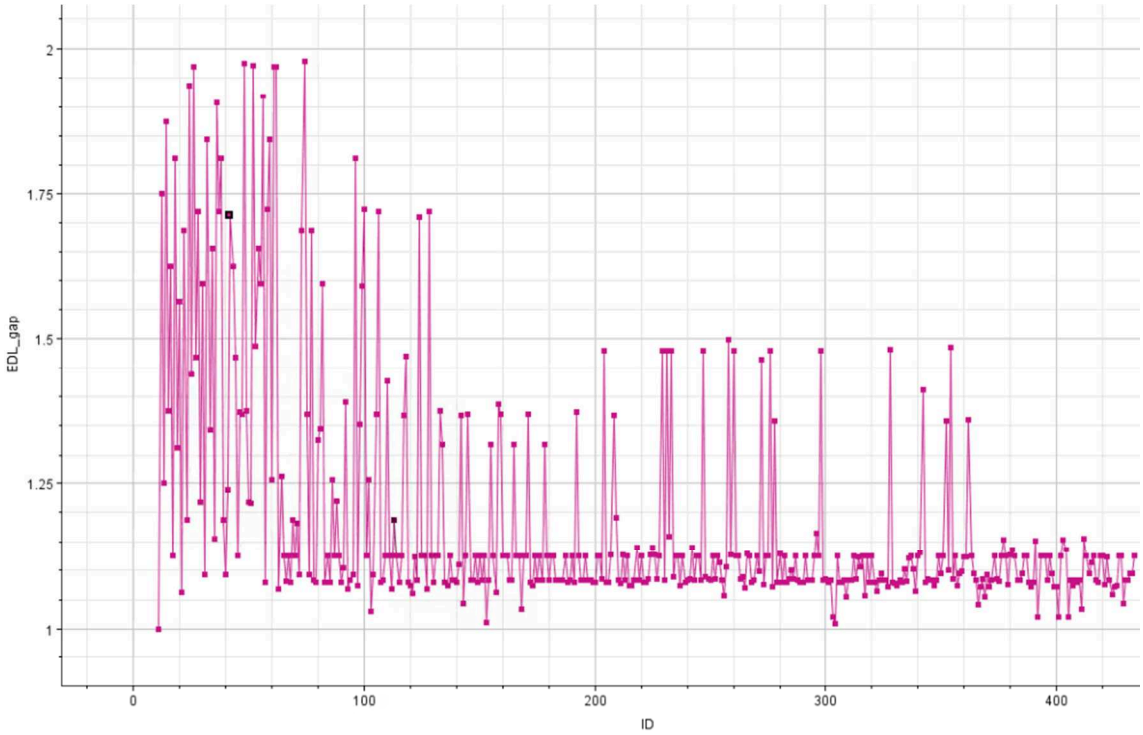

Figure 5.9 - Multi-history of the electrodeposited layer thickness along the analyses constituting the optimization process. The asymptotic range of values constituting the optimum solution form the thermal point of view is easily detectable in the interval 1.075-1.13 mm.

Conclusions and perspectives

The research activity presented in this thesis work has been carried out in the framework of EUROfusion Work Package Heating and Current Drive (WPHCD) work program within the Power Plant Physics and Development (PPPT) activities.
In fusion machines one of the most challenging issues, from an engineering point of view, is the reliability and thermal control efficiency of those components faced to the plasma and particle beam. The high heat fluxes and power densities they are subjected to, make the cooling capability of these devices one of the crucial aspects during the design phase.
The three years doctoral research work has been mainly dedicated to the triple objective to verify the present solution applied inside the MITICA experiment, to perform improvements with an acceptable pressure drop and reliable and feasible manufacturing process, and to develop further optimized solutions with a detailed exploration of the interrelated effects of input geometric parameters.
The main engineering constraints to be faced and solved during the design phase of novel cooling channels solutions are related with the geometrical constraints coming from beam optics optimizations and the space limitation constraints that severely affect the coolant distribution.
After an extensive CAE campaign ten different designs have been considered worth to be considered for the manufacturing phase. An Oxygen Free High Conductivity (OFHC) copper slab was then machined in order to obtain the created set of Single Channel Prototypes. Subsequently the cooling channels were closed through galvanic electrodeposition of copper. The same process was exploited for the realization of the Vacuum Tight Threaded Junction (VTTJ) between the copper structure and the stainless steel pipes to be connected to the hydraulic circuit.

A specific plant for testing cooling system components, called Insulation and Cooling Experiment (ICE), has been revamped in order to proceed with the testing phase of the novel cooling channel solutions which have been successfully produced.
A series of thermo-hydraulic tests on the Single Channel Prototypes (SCPs) under intense heat flux condition and elevate mass flow rate have been executed for a full qualification of the manufacturing process and assessment of the thermo-hydraulic design.
The electrodeposited layer covering the Single Straight Channel design was not able to withstand the internal pressure field realized in the cooling channel leading to a failure of the structure integrity with the creation of a leak opening. Such shortcoming however does not affect the sustainability of the adopted mechanical design and manufacturing process but highlight the need for a careful monitoring of the electrodeposition process.
Due to the impossibility of performing tests on the Single Straight Channel it was not possible to compare the experimental results with those coming from analytical correlations (Sieder-Tate and Gnielinski) limiting the data validation to the assessments of the estimation provided by the Computational Fluid-Dynamic (CFD) models.
The failed prototype will be however promptly recovered in order to benchmark it against well-known analytical correlations.
A further operation will be the verification of the correspondence between the NICE upgrade channels as designed in CAD environment and the realized one in the corresponding prototype in order to give an answer to the relevant discrepancy between the experimental and the numerical predictions in terms of pressure drop. This test could be performed through an infrared camera detecting the thermal footprint of the channel wall when subjected to a fast cooling transient. It could be indeed the case that the electrodeposition process could eventually result in a partial obstruction of the channel cross section leading to unavoidable increase of the associated hydraulic losses.
All the remaining prototypes are characterized by thermofluid-dynamic behaviour in good accordance with the prediction provided by the numerical analyses.
Being the cooling performance enhancements verified both experimentally and numerically, the different novel designs have been upgraded to the full scale model of the electrostatic accelerating segment.
Simultaneously the employment of an optimization multi-objective software has begun. Starting from present design geometry in MITICA, the software has provided further design inputs able to improve the cooling performances in terms of temperature distribution, pressure drops, fluid velocity and channel topology within the given requirements.
In the next future the thermofluid-dynamic optimization will be completed for the all different designs implemented on the segment model taking into account new available set of manufacturing option suggested by the present suppliers. Subsequently the optimization process will involve the mechanical details of the slits necessary for the relieving of the thermal stresses. Such devices will be analyzed in shape, thickness

and distribution in order to obtain the best compromise between high performance and design simplification.
In parallel the ICE test-bed facility will be equipped with additional ceramic heaters which will allow thermo-hydraulic tests on the SCPs under the real accelerator conditions both with nominal and non-nominal mass-flow and heat flux condition in order to understand the behaviour of the cooling channels event in other operative scenarios.
As a matter of fact future experimental campaigns aim to execute a set of test not only with normal water but employing ultra-pure one and also different cooling fluids (e.g. dielectric fluids) verifying the cooling performance and possible erosion or vibration issues even in a broader operational space.
The main advantages related with the implementation of novel enhanced cooling solutions rely indeed both on the possibility to extend the fatigue life-cycle of different high thermal stress components but also to investigate the possibility to employ alternative dielectric fluids instead of water since such novel design solutions would allow the exploitation of less performing fluids in terms of cooling capability.
Electrically insulating, fluorocarbon-based fluids (Galden, Fluorinert or RM101 successor) are in fact of technical interest since they are already used in various cooling applications for their stability also at high temperature. In addition they are characterized by an inert behaviour with respect of metallic surface (on the contrary of ultrapure water whose electrochemical performances in metallic environment have still to be investigated), they do not need costly purification systems and guarantee a good compatibility in nuclear environment.
Notwithstanding lower cooling capabilities and high cost of the fluids still set a number of issues to be properly faced and evaluated.
In conclusion the studies presented in this thesis, aimed to solve some of the most demanding issues regarding the design of the negative ion beam source, are allowing even to develop innovative technologies to be applied even in a short term horizon in the very next generation of neutral beam injectors.

Bibliography

[1] J. Freidberg, *Plasma Physics and Fusion Energy*, Cambridge University Press, 2007.

[2] S. Pfalzner, *An Introduction to Inertial Confinement Fusion*, CRC Press, 2006.

[3] S. Ortolani, Dalton D. Schnack, *Magnetohydrodinamic of Plasma Relaxation*, World Scientific, 1993.

[4] M. Zuin et al., *Overview of the RFX-mod fusion science activity*, Nuclear Fusion, Volume 57, Number 10, 2017.

[5] J. Freidberg, *Ideal Magnetohydrodynamics*, Plenum Publishing Company Limited, 1987.

[6] http://www.pppl.gov/about/history

[7] R.C. Wolf, *A stellarator reactor based on the optimization criteria of Wendelstein 7-X*, Fusion Engineering and Design, Volume 83, 2008.

[8] J. Wesson, *Tokamaks*, Clarendon Press, London, 2004.

[9] https://www.iter.org/

[10] V. Toigo et al., *The PRIMA Test Facility: SPIDER and MITICA test-beds for ITER neutral beam injectors*, New Journal of Physics, Volume 19, 2017.

[11] R. Hemsworth et al., *Status of the ITER heating neutral beam system*, Nuclear Fusion, Volume 49, 2009.

[12] L. Grisham et al., *Recent Improvements to the ITER Neutral Beam System Design,* Fusion Engineering and Design, Volume 87, 2012.

[13] P. Agostinetti et al., *Detailed design optimization of the MITICA negative ion accelerator in view of the ITER NBI*, Nuclear Fusion 56, 2016.

[14] N. Fonnesu et al., *A multi-beamlet analysis of the MITICA accelerator,* AIP Conference Proceedings, 2015.

[15] Various Authors, ITER SDC-IC, Structural Design Criteria for ITER In-Vessel Components. ITER Document No. G 74 MA 8.

[16] P. Agostinetti et al., *Investigation of the Thermo-mechanical properties of electro-deposited copper for ITER*, Journal of Nuclear Materials, 417 (2011), pp. 924–927.

[17] P. Agostinetti, G. Chitarin, G. Gambetta, D. Marcuzzi, *Two key improvements to enhance the thermo-mechanic performances of accelerator grids for neutral beam injectors*, Fusion Engineering and Design, November 2016.

[18] P. Agostinetti et al., *Detailed design optimization of the MITICA negative ion accelerator in view of the ITER NBI*, Nuclear Fusion 56 (2016) 016015.
[19] P. Agostinetti, M. D. Palma, D. Marcuzzi, P. Sonato, P. Zaccaria, *Vacuum tight threaded junction*, Dec. 2013.
[20] A. Rizzolo et al., *Thermo fluid dynamics test on the single channel prototypes for the SPIDER grids*, Fusion Science and Technology 62 (2012) 164-170.
[21] https://www.cfd-online.com/Wiki/RANS-base_turbulence_models.
[22] M. K. Kerimov, *On the 80th Birthday of Il'ya Meyerovich Sobol*, Computational Mathematics and Mathematical Physics, 47(7), 1065-1072, 2007.
[23] K. Deb, S. Agrawal, A. Pratap, T. Meyarivan, *A fast and elitist multi-objective genetic algorithm: NSGA-II*. IEEE Transaction on Evolutionary Computation 6(2), 182-197, 2002